Photonic Crystal Nanobeam Cavities for Biomedical Sensing

Thesis Advisor: Professor Marko Loncar Qimin Quan

Photonic Crystal Nanobeam Cavities for Biomedical Sensing

Abstract

Manipulation of light at the nanoscale has the promise to enable numerous technological advances in biomedical sensing, optical communications, nano-mechanics and quantum optics. As photons have vanishingly small interaction cross sections, their interactions have to be mitigated by matters (i.e. quantum emitters, molecules, electrons etc.). Waveguides and cavities are the fundamental building blocks of the optical circuits, which control or confine light to specific matters of interest.

The first half of the thesis (Chapters 2 & 3) focuses on how to design various photonic nanostructures to manipulate light on nano- to micro- scale, especially to modify the light-matter interaction properties. Chapter 2 discusses how nano-slot waveguides and photonic crystal nanobeam waveguides are able to modify the emission of quantum emitters, in a different way that normal ridge waveguides are not able to. Chapter 3 focuses on a more complicated and powerful structure: the photonic crystal nanobeam cavity. The design, fabrication and characterization of the photonic crystal nanobeam cavities are described and demonstrated in detail, which lays out the foundation of the biomedical sensing applications in the second half of the thesis.

The second half of the thesis (Chapters 4 & 5) focuses on the application of photonic crystal nanobeam cavities in the label-free sensing of biomedical substances.

Chapter 4 demonstrates detection of solutions with different refractive index (aceton, methanol, IPA etc.), glucose concentration, single polystyrene nanoparticles and single streptavidin bio-molecules. Chapter 4 proposes a novel nonlinear optical method to further enhance the sensitivity. Chapter 4 also demonstrates high quality nanobeam cavities fabricated in polymers, that open up a new route to decrease the cost, as well as to achieve novel applications with functional polymers. The broader impact of this technology lies in its potential of commercialization of a new generation of biosensors with high sensitivity and high integration. Chapter 5 discusses progresses towards instrumentation of the nanobeam cavity sensing technology for research & development apparatus, as well as point-of-care diagnostic tools.

Contents

Acknowledgments

First and foremost, it is my true pleasure to thank my advisor, Marko Loncar, for all of his support, encouragement and guidance throughout the past five years. I joined the group as the first generation of graduate students, when Marko just started the lab at Harvard. I could not assess how much I have learned from seeing him leading the group, building up the lab and progressively achieving so many scientific advances. His insight, creativity, and comments have been invaluable. He helped me sharpen my scientific vision every time I had to meet with him, and in fact, I always had to come up with a new, interesting idea to distract him from how little work I did. He has been extremely supportive, beyond a teacher, like a friend. I feel truly lucky to be Marko's student. I benefited in every aspect that a student can benefit.

Marko's excellent research group has a diverse lines of areas. I have been constantly inspired by learning from my fellow group members. I want to thank especially the sensor sub-group: Dr. Daniel L. Floyd, Ian B. Burgess, Dr. Sindy K. Y. Tang, Dr. Frank Vollmer and Anna Shneidman. I can not imagine I can accomplish anything with my zero knowledge of biomedical science if it is not Dan and Sindy. Thank you Frank so much for leading me to this fascinating area of optical cavity biosensing. I have learned from so many aspects from Ian, his management of time, smart planning of everything, as well as critical thinking of everything. Anna has been always so helpful with all the experiments and discussions.

I also want to specially thank Parag B. Deotare, Jennifer T. Choy, Birgit

Hausmann and Motoo Aiba. Parag has always been the first person that jumps on top of my head when I mess up with all kinds of problems. He has been like a big brother, with patience and knowledge to help me out. Jennifer has been the most warm-hearted person I have ever met, and sorry for all distractions when I have problems. Birgit is such a talent researcher, from whom I learnt the German style rigorious and humble characteristics. I enjoyed so many beer nights with Motoo, Maki and Dan. Motto taught me the Japanese style sincerity, humbleness, and hard work.

It was my great honor to have the opportunity to co-author with Dr. Irfan Bulu, Parag B. Deotare, Ian B. Burgess, Ian W. Frank, Jennifer T. Choy, Dr. Frank Vollmer, Dr. Sindy K. Y. Tang, Dr. Daniel L. Floyd, Birgit Hausmann and Michael J. Burek. I have also learned so much from discussions with Murray McCutcheon, Raji Shankar, Wallace Hui, Yinan Zhang, Tom Babinec, Haig Atikian, Dr. Mughees Khan, Dr. Eiji Iwase and Kathi Kleinlein.

I was also very fortunate to co-author with Prof. Mikhail D. Lukin, Prof. Joanna Aizenberg and Prof. George W. Whitesides.

I also like to thank Ms. Kathy LaFrance. You helped me to make the reimbursements and purchasing into such a delightful and smooth process.

During my first year, Darrick Chang and Liang Jiang from Professor Lukin's group were so helpful (and patient) to answer so many silly questions I had, and greatly inspired me with their physics insights. My way of thinking and judgement to a new physics problem greatly benefited from their influence.

Last few months, I have been working very closely with Nigel Clarke and Parth

Patel, two extremely talented CO-OP students from University of Waterloo. This is my first experience being a mentor myself. Because of Nigel and Parth's hard work and aspirations, we were able to accomplish so many advances in building the portable sensors.

In addition to Marko, I want to thank the many important science mentors I have luckily met at Harvard. Especially, Professor Mikhail Lukin's classes in Quantum Optics and Quantum Information lead me to deeper understanding of Optics. Professor Federico Capasso's class in Quantum Engineering inspired me how optics and semiconductor physics can be useful in modern technologies. Professor James G. Fujimoto's class Nonlinear Optics class at MIT leads me to a more fascinating world of optics. Professor Ken Crozier's class in Nanophotonics leads me to the interdisciplinary of modern nanotechnology and photonics. Professor Connor J. Walsh's class in Medical Device Design inspired me the pursuit of applying optical technology in medical applications. I am grateful to all the classes I took at Harvard, all the seminars I attended, and all the professors I have luckily chat with. They all shaped who I am and helped me achieve this thesis.

Much of my thesis also relies on the hard work of the greater community. I have been constantly obtaining knowledge and inspirations from reading the literatures from the optics, physics and photonic engineering community. And I hope this thesis contributes a small portion to the community as well.

During the final year, as some progresses were made on the research project, we realized that the project has a commercialization potential. I want to specially thank Sam Liss at the Harvard Technology Transfer Office to provide me so many

opportunities talking to potential collaborators, customers and investors. His business savvy and technology understandings enlightened me how technology can benefit the real world. With the project, we won the first prize in the MIT-CHIEF start-up competition, grand prize in ZhenFund pitch to China competition, and second prize in the global final of "Made for China" start-up competition.

I would also like to thank my dear Chinese friends: Meng Su, Yiqiao Tang, Nan Yang, Kevin Niu, Leizhi Sun, Yuqi Qin, Wenju Li, Shijin Wu, Juan Chen, Kai Wang, Shengqiang Cai, Ming Guo, Liu Yang, Xiaolu Yu, Wen Zhou, Yizhe Zhang, Shan Lou, Yuan Yuan, Sirui Zhou, Zhunan Chen, Jennifer Wang and Ben Fan. Without you guys, I can not imagine how boring my life will be in the five years. The get-together with Meng, Yiqiao and Yuqi have been always my most relaxed time. I enjoyed so many beer nights, and late night talks with Kevin and Nan, who I have learned so much beyond academics.

I want to specially thank Xiaole Wu, for your support and understanding in every aspect.

Finally, I thank my parents for all the love they gave to me. They have been the biggest supporter for me to accomplish all I have achieved. They let me truly understand how selfless the love can be. I want to dedicate this thesis to my dear Mom and Dad.

For my Mom and Dad

Chapter 1

Introduction

1.1 Photonics and Nano-optics

Optical science has been a science of over thousand years, since the development of lenses by the ancient Egyptians and Mesopotamians. The word optics comes from the ancient Greek word, meaning appearance or look. Optics usually describes the behavior of visible, ultraviolet, and infrared light. Since light is an electromagnetic wave, other forms of electromagnetic radiation such as X-rays, microwaves, and radio waves have exact same properties.

What makes today's optics different from the old days?

I think there are two aspects: first, the number of photons that are involved in the process has become fewer and fewer, and thus the emerging field is called photonics. Today we begin to look into the behavior of single photons, a new class of light source, just like lasers 50 years ago. We also begin to study the interaction

between single photons and single atoms, as well as the entanglement of two or few photons.

The other is the physical scale in which the optical processes occur. Thanks to the development of the nanotechnology, we are now able to fabricate features in sub-microscale, approaching or smaller the length of the light wavelength (therefore the field is called nano-optics). And as a result, manipulation of the light can be achieved in light-wavelength scale, which enables numerous applications in optical communications, biomedical sensing and quantum optics.

1.2 Outline of the Thesis

In this thesis, we will focus on how to manipulate light at nanoscale, and especially, how it can be used in biomedical sensing.

Light and light has vanishingly small interaction cross section, and has to be mitigated by matter. In most of all applications (light source, detectors, solar cells), the core of the theme is to enhance or suppress the interaction between light and matter in a controlled way. The fundamental building blocks to manipulate light are waveguides and cavities. More complicated structures, for example CROW (coupled-resonator-optical waveguide), coupled ring resonators, or gratings are all based on waveguides and cavities. This thesis includes the discussion of four nano-scale structures, slot waveguide and photonic crystal waveguide in Chapter 2, and ring resonators and photonic crystal nanobeam cavities in Chapter 3, with a special emphasis on the photonic crystal nanobeam cavities.

Photonic crystals are periodic optical nanostructures that are designed to affect the motion of photons in a similar way that periodicity of a semiconductor crystal affects the motion of electrons. Photonic crystals that occur in nature and in various forms (e.g butterfly wings) have been studied scientifically for the past decades. However, the first artificial photonic crystal at near-infrared was not achieved until 1996(1), which opened up the way for photonic crystals to be fabricated in semiconductor materials by borrowing the methods used in the semiconductor industry. The first photonic crystal cavity was demonstrated in 1997 (2). However, the Q-factor (essential figure of merit of all cavities) was very low. This Q ($\sim$ 250) was not limited by fabrication errors, but rather due to under optimized design of the photonic structure. In Chapter 3, we propose and demonstrate a new method to deterministically design the photonic crystal nanobeam cavities. With this method, the Q was increased by several orders of magnitude, and the design process was also simplified from many hours to several minutes.

The second half of the thesis (Chapters 4 & 5) focuses on the application of photonic crystal nanobeam cavities in the label-free sensing of biomedical substances. We demonstrate the detection of various solutions with different refractive index, glucose concentrations, 25nm polystyrene particles, a single streptavidin molecule, as well as low abundance of BSA molecules. High quality sensors fabricated in polymeric materials are also demonstrated which open up a new route to low-cost and versatile functionality. Chapter 5 discusses the progresses towards instrumentation of the nanocavity sensing technology. The sensor chips are fabricated with commercial foundry technology, the set-up is modified to a portable platform amenable to multiplexed detection.

The thesis concludes with summary and future directions.

1.3 Scientific Achievement of the Thesis

There are two major contributions in this thesis.

First, we invented a deterministic design method to design high-Q, small mode volume cavities, and demonstrated the record high Qs, both in simulation and in experiment. The design was inspired by Noda group's previous study of Gaussian field distribution for optimal cavity field(3), and was based on the fourier space analysis method, proposed by Scherer's group at Caltech(4). Previous designs of ultra-high Q cavities are primarily based on trial-and-error method, which involved extensive parameter search and optimization. Current deterministic design method based on mathematical descriptions, has a clear recipe, and eliminates large computational cost in the design process. Fig. 1.1 summaries selected state-of-the-art photonic crystal cavities. Not only have we demonstrated the highest Q and both high-Q and high Transmission simultaneously, but also our method outperforms in the computational cost.

Second, with the high-Q, small-V photonic crystal nanobeam cavities we demonstrated detection of record low concentration of BSAs, single 25nm-polystyrene nanoparticles and single streptavidin molecules, achieving the state-of-the-art, as shown in Fig. 1.2. Furthermore, we also demonstrated that high-Q cavities can also be achieved in polymer based materials. The simplified fabrication process of polymeric cavities potentially eliminates the need of clean-room facilities and can be

Group	Simulation	Experiment	Computer cost
Noda @ Kyoto	$Q=1\times10^{9}$	$Q=3\times10^{6}$	Average: numerical +FDTD
Notomi @ NTT	$Q=2.9\times10^{8}$	$Q=7.2\times10^{5}$	High: FDTD
Vuckovic @ Stanford	$Q=4\times10^{6}$		Low: numerical estimation
De La Rue @ Glasgov	$Q=1.8\times10^{5}$,T=48%	$Q=1.5\times10^{5}$,T=34%	High: FDTD
Current work	$Q=5\times10^{9}$	$Q=1\times10^{6}$	Low: band-diagram simulation
	$Q=1\times10^{7}$,T=97%	$Q=8\times10^{4}$,T=75%	

Figure 1.1.— Comparison of the state-of-the-art Q-factors that have been demonstrated in different groups. Simulation refers to the design Q value obtained from the finite-difference-time-domain (FDTD) method. As a general rule, higher Q will result in smaller the signal transmission (T) of the system. With current deterministically optimized method, we demonstrated both record high Q cavities, and record high-Q and high-T cavities.

Group	System	Detection	comments
Vahala @Caltech Yang@WUSTL Lu@Victoria	Microtoroid 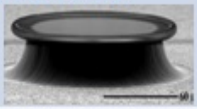	25nm nanoparticle Influnza virus	Yang @ WUSTLE Armani @ USC
Vollmer @ MPQ	Microsphere 	Influenza virus	First demonstration of single virus @Rowland institute
Bailey @ UIUC	Ring resonator 	150fM miRNA, 10ng/mL PSA, IL8	Biomarker detection in complex mixture
Baba @ Yokohama National Univ.	2D PhC 	1fM BSA	2D photonic crystal slot laser
Current work	Nanobeam (1D PhC) 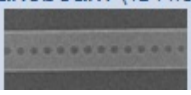	1aM BSA, 25nm nanoparticle Single streptavidin	Towards instrumentation

Figure 1.2.— Detection limit that has been demonstrated in different cavity systems.

fabricated at low cost.

1.4 Commercialization Potential of the Nanocavity Sensing Technology

The broader impact of this technology lies in its potential of commercialization of a new generation of biosensors with high sensitivity and high integration.

With the discovery of new disease biomarkers and emergence of new pathogenic strains of bacteria and viruses, rapid and sensitive biomolecular detection is increasingly important in biomedicine and public health. While ultra-sensitive and specific fluorescence based assays have enabled a number of scientific advances and commercial applications, the labeling process is often complex, difficult to control, can interfere with receptor affinity, limits the throughput and results in long assay time.

To remedy limitations for high-throughput (HT) detection posed by the current labels-based biosensing approaches, we use the nanobeam photonic cavity label-free sensing method as the sensing principle and develop an ultra-sensitive, real-time, micrometer-size sensing device fabricated using conventional semiconductor processing. It is capable of sensing low abundance biochemical particles (e.g proteins, viruses and etc) in real-time. Furthermore, the sensor can be integrated with electronic components and versatile forms of fluidic/gas channels; and supports high throughput and parallel detection. Scaling up to mass production is possible since chip fabrication uses the standard commercial CMOS foundry technologies,

with well documented low costs per unit wafer area, with high density integration and high yield. We envision a new class of biomedical instruments based on this device for high performance, high value research & development tools. We also envision a point-of-care diagnostic tool for food/water safety and disease diagnostics.

Chapter 2

Nano-scale Optical Structures for Enhancement of Light and Matter Interactions - Waveguides

2.1 Introduction

An optical waveguide is a structure that guides electromagnetic waves at visible to near-IR wavelength. Light is guided due to the index contrast between different materials. It can be confined in one dimension such as in slab waveguides or two dimensions as in fibers and ridge waveguides. By diffraction theory, the minimum mode area (cross-section) that light can be confined in a homogeneous media is $S = (\lambda/n)^2$, λ being its wavelength, and n is the refractive index of the media. The interaction probability between light and matter embedded in the media is inversely

proportional to the size of the mode, as well as the group velocity of the mode: $S \cdot v_{\mathtt{group}}$. Therefore, the probability of a single emitter emitting or absorbing photons is larger when the light is "squeezed" in a smaller mode area, and when light travels more slowly across the emitter. In this chapter, we will see how nanoscale structures can greatly change the light interaction strength by tailoring S and $v_{\mathtt{group}}$.

2.2 Slot Waveguide

A slot waveguide is a ridge waveguide with a slot cutting through the middle of its solid-center. The most common configurations are shown in Fig. 2.1. It is first proposed by Lipson's group at Cornell (5)-(12). It shows that the optical field inside the slot is greatly enhanced due to the index discontinuity and boundary conditions. In the following discussions, we focus on how the light-matter interaction is enhanced, and we propose an ideal application taking advantage of this light enhancement effect.

The figure of merit to characterize the light-matter interaction is indicated by α-factor, defined as $\alpha = \gamma_{\mathtt{wg}}/\gamma_0$, the ratio between the emission rate into the slot waveguide mode (both directions combined) and the intrinsic spontaneous emission rate in free space. To capture the physical mechanism of the enhancement of α, we use a simple toy model to analyze a solid-core (slot width is zero) dielectric waveguide (index n), with cross section $a \times b$, surrounded by air. Neglecting the field outside the dielectric and applying a perfect electric conductor boundary condition, the mode inside the dielectric can be approximated by $\phi_0 = \cos(\pi x/a)\cos(\pi y/b)$, resulting in the mode size $S = ab/4$. The key is that the introduction of an narrow air

slot (width δ) results only in the change of the field magnitude outside the slot, while overall mode shape is maintained i.e. $\phi = t\phi_0$, (t is a coefficient which drops off in the final expression). Within the slot, however, the electric field (TE-like polarized) can be written as $\phi = t\epsilon\phi_0$ ($\epsilon = n^2$), due to boundary conditions. The mode size of the slot waveguide is then $S = ab/(4\epsilon) + \delta b$. The major field distribution, perturbed by slot with different widths are shown in Fig. 2.2. Hence the ratio between the slot and the solid-core waveguide mode size is $\eta(\delta) = \frac{a/4+\epsilon\delta}{\epsilon a/4} \rightarrow \frac{1}{\epsilon}$, as $\delta \rightarrow 0$.

Since n=1 at $(n\vec{\phi})_{\max}$, the enhancement emission rate provided by the slot waveguide, compared to the free space, scales as $\alpha \propto \epsilon^2 \cdot n_{vg}$, and this scaling law is strictly valid only at the zero slot limit. A similar scaling was obtained by Ho and colleagues(13) who studied the inhibition of spontaneous emission. This indicates that a narrow air slot in a silicon ($\epsilon = 12.25$) ridge waveguide can enhance the interaction of its mode and the emitter in the slot by a maximum of two orders of magnitude. In comparison, solid-core waveguide provides an enhancement of $n_{vg} \sim 3$ and homogenous bulk medium enhances by $n_{\text{bulk}} = 3.5$ over the free space emission rate.

We compare the result from the toy model and that solved by finite element method (FEM). A nice agreement is shown in Table.2.1, which implies the correct mechanism that is addressed in the toy model. Hence the enhancement factor scales as $\alpha \propto \epsilon^2$ at small gaps. Note that this scaling rule is different from (14), where an enhancement of emission in a high index contrast microcavity is discussed in the weak coupling regime.

To calculate more rigorously the enhancement factor, this emitter-waveguide

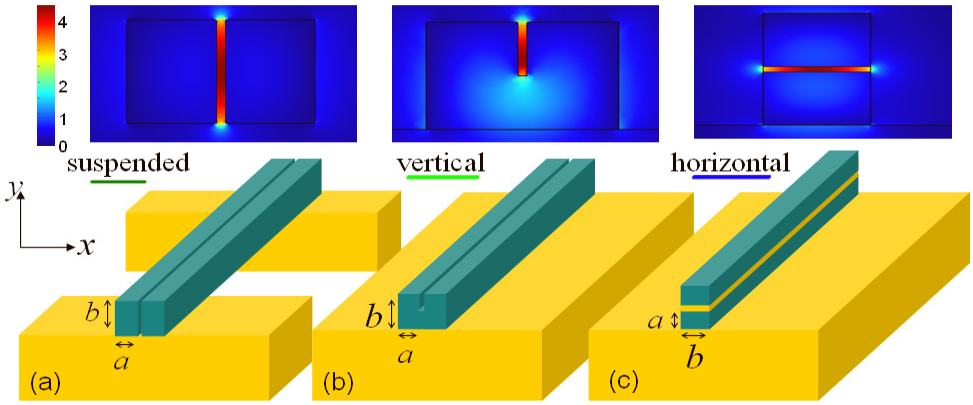

Figure 2.1.— Configurations of proposed waveguide QED device. In all cases $\lambda = 1.5\mu m$, and $a = 0.2\mu m, b = 0.25\mu m$. (a)A slot waveguide with material index 3.5, suspended in air. (b) A vertical and (c) horizontal on-substrate configurations. Insets show major field components $|E_x|$ in (a)&(b) and $|E_y|$ in (c).

Table 2.1: Comparison of the results from toy model and finite element method of the transverse mode size.

Gap width δ	$0.005\mu m$	$0.01\mu m$	$0.02\mu m$
Toy model η	7.66	5.56	3.55
FEM η	7.20	5.95	3.19

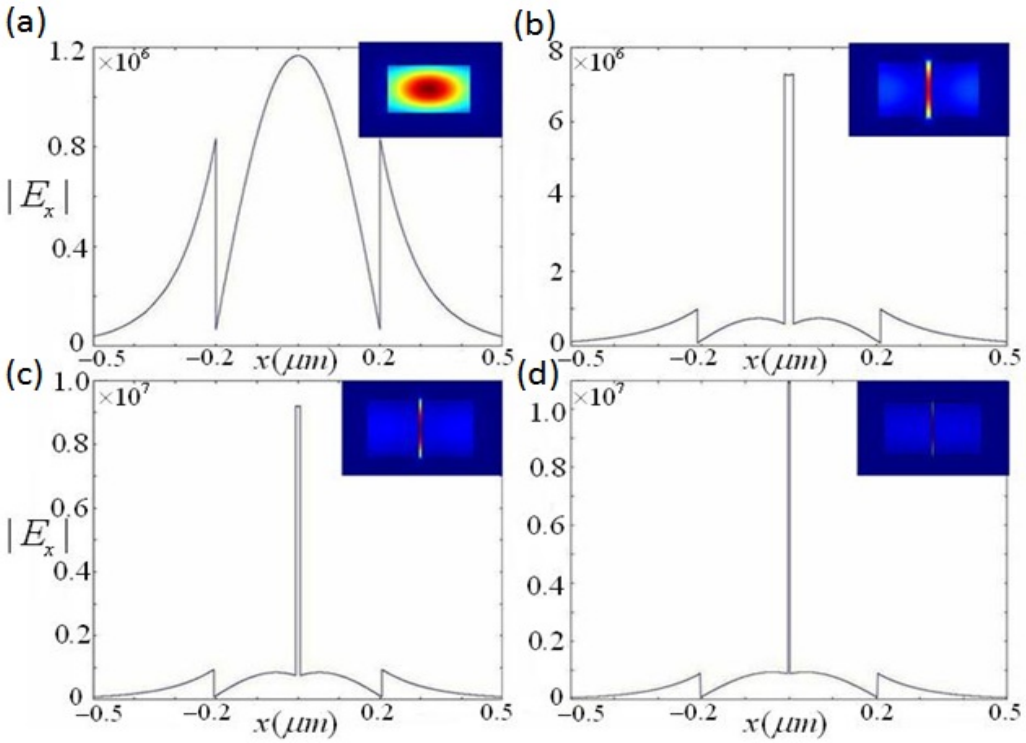

Figure 2.2.— Comparison between E_x for solid-core waveguide (a) and slot waveguide with gap width 20nm (b), 10nm (c), 5nm (d), normalized to a single photon, i.e. $|E_x|/\sqrt{\int \epsilon_r |\mathbf{E}(\mathbf{r}_T)|^2 d\mathbf{r}_T}$. For slot waveguide, $E_x|_{x=0}$ directly reflects the inverse of mode size. Inset plots are the electric energy density of each mode.

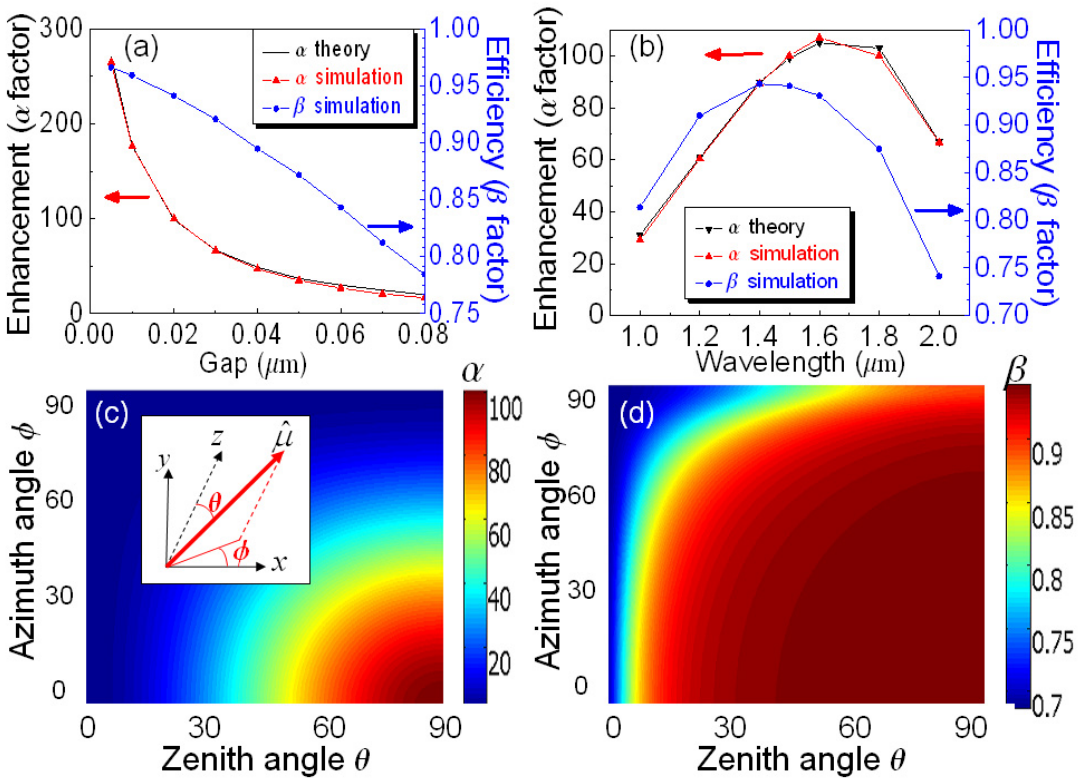

Figure 2.3.— (a) Enhancement(α factor) and efficiency(β factor) for slot waveguide with $a = 0.2\mu m, b = 0.25\mu m$ at different gap sizes. The dipole emits at $1.5\mu m$. (b) α and β factors v.s wavelength. (c) and (d) show the polarization dependence of α and β factors respectively. Inset (c): the zenith angle is between the dipole orientation and the z-axis, and azimuthal angle is between the x-axis and projection of the dipole orientation onto the x-y plane.

system can be described with Wigner-Weisskopf theory. The quantum emitter is coupled to both the continuum modes of free space and to the modes of the slot waveguide. The atomic two level system is coupled to both the continuum modes of free space and also to the modes of slot waveguide. The coupling strength to each waveguide mode is denoted by $g_{i,k}$, subscript i for a different mode of the slot waveguide, and k is the effective wave vector. The modified spontaneous emission into vacuum, denoted as γ', is incorporated into the Hamiltonian as an imaginary part in the framework of quantum jump description of an open system(15). The intrinsic spontaneous emission in free space is denoted as γ_0.

$$H = \hbar(w - i\frac{\gamma'}{2})\sigma_{ee} + \sum_{i,k>0} \hbar\omega_{i,k}(a^{\dagger}_{i,Rk}a_{i,Rk} + a^{\dagger}_{i,L-k}a_{i,L-k}) + \sum_{i,k>0} \hbar g_{i,k}[\sigma_{eg}(a^{\dagger}_{i,Lk} + a^{\dagger}_{i,Rk}) + h.c.] \tag{2.1}$$

The Fourier component of the waveguide mode is explicitly divided as $a^{\dagger}_{Rk}$-right propagating and $a^{\dagger}_{L-k}$-left propagating waveguide modes. The electric field associated with single photon takes the following quantized form

$$\mathbf{E} = \sqrt{\frac{\hbar\omega}{2\epsilon_0 L}}\phi(\mathbf{r}_T)a^{\dagger}e^{\imath n_{\mathtt{eff}}kx - i\omega t} \tag{2.2}$$

with normalization as $\int \epsilon_r|\phi(\mathbf{r}_T|^2 d\mathbf{r}_T = 1$, L is the interaction length. With the definition of mode size as $S = \int \epsilon_r|\vec{\phi}|^2 d\mathbf{r}_T/(\epsilon_r|\vec{\phi}|^2)_{\mathtt{max}}$, the coupling strength of the atom and photon is

$$g^i_k(\mathbf{r}) = \frac{\vec{\mu}\cdot\mathbf{E}^i}{\hbar} = \frac{1}{\hbar}\sqrt{\frac{\hbar\omega^i_k}{2\epsilon_0 LS}}\frac{\mu\cdot\vec{\phi}^i_{coup}(\mathbf{r})}{(n|\vec{\phi}^i|)_{\mathtt{max}}} \tag{2.3}$$

$\vec{\phi}^i_{coup}$ is the electrical field at the position of the emitter. The decay rate into a particular waveguide mode (including both left and right propagating mode) is $2|g^i_k|^2 L/v^i_g$, where $\omega^i_k = \omega$ and $v^i_g = d\omega^i_k/dk$ is the group velocity of the ith mode. The

spontaneous emission rate into freespace reads $\gamma_0 = \frac{\mu^2\omega^3}{3\pi\epsilon_0 c^3\hbar}$, hence the enhancement factor compared to the intrinsic spontaneous decay rate is

$$\alpha = \frac{\gamma_{\mathtt{wg}}}{\gamma_0} = \sum_i \frac{3}{4\pi}\frac{\lambda_0^2}{S^i}\frac{c}{v_g^i}\frac{|\vec{\phi}^i_{coup}\cdot\hat{\mu}|^2}{|(n\vec{\phi}^i)_{max}|^2} \tag{2.4}$$

The sum is over all the modes that slot waveguide supports, $\mathbf{r}_0$ represents the position of the emitter. Clearly, if the mode size S is squeezed significantly below λ_0^2, then the light-matter interaction could be dramatically enhanced. In addition, a reduction in the group velocity in a slot waveguide (group index $n_{vg} \sim 3.5 - 4$) increases the LDOS and also contributes to the increase in α. However, this is a minor effect compared to the enhancement due to light localization in the waveguide slot.

Another important figure of merit is the waveguide coupling efficiency, $\beta = \gamma_{\mathtt{wg}}/\gamma_{\mathtt{total}}$, defined as the ratio between the emission rate into the waveguide mode (both directions combined) and total emission rate into all radiative channels. $\beta/(1-\beta)$ corresponds to cooperativity often used in cQED (that is, optical depth used in cold atoms), and it discriminates the strong coupling from weak coupling regime. In the former case, highly nonlinear optical effects are expected(16), that are important for devices like a single atom quantum gate(17) and a single photon transistor(18). The total enhancement of spontaneous emission, the Purcell factor (19), can be found as α/β.

Both α and β-factors can be obtained from 3D finite-difference time-domain (FDTD) simulation by placing a dipole source at the center of the gap and monitoring the power emitted into the waveguide. Fig. 2.3 shows the α and β factors of the slot waveguide with $a = 0.2\mu m$ and $b = 0.25\mu m$ for different gap widths,

different wavelengths, and different polarizations. In Fig. 2.3(a), we assumed an $\hat{x}$-polarized dipole source that emits at $1.5\mu m$, placed at the center of the slot and varied the gap from 5nm to 80nm. An excellent agreement between α's obtained from theory and FDTD simulation is obtained. An enhancement of up to 270 is obtained for a gap size of 5nm, and 100 is obtained with a moderate gap size of 20nm. An efficiency better than 90% is maintained for a gap width$\leq 30nm$. As the slot width is further reduced towards zero width, α factor converges to $3\epsilon^2 n_{vg}/\pi$, assuming that the corresponding solid-core waveguide has a minimum mode size of $(\lambda_0/2n)^2$. This upper limit, however, is valid within mesoscopic scale when materials can be described by different refractive indices and the Maxwell boundary conditions are valid. For vanishingly small slots (down to the atomic scale), the discontinuity of boundary conditions for E-field breaks down and one recovers the solid-core waveguide regime. Fig. 2.3(b) shows the enhancement factor at different wavelengths for a slot waveguide with $a = 0.2\mu m, b = 0.25\mu m$ and a moderate gap width $0.02\mu m$. $\alpha > 50$ (half of its maximum value) is achieved in the wavelength range from $1.2\mu m$ to $2\mu m$. The optimal value of α at $1.6\mu m$ is due to the trade-off between the increase in wavelength and reduction in the effective mode index for longer wavelengths. The enhancement bandwidth for the current wQED system is over 800nm, and strong coupling is maintained across the wavelength range $1 - 2\mu m$. As a comparison, a cQED system with a $Q \sim 10,000$ operating at $1.5\mu m$ has a bandwidth $\sim 0.15nm$. However, a cQED system provides much larger values of α (larger than $1,000$ has been predicted). At the same time, the photonic crystal waveguide approach provides $\alpha \sim 30$ and $\beta \sim 0.9$ over a bandwidth of 20nm(23)-(24). Finally, solid-core waveguide, with core index n and air cladding, provides $\alpha_{solid} \sim n$, which is similar

to the enhancement in bulk material with the same index (25). Therefore, the emission enhancement provided by the slot waveguide, when compared to both bulk and solid-core geometry, is approximately α_{slot}/n and is in the range of $10 - 100$ for slot widths explored in Fig. 2.3(a)&(b). It is important to mention that slot geometry does not provide better waveguide coupling efficiencies, β, than solid-core geometry (25). This can be attributed to the enhanced emission into the leaky modes of the slot waveguide, in addition to the guided ones. However, an advantage of slot-waveguide is its large Purcell factor (α/β) which enhances radiative processes over the non-radiative ones (common to solid state emitters). This is highly desirable in order to coherently extract photons into the waveguide mode.

Fig. 2.3(c) and (d) show the polarization dependence of the α and β factors, for a slot waveguide with a 20nm gap. This waveguide geometry supports one TE-like mode with phase index 1.68 [E_x profile shown in Fig. 2.2(b)] along with two other modes (effective indices of 1.49 and 1.03) with different symmetries(not shown). Differently polarized dipoles will preferentially couple to one of these three modes. For the $\hat{y}$ or $\hat{z}$-dipole, there is virtually no emission enhancement ($\alpha \sim 1$). Therefore, the amount of spontaneous emission rate enhancement can be viewed as a contribution from the $\hat{x}$ component of the dipole. The efficiencies of $\hat{y}$ and $\hat{z}$-dipoles are 89% and 69% respectively. Therefore, high extraction efficiency as well as strong coupling between an emitter and a slot waveguide is possible for range of different polarizations.

The slot waveguide is a convenient platform from the experimental point of view, since the emitter can be placed in the gap region where optical field is the strongest. This geometry can be used in QED experiments with cold atoms trapped

directly by the waveguide field inside the slot(26), or in a solid state QED system with quantum emitters (e.g. nanocrystals and molecules) placed in the slot. We show two experimental schemes for a solid state QED application, namely, the vertical half-slot and horizontal slot in Fig. 2.1 (b&c). In the vertical configuration, the slot is etched only halfway, and the quantum emitter is placed at the bottom (center of the waveguide). In the horizontal configuration, the quantum emitters are embedded within the low index material that forms the slot (n=1.46)(7). For these two realistic cases, we estimate the degradation of the α and β factors due to reduced index contrast by simulating the nanocrystal quantum dot as a sphere with diameter of 10nm with refractive index n=2 (average of core and shell in PbS quantum dots). We do not take into account the details of the inner structure of solid state emitters or local field correction due to various field-screening effects(27). We find that $\beta \sim 0.91$ for the vertical configuration and $\beta \sim 0.72$ for the horizontal configuration, for geometries in the range $a \in [0.2, 0.3]\mu m$, $b \in [0.2, 0.3]\mu m$, and gap width $= 20nm$. We also find $\alpha_{\texttt{hoz}} = 98$ and $\alpha_{\texttt{ver}} = 28$, when compared to a dipole embedded in a 10nm-diameter nanocrystal with index of 2 ($\alpha_{\texttt{hoz}} = 14$ and $\alpha_{\texttt{ver}} = 4$, when compared to a dipole embedded in a uniform medium with index of 2). Reduction of the enhancement is due to smaller index contrast between waveguide and emitter as well as non-ideal overlap between the field and emitter in the vertical case. However, the efficiency is robust and doesn't depend strongly on the effective index of the emitter, but instead on the waveguide index.

The impressive ability to enhance the emission and extraction of photons with high fidelity makes the slot-waveguide an appealing platform for applications in quantum information. Here we propose an implementation of an optically

addressable photon register, shown in Fig. 2.4.

Single emitters, used to store photons, are placed along the waveguide so that each can be addressed individually using external control pulses(can be integrated on the same chip). We assume that each emitter has a triplet ground state, denoted according to polarization as X, Y and Z-state, and e is the excited state. For the TE-like mode, the $\hat{X}$-component is the major component and is the only non-vanishing component at the center of the slot. As a result, emitters polarized in $\hat{Y}$ or $\hat{Z}$-direction will not couple to the TE-like slot waveguide mode. Our register is first initialized by setting all emitters into the Z-state, so that they are decoupled from the waveguide, and do not interact with light propagating down the waveguide. Next, one of the emitters is prepared by external control into X-state without changing the states of the other units. Now, a single photon propagating in the waveguide can be absorbed by the emitter, thus setting the emitter into the state Y. This can be achieved by applying a time-dependent classical control pulse on transition between e and Y-state, using techniques similar to the ones originally used by Fleischhauer et. al. to map single photon field to collective atomic excitations (39)(29). Once a photon is stored in Y-state, the unit is again decoupled from the waveguide. Photon retrieval can be accomplished using the same control pulse, time reversed.

To calculate the storage and retrieval efficiency, the Hamiltonian for this system

is written with a slight modification to Expression (2.1)

$$H = \hbar(\omega_{eg} - i\frac{\gamma'}{2})\sigma_{ee} + \hbar\omega_{gs}\sigma_{ss} + \hbar(\Omega\sigma_{es} + h.c.) + \sum_{k>0} \hbar\omega_k(a^\dagger_{Rk}a_{Rk} + a^\dagger_{L-k}a_{L-k}) + \sum_{k>0} \hbar g_k[\sigma_{eg}(a^\dagger_{Lk} + a^\dagger_{Rk}) + h.c.] \quad (2.5)$$

where Ω is the Rabi frequency of the classical control, e is the excited state, two stable states g and s denotes H and V states respectively. Also denote the detuning as $\delta_k = \omega_k - \omega_{eg}$ and group velocity is $v_g = d\omega_k/dk$. The state can be written as

$$|\psi >= c_e|e, 0 > +c_s|s, 0 > + \sum_{k>0} c_{Rk}|g, k > + \sum_{k>0} c_{L-k}|g, -k > \quad (2.6)$$

In the retrieval process, assuming the photon has already been stored at s-state. Solve the time dynamics of the Schrodinger equation under the condition $\Omega >> \gamma', \gamma_{\mathtt{wg}}$. Define $\gamma(t, 0) = \int_0^t dt2|\Omega(t)|^2/\gamma_{\mathtt{wg}}$. The population in s-state decays as $c_s(t) = e^{-\gamma(t,0)}$, and the outgoing single photon pulse splits into a left-propagating and a right-propagating pulse as

$$c^{R,L} = -\frac{2g^*}{\gamma_{\mathrm{wg}}} \int_0^t dt' e^{-\gamma(t,0)} e^{-i\delta_k(t-t')} \quad (2.7)$$

Retrieval efficiency is then

$$\sum_{k>0,R,L} |c_k(\infty)|^2 = \beta(1 - e^{-\gamma(\infty,0)}) \to \beta \quad (2.8)$$

The outgoing photon pulse shape is

$$c_{+}^{\mathtt{out}} = -\frac{2g^{*}L}{\gamma_{wg}v_g}\theta(x)\theta(t-x/v_g)\Omega(t-x/v_g)$$
$$\exp[-\gamma(t-x/v_g,0)]\exp[iw_{eg}x/v_g]$$
$$c_{-}^{\mathtt{out}} = -\frac{2g^{*}L}{\gamma_{wg}v_g}\theta(-x)\theta(t+x/v_g)\Omega(t+x/v_g) \tag{2.9}$$
$$\exp[-\gamma(t+x/v_g,0)]\exp[-iw_{eg}x/v_g] \tag{2.10}$$

The outgoing pulse shape is totally determined by the control light. For the storage process, one can naturally imagine the time reversal process. In order to store an incoming photon pulse, the control pulse must match with the incoming photon pulse shape. Let the incoming photon shape at $x = 0$(position of the emitter) be $c^{\mathtt{in}}(x=0,t)$. In order to maximize $c_s(t=\infty)$, the control pulse should take the form

$$\Omega(t) = \frac{\sqrt{\gamma_{\mathtt{wg}}+\gamma'}}{2}\frac{|c^{in}(t')|}{[\int_0^t dt'|c^{in}(t')|^2]^{1/2}} \tag{2.11}$$

To calculate the storage efficiency, under the condition that $c_{Rk}(0) = c_{L-k}(0)$

$$|c_s(\infty)|^2 = |\frac{2g^{*}\Omega^{*}}{\gamma_{\mathtt{wg}}+\gamma'}\int_0^{\infty} dt'\Omega^{*}(t')e^{-\gamma(\infty,t')}c^{\mathtt{in}}(t')|^2$$
$$= \beta(1-e^{-\gamma(\infty,0)}) \rightarrow \beta \tag{2.12}$$

This means incoming photon should be split into two symmetric pulses arriving from both sides. Without splitting, the efficiency will be 50%. This is a direct result of the symmetry of the waveguide, which makes the emitter couples only to the symmetric state of $a_{Rk}^{\dagger} + c_{L-k}^{\dagger}$ in Expression[2.5]. And the antisymmetric photon pulse $a_{Rk}^{\dagger} - c_{L-k}^{\dagger}$ is a dark state to the emitter.

The proposed scheme can also be used to implement a quantum memory: due to the strong coupling between a waveguide mode and an atom placed in the slot,

the atomic state $\cos\theta|Y> + e^{i\phi}\sin\theta|X>$ can be efficiently mapped onto the photon state (using classical control pulse) $\cos\theta|1> + e^{i\phi}\sin\theta|\texttt{vac}>$, with high fidelity. Our platform can also be used to realize single-photon transistors, similar to the one based on metallic nanowires recently proposed by Chang et. al. (18). The advantage of the slot waveguide, however, is that the material losses are negligible.

2.3 Photonic Crystal Waveguide

A photonic crystal nanobeam waveguide (Fig. 2.5) contains regularly repeating internal regions of high and low dielectric materials. Like electronic energy bands in semiconductor physics, photons with certain wavelength (or energy) are not allowed to travel as an eigenmode in the waveguide, and this wavelength range is called photonic band gaps. This gives rise to distinct optical phenomena such as inhibition of spontaneous emission, high-reflecting omni-directional mirrors and etc.

Since the fundamental physics is due to diffraction, the periodicity of the photonic crystal structure (r, a, b in Fig. 2.5) is on the same order of half wavelength of the carrying light. Thanks to the advances of nanofabrication technologies during the past 20 years, making high quality photonic crystals has been possible.

A typical band-structure (or dispersion relation) of a photonic crystal waveguide is shown in Fig. 2.6. f denotes filling fraction, defined as $f = \pi r^2/ab$. The two shaded areas are the band gap regions corresponding to $f = 0.1$ and $f = 0.2$. The emission of emitters with transition frequency inside the band gap will be greatly suppressed. On the other hand, the emission of emitters with the transition frequency

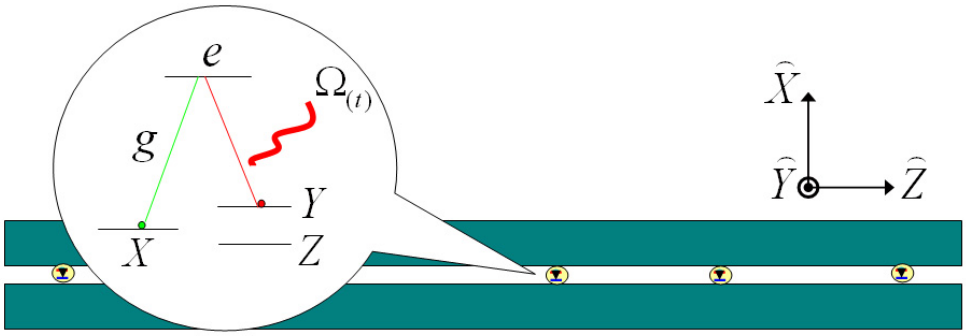

Figure 2.4.— A schematic of optically addressable photon register that allows storage (retrieval) of a photon into (out of) a specific quantum emitter. Before and after the storage (retrieval), the emitter is decoupled from the waveguide.

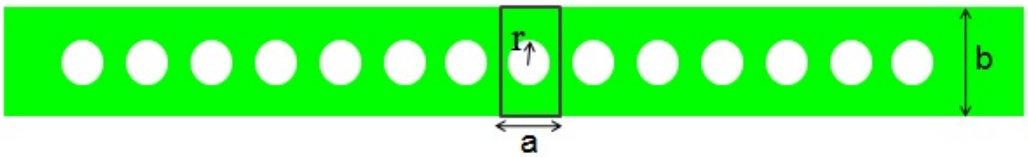

Figure 2.5.— Schematics (top view) of a photonic crystal nanobeam waveguide. It is a periodically perforated ridge waveguide. The holes can be any shape, squares, triangles and etc. f denotes for filling fraction, defined as the area of hole divided by the area of a single periodic unit.

on or close to the bandedge (as circled in Fig. 2.6) will be greatly enhanced, since the optical mode has a reduced group velocity: $v_g = d\omega/dk$, according to Expression 2.5. In the previous section, the slot waveguide enhances the emission of the matter due to squeezing of the optical mode area S. On the other hand, in photonic crystal nanobeam cavities, emissions are enhanced due to reduced group velocity v_g.

Both systems can be used to build a high fidelity photon register, as well as to "network" different quantum emitters. However, the efficiency of slot waveguide is limited by 25%, as during the retrieval and storage process, photons are emitted in left and right directions, (half of the photons are lost). To remedy this problem, we propose to use a photonic crystal waveguide with modulated Bragg mirrors on one side (modulate size of the holes) which adiabatically shifts the bandgap to lower frequency (as shown in Fig. 2.6, modulate f from 0.2 to 0.1). Therefore, photons traveling to the modulated Bragg mirror direction are bounced back. As long as the coupling time scale is much shorter than the decay time scale, we can assume the emitter couples to only one direction of the mode.

A quantum network consists of nodes to store and channels to distribute quantum coherence and entanglement(30). An efficient way to distribute entanglement and transfer quantum states between nodes is crucial for quantum computation, communication and metrology(31). Most experiments have been based on a probabilistic and heralded method to generate entanglement between nodes(32)(33)(34), despite that a deterministic method to realize quantum state transfer and entanglement distribution has been proposed using optical cavities early in 1996(35). The basic idea of this proposal(35) is to utilize strong coupling between a high-Q optical cavity and an atom to form individual nodes of the quantum

network. By applying laser beams, the internal state of an atom at the first node is first transferred to the optical state of the cavity mode. The generated photons leak out of the cavity, propagate as a wave packet along the transmission line, and enter an optical cavity at the second node. Finally, the optical state of the second cavity is transferred to the internal state of an atom by another laser beams. In this scheme, photons are used as flying qubits and atomic states are used as storage qubits. To suppress the spontaneous emission from the excited states, both the laser beam and the cavity mode are large dutuned from the atomic transition frequency, and thus the two ground states are coupled by virtual photon exchange. The experimental demonstration has not been possible until recently(36). Nevertheless, only a transfer fidelity of 6.3% is achieved. In (36), the maxixum possible transfer fidelity is bounded by 25%, since the atom couples to two degenerate modes with different polarization of the FP cavity, and the cavity is two-side symmetric cavity, thus photon leaks from both sides. This cavity approach also has a disadvantage in transfer speed, since in the strong coupling regime, photon has to be trapped inside the cavity for a while before it leaks out of the cavity. The photonic crystal waveguide approach, on the other hand, coherently couples the emitter to the waveguide mode at high fidelity and high speed.

Diamond nitrogen-vacancy(NV) center would be suitable as the quantum emitter. NV center has a electron spin triplet ground state (Fig. 2.7(e)). Each state is coupled to the nuclear spin. In what follows, we only use $|0>$ and $|1>$ spin state, denoted as $|g>$ and $|s>$, $|-1>$ state can be detuned away by electric field. The benefit of using NV center is that it has a nuclear spin qubits with long coherent time more than tens of milliseconds. We denote the nuclear spin qubits as $|\downarrow>$

and $|\uparrow>$. NV centers are well qualified as the definition of small quantum registers described in (37). The nuclear spin state is used as the storage qubit; electron spin, with coherence time of microsecond, is used as communication qubit. The photonic qubit, which is the presence or absence of photon, is used as flying qubits to transfer the quantum state or distribute entanglement between distant registers.

The Maps between nuclear spin qubit and electron spin qubit are proposed and experimentally demonstrated in (38). It utilizes the degeneracy between $|g\uparrow>$ and $|g\downarrow>$ and hyperfine splitting between $|s\uparrow>$ and $|s\downarrow>$. Hence there would be Larmor precession between states $|g\uparrow>$ and $|g\downarrow>$ when a weak magnetic field is applied perpendicular to the nuclear spin quantization axis. The hyperfine splitting of states $|s\uparrow>$ and $|s\downarrow>$ prevents the Larmor precession between the two states. $|s\downarrow>$ and $|g\downarrow>$ can be coupled using microwave ESR pulse. Therefore, a nuclear spin state would evolve as following, by a sequence of ESR π pulse and Larmor π pulse,

$$\begin{aligned}(\alpha|\uparrow>+\beta|\downarrow>)\otimes|s>&\longrightarrow \alpha|\uparrow s>+\beta|\downarrow g>\\ &\longrightarrow(\alpha|s>+\beta|g>)\otimes|\downarrow>\end{aligned} \tag{2.13}$$

In the current lambda-system, $|e>$ and $|s>$ states are resonantly coupled by a classical control light with Rabi frequency Ω. $|e>$ and $|g>$ are coupled to both the continuum modes of free space and to the modes of the photonic crystal waveguide. The coupling strength to each waveguide mode is denoted by $g_{i,k}$, subscript i for different modes of the waveguide, and k is the effective wave vector. Similar to the previous section, we divide the waveguide mode as $a_k^\dagger$-right propagating and $a_{-k}^\dagger$-left propagating waveguide modes. The left propagating mode is coupled irreversibly to

right propagating mode by modulated gratings on the photonic crystal waveguide. The right propagating mode, however, does not couple to left propagating mode. We further assume due to scattering loss from bragg mirror, this coupling is a Markovian process. Therefore, mater equation is valid to describe this process. The directional coupling can be accounted by Louvillan operators as

$$\mathcal{L}_{-kk} = -\frac{\beta}{2}(\sigma_{-kk}\sigma_{k-k}\rho - \sigma_{k-k}\rho\sigma_{-kk} + h.c.) \tag{2.14}$$

Here we also assumed an instantaneous coupling of left propagating mode to right propagating mode. This would be valid as long as the coupling time scale is much shorter than the decay time scale. Noting from the final result(Fig. 2.8(b)) that the total enhancement is around 30, and it is mainly due to slow group velocity in the waveguide. The Bragg mirror is on the scale of 10μm, so the coupling time is less than $10^{-12}s$, which is much faster than the decay time of electron state($10^{-9}s$). The spontaneous emission into vacuum, can be accounted similarly by $\mathcal{L}_{eg}$ and $\mathcal{L}_{es}$. Therefore,

$$\dot{\rho} = \mathcal{L}_{eg} + \mathcal{L}_{es} + \mathcal{L}_{-kk} + \frac{i}{\hbar}[\mathcal{H}_{sys}, \rho] \tag{2.15}$$

It is difficult to get analytical result out of this density matrix description, however, under the condition that

$$P_{jump} = \int dt(|c_e|^2\gamma' + |c_{-k}|^2\beta) << 1 \tag{2.16}$$

the process can be described using a non-Hermitian Hamiltonian and the dynamics can be solved analytically using the stochastic wave function method, with the wave function expressed as

$$|\psi >= c_e|e, 0 > +c_s|s, 0 > + \sum_{k>0}(c_k|g, k > +c_{-k}|g, -k >) \tag{2.17}$$

and

$$\dot{c}_s = i\Omega^* c_e \tag{2.18}$$

$$\dot{c}_e = -\frac{\gamma'}{2}c_e + i\Omega c_s + i\sum_{k>0} g_k(c_k + c_{-k}) \tag{2.19}$$

$$\dot{c}_k = -i\delta_k c_k + ig^* c_e + \frac{\beta}{2}\frac{|c_{-k}|^2}{|c_k|^2}c_k \tag{2.20}$$

$$\dot{c}_{-k} = -i\delta_k c_{-k} + ig^* c_e - \frac{\beta}{2}c_{-k} \tag{2.21}$$

Now we consider the mapping from electron spin state to photonic state by assuming the system starts from $c_s(0) = 1$. Plug the solutions of equation 2.20 and 2.21 into 2.19, we get

$$\dot{c}_s = i\Omega^* c_e \tag{2.22}$$

$$\dot{c}_e = -\frac{\gamma' + \gamma_{wg}}{2}c_e + i\Omega c_s \tag{2.23}$$

The additional decay term in $\dot{c}_e$ is identified decay rates into right-propagating waveguide mode. And $\gamma_{wg} = |g_k^i|^2 L/v_g^i$, where $v_g^i = d\omega_k^i/dk$ is the group velocity of the ith mode, which satisfies $\omega_k^i = \omega$. Therefore, the enhancement factor (α) takes the same Expression 2.4, and the storage and retrieval efficiencies calculated from the previous section are all valid. The only difference is that the sum of the all possible modes (denoted by i) now excludes the left-propagating mode.

For complicated photonic crystal waveguide structures in three-dimensional, there is no analytical solution for γ'. The atomic transition rate under dipole interaction in a quantum mechanical framework can be exactly solved classically by calculating the power emitted from a dipole source (40). Therefore, same as the previous section, α and β-factors can be obtained from 3D FDTD simulation. In quantum information, β corresponds to the fidelity of the process.

We simulate the quantum emitter as a classical dipole, using a monitor on the right end of the waveguide to record the emitted power through the waveguide. We also monitor the total power emitted by the dipole. The propotion of the above two numbers gives the maximum fidelity under matched control pulse. The coupling from the left propagating mode to the right propagating mode can be in general realized using first order grating(41). However, the scattering loss in this case is large (20%) and is due to phase mismatch between the left propagating mode and the Bragg mirror mode. The challenge is to design a novel bragg mirror to couple the left propagating mode to right propagating mode with as low scattering loss as possible.

To achieve this, we propose "modulated Bragg mirror" approach: keep the period of the grating unchanged and increase the Bragg mirror strength by modulating the fraction ratio of each period The underlying physics behind this strategy will be discussed in Chapter 3. We simulate the nanocrystal NV center as a classical dipole. To account for the nanocrystal, we also simulated it as a dipole embedded in a sphere with index 2.5, diameter 50nm. b is the width of the photonic crystal waveguide and is used to match the optimal frequency to the zero phonon line of NV center(637nm). Fig. 2.8(a) shows the fidelity we can get under this modulated bragg mirror design. The nanocrystal would shift the curve to lower frequency since it contains high index material. By slightly changing the width b from 270nm to 265nm. We can shift the curve back to the optimal point. With almost 98% fidelity, the photon will be coupled to the right propagating waveguide mode. Therefore, in the reverse mapping process, a maximum fidelity of 98% is possible by applying a time reversed control pulse of the mapping process. The total

enhancement shows the mapping process would be 30 times faster.

For normal waveguide without modulated Bragg mirror on one side, electron spin state will be mapped to symmetric photonic state $a_k^\dagger + c_{-k}^\dagger$. This causes great difficulty for the reverse mapping process since incoming photonic state must be split into two symmetric pulses arriving from both sides, otherwise the fidelity will be bounded by 50%. Using current directional photonic crystal waveguide, the electronic spin state couples to the right propagating mode strongly. Therefore, in the reverse mapping process, it becomes possible to store the incoming photon from one side with high fidelity.

Having achieved an efficient mapping between electron spin state $\alpha|s> + \beta|g>$ and photonic state $\alpha|1> + \beta|0>$, "Map" in Fig. 2.9 shows how to map the nuclear spin qubit to flying qubit. Together with the inverse Map, state transfer would be realized from one register to the other. Similarly, deterministic entanglement generation is also possible by mapping to entangled photons into two distant quantum registers. "ENT" in Fig. 2.9 demonstrates how to entangle the nuclear spin qubits of two NV centers, utilizing two entangle photon pairs in Bell state.

2.4 Summary

In summary, we first demonstrated a broadband, loss-free, on chip slot-waveguide QED system that can operate at high photon collection efficiency $\beta \sim 94\%$ (corresponding to cooperativity of 16) and a spontaneous emission enhancement of $\alpha \sim 100$, at a moderate slot width of 20nm. We have also shown that, in

experimentally more accessible configurations, high coupling efficiencies can be achieved. The broadband nature of wQED system makes it an attractive alternative to cQED since it does not require any tuning mechanism, and it could be beneficial for applications in spectroscopy and multicolor information processing. In such system, all the information of the atomic states is coherently extracted into the waveguide mode with high fidelity.

Second, with photonic crystal nanobeam waveguide, we had more flexibility to control the light and facilitate the light-emitter interactions. We demonstrated an easy scheme (free from splitting photons to both directions) that enables a high fidelity state transfer and entanglement distribution between distant diamond NV centers. NV centers are suitable, but not exclusive examples of the small quantum registers in the current scheme. This waveguide based approach is also valid for variety types of quantum emitters, such as quantum dots or superconducting qubits.

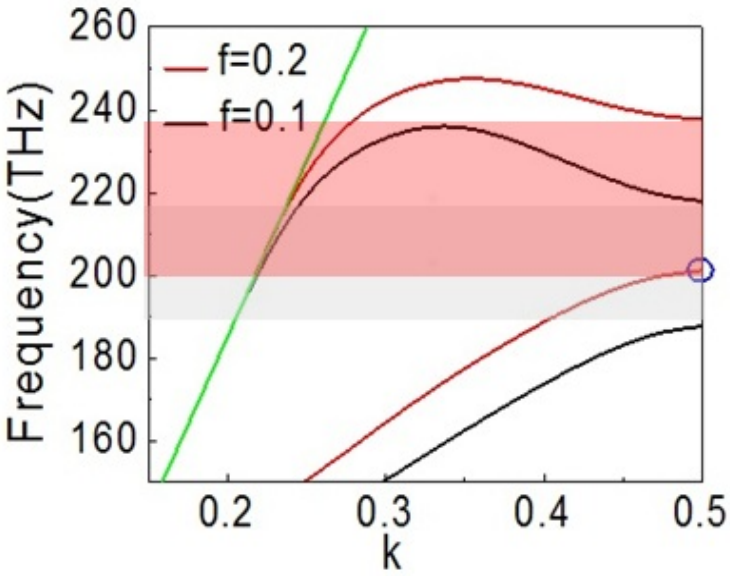

Figure 2.6.— Schematics (top view) of a photonic crystal nanobeam waveguide. It is a periodicaly perforated ridge waveguide. The holes can be any shape. The idea is to create a periodic index change between the holes and the rest.

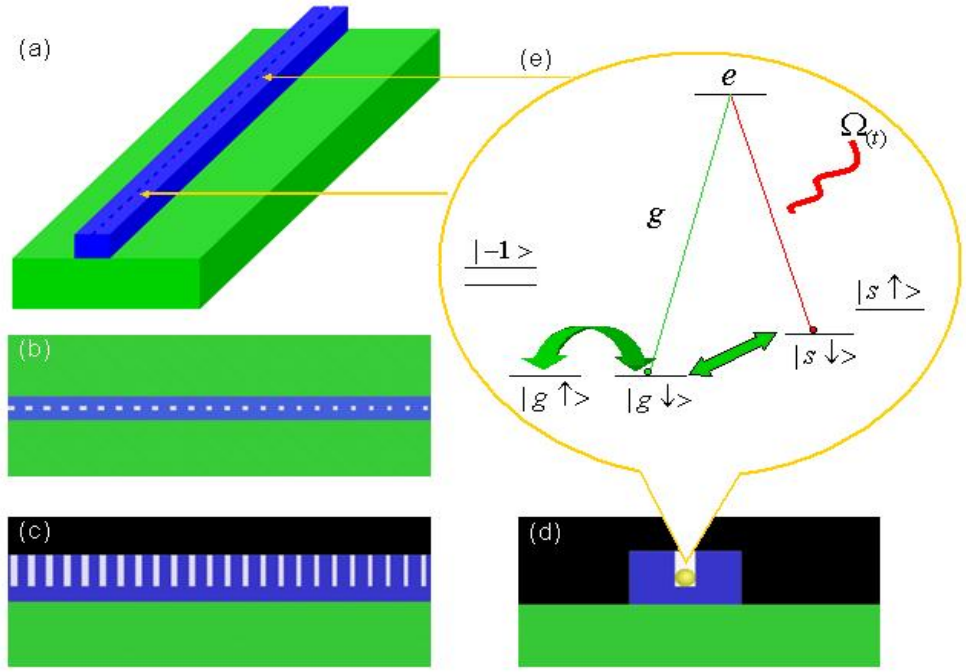

Figure 2.7.— (a)A photonic crystal waveguide on chip, each period contains a slot with width of 50nm. Grating period is fixed, while the length of the slots are modulated in order to suppress scattering and adiabatically couple the left propogating light mode to right propogating mode. Two nanocrystal diamond NV centers are placed in the slots at both ends of the waveguide. (b)&(c)Top and side view of the waveguide, a modulation in the length of the slots can be seen. (d) Front view of the slot that contains a diamond nanocrystal. (e) Illustration of electron and nuclear spin levels of NV centers.

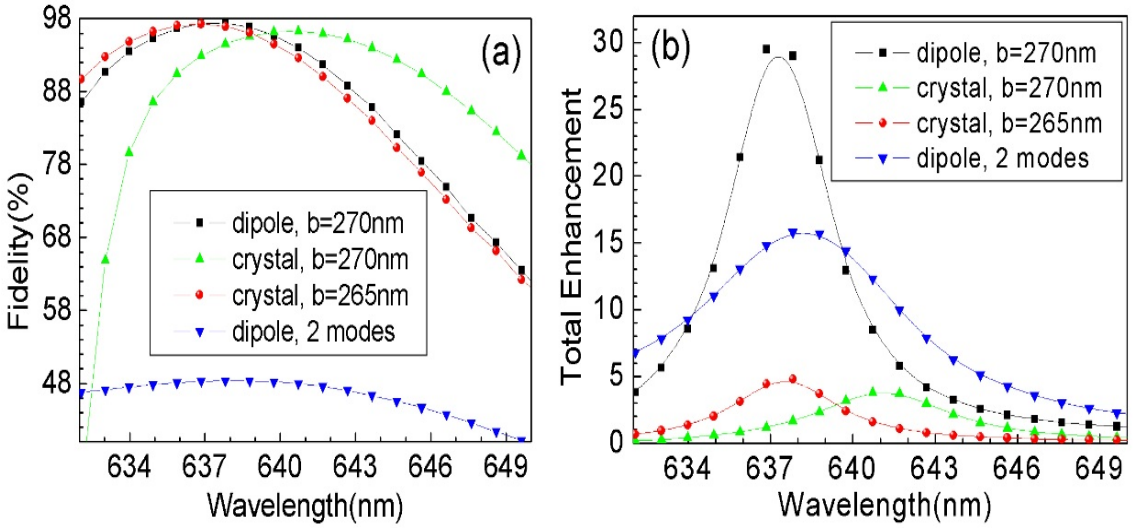

Figure 2.8.— (a)Quantum state mapping fidelity using photonic crystal waveguide. Black, green and red curves are for waveguide with modulated Bragg mirror on one side in order to couple left propagating mode to right propagating mode. Blue curve is normal photonic crystal waveguide, hence emitted photon would couple into both left and right propagating mode, and the fidelity is bounded by 50%. Black curve is simulated using a dipole source, waveguide width is 270nm; green is simulated using a dipole source imbedded inside a nanocrystal with index 2.5(diamond), nanocrystal diameter is 50nm, waveguide width b is 270nm; red curve is the same as green curve except that the waveguide width is adjusted to be b=265nm so that the peak is positioned at the zero phonon line (637nm) of NV center. (b) Spontaneous emission enhancement of each condition in (a). For dipole case(black and blue), total enhancement is compared with dipole in free space, for dipole embedded in nanocrystal case(green and red), the enhancement is compared to dipole embedded in bulk dielectric medium with index 2.5.

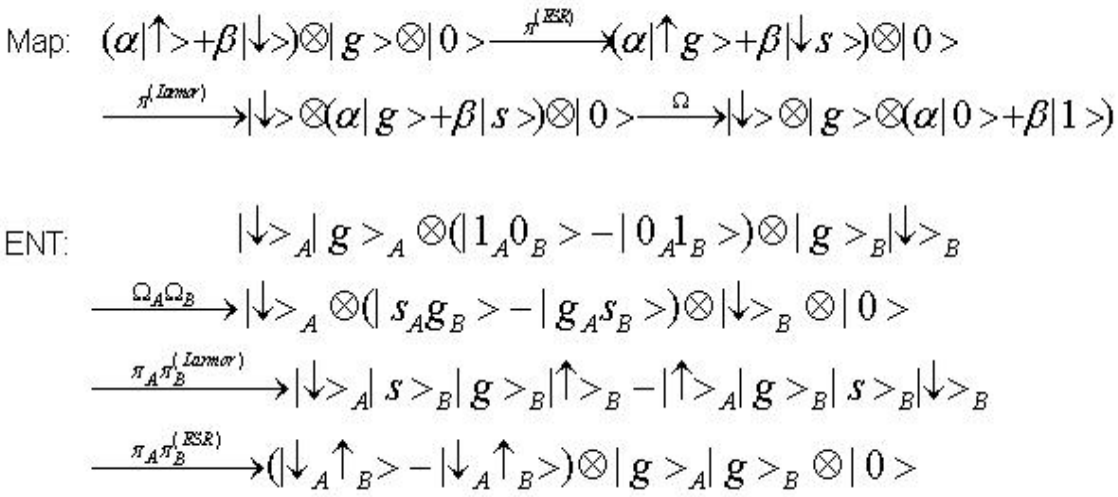

Figure 2.9.— Map operation from nuclear spin state to photonic states. ENT (entanglement) generation of two nuclear spin qubits.

Chapter 3

Nano-scale Optical Structures for Enhancement of Light and Matter Interactions - Cavities

3.1 Introduction

In Chapter II, we studied optical waveguides, which guide light by index contrast. What will happen if we bend a ridge waveguide and form a ring? As we can imagine, light will be guided by the waveguide and circles around until its energy vanishes. In this case, if an emitter is placed in the ring, the guided light will interact with the emitter once every time it circles. As a result, the total interaction strength is effectively enhanced.

There are in general two classes of optical resonators. The first class is

morphology based optical resonators, ring resonators as an example. Optical light trapped inside the resonator forms whispering-gellery-modes (WGM), by the morphology of the resonator. The other class is Febry-Perot type resonator. Light is bounced back and forth between two reflectors or equivalents. Metals suffer a huge loss at optical wavelength. An alternative form of reflectors are the photonic crystal structures (or Bragg reflectors) when operating inside the bandgap, as we discussed in Chapter 2. Cavities formed by Bragg reflectors are called photonic crystal cavities.

The two figures of merit for an optical cavity is Quality factor, defined as $Q = \omega_0 \frac{\text{Energy stored}}{\text{Power loss}}$, and mode volume, defined as $V = \int \mathrm{d}V \epsilon |\mathbf{E}|^2 / [\epsilon |\mathbf{E}|^2]_{\max}$. High quality factor ($Q$), small mode volume ($V$) optical cavities provide powerful means for modifying the interactions between light and matter(45), and have many exciting applications including quantum information processing(46), nonlinear optics(47), optomechanics(49), optical trapping(50) and optofluidics(51).

3.2 Whispering-Gallery-Mode (WGM) Cavity

The design of a WGM cavity is straightforward. A general rule of thumb is that the larger the radius, the higher the Q-factor, but also the larger the mode volume V. It is in fact exactly because of the ease of design, and larger tolerance in fabrication accuracy in WGM cavities than in photonic crystal cavities, most applications are first realized in WGM systems. For example, diamond is a material extremely hard to fabricate, however, the existence of luminescent defects such as Nitrogen Vacancy (NV) centers, that can be used as a long-lived (spin-based) memory with optical read-out, makes diamond a promising platform for quantum information processing

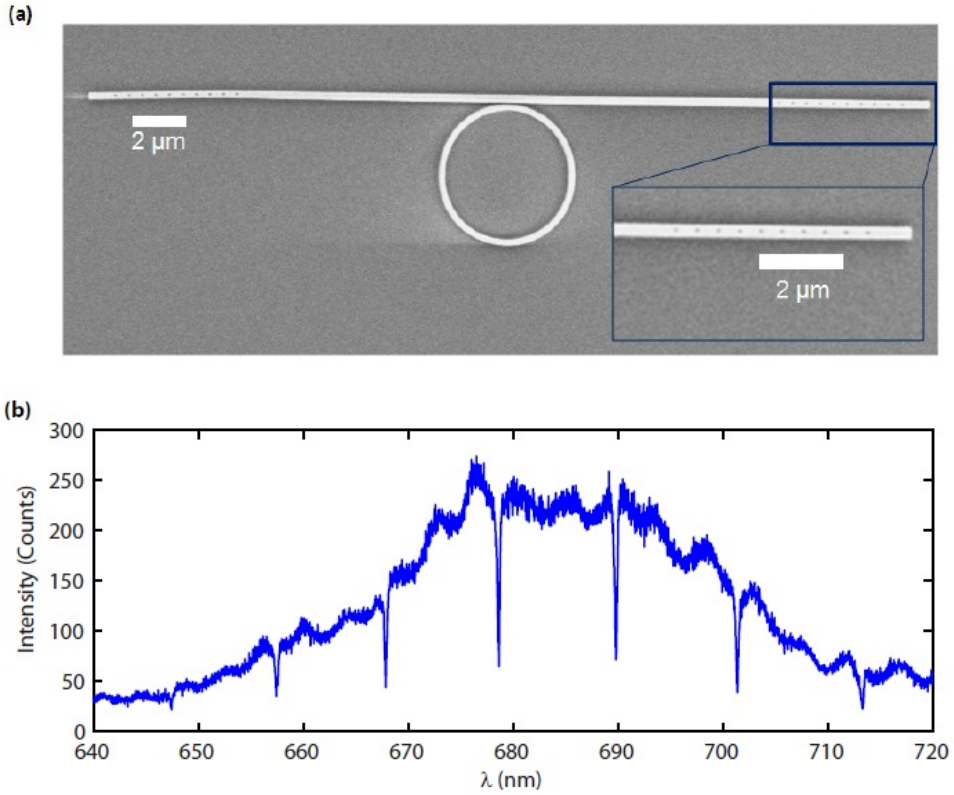

Figure 3.1.— (a) SEM image of a single mode ring resonator coupled to a waveguide containing second order gratings on both ends which facilitate collection of single photons via upward scattering. The ring diameter is 5 μm in the presented case, having a 245nm ring width. The gap between the waveguide and the ring is 100nm, while the waveguide itself has a width of 370nm. The devices are sitting on a SiO_2/Si substrate. Inset: Higher magnification image of the grating region. (b) Transmission spectrum through the waveguide via white light excitation exhibits a periodic mode structure. (Image courtesy Birgit Hausmann)

(42)-(44). In addition, diamond's bio-compatibility, and mechanically, chemically stable property also makes it a promising platform for biomedical applications.

To make a ring resonator with diamond, first a 20μm thick type Ib single crystal diamond slab (Element Six Inc.) was thinned to the preferred device layer thickness by an oxygen-based inductively coupled reactive ion etch (ICP RIE). E-beam (Elionix) exposes XR e-beam resist (spin-on-glass, Dow Corning) to form a mask and was transferred to the diamond film in a second etch. Fig. 3.1 shows a scanning electron microscope (SEM) image of representative diamond ring resonators on SiO_2/Si substrate.

We monolithically fabricated ring resonators and optical waveguides and thereby provided efficient and robust in- and out-coupling of light to the resonator with embedded single NV centers. The waveguides contain second order gratings on each end to facilitate the free-space coupling of photons (Fig. 3.1a). Second order grating is a form of photonic crystal. It couples light guided by the waveguide to the vertical direction by canceling the propagating momentum with Bragg mirrors. We characterized the structure by coupling the light from a broadband white light source into one grating and by collecting transmitted light from the other grating. The transmission spectrum shows regularly spaced dips corresponding to the different (longitudinal) resonant modes of the ring resonator (Fig. 3.1(b)). We extracted a Q-factor of Q$\sim$2500 for the resonance at $\lambda = 689.8$nm. Here, we operate close to critical coupling where the decay rate to the waveguide would equal the intrinsic field decay rate of the resonator. The mode volume of the ring resonator was obtained from FEM simulations: $V = 28(\lambda/n)^3$, when the dipole is placed in the field maximum with optimal polarization (aligned with the E-field of the cavity mode).

Combining this value with the Q-factor we measured, we estimate the Purcell factor of

$$\alpha = \frac{3}{4\pi^2}(\frac{\lambda}{n})^3\frac{Q}{V} \simeq 9 \tag{3.1}$$

3.3 Photonic Crystal Nanobeam Cavity

Photonic crystal cavities (PhC)(52)(53) have demonstrated advantages over other cavity geometries due to their wavelength-scale mode volumes and over-million Q-factors(54)-(62). While the small mode volumes of PhC cavities can be achieved in a straightforward way, the high Q designs have been challenging. Different methods have been developed to describe the origin of high-Qs, including Fourier space analysis(4)(77), the multipole cancelation effect(55), and the mode matching mechanism(56)-(80). Ultra-high Q factors are typically obtained using extensive parameter search and optimization(60)-(65), though inverse engineering approaches have also been explored(58)-(64). Large computational cost, in particular the computation time, needed to perform the simulation of high-Q cavities make this trial based approach inefficient. Inverse design engineering, in which the physical structure is optimized by constructing specific target functions and constraints, has also been proposed(58)(59). A design recipe based on the desired field distribution is proposed in (78).

1-D PhC nanobeam cavities (schematics in Fig. 3.2(a)&(b)) have recently emerged as a powerful alternative to the slab-based 2-D PhC cavities(60)-(62). Nanobeams can achieve Qs on par with those found in slab-based geometries, but in much smaller footprint. Furthermore, they are natural geometries for integration

with waveguides, have small mass and are flexible.

In the following sections, we propose and experimentally demonstrate a *deterministic* method to design an ultra-high Q, wavelength-scale PhC nanobeam cavity. The design approach is deterministic in the sense that it does not involve any trial-based hole shifting, re-sizing and overall cavity re-scaling to ensure the ultra-high Q-factor of the cavity. Moreover, the final cavity resonance has less than a 2% deviation from the targeted frequency. Our design method requires only computationally inexpensive, photonic band calculations (e.g. the plane wave expansion method), and is simple to implement.

3.3.1 Analytical Model

In the most general case a nanobeam cavity consists of a section, with length L, that supports propagating modes, sandwiched between two Bragg mirrors within which the field attenuates (Fig. 3.2(a)). Light is confined by Bragg reflection in the waveguide direction and by total internal reflection (TIR) in the other two directions. Light that leaks through the waveguide direction can be suppressed by increasing the number of mirror pairs. Therefore, in order to maximize total-Q, the key is to minimize coupling of light to the radiation modes (Q_{rad} maximized). The radiated power (P_{rad}) can be expressed as an integral of the spatial Fourier frequencies within the light cone, calculated over the surface above the cavity: $P_{\mathrm{rad}} \propto \int_{<\mathrm{lightcone}} \mathrm{d}k(|\mathrm{FT}(H_z)|^2 + |\mathrm{FT}(E_z)|^2)$, where FT denotes the spatial Fourier transform and z is the direction perpendicular to the surface(4)(78). The challenge of high Q cavity design is to understand what field distribution minimizes P_{rad}, and

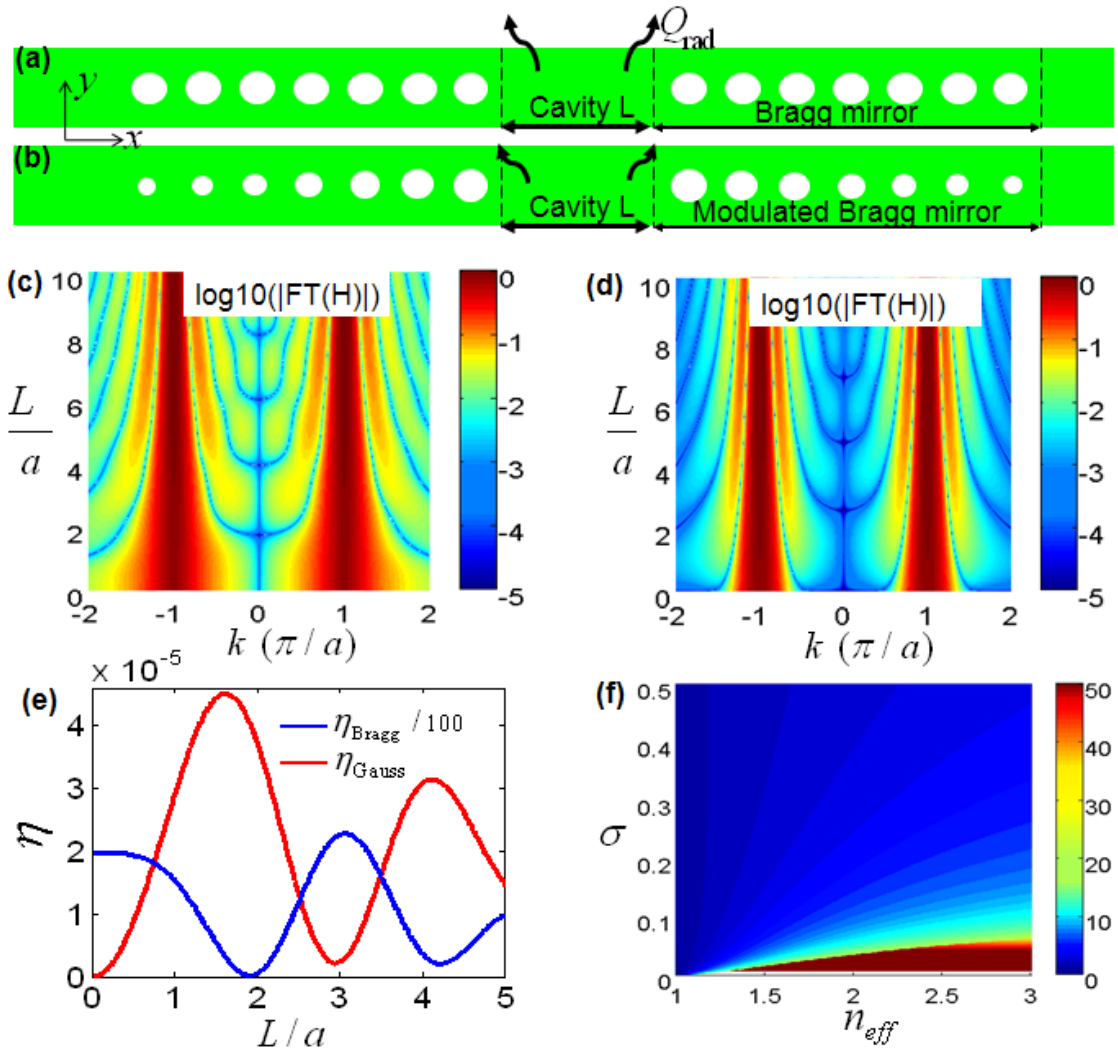

Figure 3.2.— (a)&(b) Schematics of a Bragg mirror cavity and a Gaussian mirror cavity. Q_{rad} indicates the radiation loss of the cavity mode. (c)&(d) Log(10) plot of fourier component distribution for different cavity lengths: (c) for Bragg mirror and (d) for Gaussian mirror. Both the field distribution and its Fourier transform are normalized such that $\int |H|^2 dx = \int |\text{FT}(H)|^2 dk = 1$. (e) The portion of the fourier components that are inside the lightline assuming an index proportion of 2.5 between the waveguide and the surroundings. (f) Log(10) plot of Q/V for different effective index and σ of a modulated Bragg mirror cavity with L=0.

how to realize this with realistic structures.

We start by considering the ideal field distribution that will minimize P_{rad}. Without loss of generality, we consider a TE-like cavity mode, which has H_z as the major field component. In the case of a conventional periodic Bragg mirror, the evanescent field inside the mirror can be expressed as $\sin(\beta_{\text{Bragg}}x)\exp(-\gamma x)$, where γ is the attenuation constant and $\beta_{\text{Bragg}} = \pi/a$. The cavity field inside the waveguide region can be represented as $\sin(\beta_{\text{wg}}x)$. Since only the spatial harmonics that lie inside the light cone couple to the radiation modes, tight localization of the spatial Fourier components far away from the light-cone would minimize P_{rad}. Therefore, we pick $\beta_{\text{Bragg}} = \beta_{\text{wg}}$ which also minimizes phase mismatch between the mirror and waveguide, thus reducing the scattering loss at the waveguide-mirror interface(70)(79)-(80). We note that these two functions are smoothly connected at the boundary, are divergence-less, and therefore are valid solution to the Maxwell equation.

In a Bragg mirror cavity with cavity length L, the field can be approximated, to the leading order, as $H_{\text{Bragg}} = \sin(\frac{\pi}{a}x)\{[1-\theta_{(|x|-L/2)}] + \theta_{(|x|-L/2)}\cdot\exp[-\gamma(|x|-L/2)]\}$, θ is the Heaviside function. The spatial Fourier distribution of the above field, for different length L, is shown in Fig. 3.2(c). Expectedly, the major Fourier component is at $k = \pm\pi/a$. Away from this point, the Fourier component decreases as $\propto \frac{1}{\pi/a-|k|}$, and then revives at $k = j\cdot\pi/a$ (j are integers). This is a natural result of the Fourier transformation of a field decaying inside Bragg mirror, that has sinusoidal field oscillations with an exponentially attenuating envelop function. As first proposed in (3), spatial frequencies within the light-cone can be minimized (Q maximized) if the field attenuation inside the mirror has a Gaussian shape. The total field can

be written as $H_{\text{Gauss}} = \sin(\frac{\pi}{a}x)\{[1 - \theta_{(|x|-L/a)}] + \theta_{(|x|-L/2)} \cdot \exp[-\sigma(|x| - L/2)^2]\}$. The spatial Fourier distribution of the Gaussian cavity (shown in Fig. 3.2(d)) is much more localized at $k = \pm\pi/a$. As a direct comparison, the fractions of the energy associated with spatial harmonics within the light-cone, η, in Fig. 3.2(c) and (d) are shown in Fig. 3.2(e). Evidently, η for the cavity with a Gaussian attenuation is more than 2 orders of magnitude smaller than that of the cavity with an exponential attenuation. It is worth noting that $L/a = 3$ corresponds to the well-known L3 cavity(3). Furthermore, we find the global minimum of radiation loss when $L = 0$, which is similar in so called point-shift cavities(63). We emphasize that $L = 0$ design minimizes the mode volume (V) of the cavity at the same time. Therefore, the optimal field distribution that maximizes Q/V figure of merit can be written as $H = \sin(\frac{\pi}{a}x)\exp(-\sigma x^2)$, while its Fourier transform takes the form $\text{FT}(H) = -i\{\exp[-(k+\pi)^2/4\sigma] - \exp[-(k-\pi)^2/4\sigma]\}/\sqrt{8\sigma}$. The cavity field has resonant frequency at $\omega/c = n_{\text{eff}}\pi/a$. Using these expressions for cavity fields, the radiated power (power loss), the total energy stored inside the cavity, cavity Q and mode volume, can be calculated from the analytical expressions. The figure of merit Q/V is shown in Fig. 3.2(f) in a log scale, with V normalized by wavelength-cubed. We see that arbitrarily high Q/V is possible for sufficiently small mirror strength.

The preferred Gaussian field-profile can be obtained from a simple exponential decaying field (typical of Bragg mirrors) by making the mirror strength γ a linearly increasing function of the position within the mirror, i.e., $\gamma = \sigma x$. We name such a mirror "Gaussian mirror". In the case of a dielectric-mode nanobeam cavity, this can be achieved by lowering the dielectric band-edges of each mirror segment by reducing the size of the holes away from the cavity center. Other approaches are possible,

for example, by increasing the width of the nanobeam(85). In order to prevent radiation loss, the oscillating part of the field, $\sin(\beta_{\text{Gauss}}x)$, should have a constant β_{Gauss} throughout the mirror. This condition is satisfied only if each segment of the Gaussian mirror has the same length (periodicity) a, and if the operating frequency (cavity resonance) is kept inside the bandgap of each segment.

We analyze the ideal tapering profile using plane wave expansion method and verify the results with 3D FDTD simulations. The dielectric profile of the structure in the middle plane of the cavity can be expressed as

$$\frac{1}{\epsilon(\rho)} = \frac{1}{\epsilon_{\text{Si}}} + (\frac{1}{\epsilon_{\text{air}}} - \frac{1}{\epsilon_{\text{Si}}})S(\rho) \tag{3.2}$$

with

$$S(\rho) = \begin{cases} 1 & |\rho - \mathbf{r}_j| \leq R \\ 0 & |\rho - \mathbf{r}_j| > R \end{cases}$$

$\mathbf{r}_j = j \cdot a\hat{x}$, a is the period, and $j = \pm 1, \pm 2...$ are integers. R is the radius of the hole. Using plane wave expansion method(81) in the beam direction ($\hat{x}$),

$$\frac{1}{\epsilon(x)} = \kappa_0 + \kappa_1 e^{iGx} + \kappa_{-1} e^{-iGx} + ... \tag{3.3}$$

where $G = 2\pi/a$. The zeroth (κ_0) and first (κ_1) order Fourier components can be expressed as (81)

$$\kappa_0 = \frac{f}{\epsilon_{\text{air}}} + \frac{1-f}{\epsilon_{\text{Si}}} \tag{3.4}$$

$$\kappa_1 = 2f(\frac{1}{\epsilon_{\text{air}}} - \frac{1}{\epsilon_{\text{Si}}})\frac{J_1(GR)}{GR} \tag{3.5}$$

J_1 is the first order Bessel function. Filling fraction $f = \pi R^2/ab$ is the ratio of the area of the air-hole to the area of the unit cell. We note that the above expressions are calculated assuming that the nanobeam cavity has infinite thickness (i.e 2D

equivalent case). Better estimation can be obtained by replacing ϵ_{air} and ϵ_{Si} with the effective permittivities.

The dispersion relation can be obtained by solving the master equation(82):

$$\frac{c^2}{\epsilon(x)}\frac{\partial^2 E}{\partial x^2} = \frac{\partial^2 E}{\partial t^2} \tag{3.6}$$

Inside the bandgap, the wavevector (k) for a given frequency (ω) is a complex number, whose imaginary part denotes the mirror strength (γ). For solutions near the band-edge, of interest for high-Q cavity design(74), the frequency can be written as $\omega = (1-\delta)\sqrt{\kappa_0}\pi c/a$ (δ is the detuning from the mid-gap frequency) and the wavevector as $k = (1+i\gamma)\pi/a$. Substituting this into the master equation, we obtain $\delta^2 + \gamma^2 = \kappa_1^2/4\kappa_0^2$. The cavity resonance asymptotes to the dielectric band-edge of the center mirror segment: $w_{\text{res}} \rightarrow (1-\kappa_1^{j=1}/2\kappa_0^{j=1})\sqrt{\kappa_0^{j=1}}\pi c/a$ (j represents the j^{th} mirror segment counted from the center), at which point the mirror strength $\gamma^{j=1} = 0$. γ increases with j. With $\epsilon_{\text{air}} = 1$ and $\epsilon_{\text{Si}} = 3.46^2$, we calculate in Fig. 3.3(a) the $\gamma - j$ relation for different tapering profiles. It can be seen that quadratically tapering profile results in linearly increasing mirror strengths, needed for Gaussian field attenuation(74). To verify this, we perform FDTD simulation and obtain the band diagram (Fig. 3.3(b)) and $\gamma - f$ relation (Fig. 3.3(c)). As shown in Fig. 3.3(d), linearly increasing mirror strength is indeed achieved after quadratic tapering.

Next, with the optimized tapering profile, the cavity is formed by putting two such mirrors back to back, leaving a cavity length L in between (Fig. 3.2(b)). Fig. 3.3(e) shows the simulated Q-factors for various Ls. Highest Q_{rad} is achieved at zero cavity length (L=0), which supports the prediction in (74) based on 1D model.

Third, we verify that the cavity mode has a Gaussian-like attenuation profile. Fig. 3.4(a) shows the H_z-field distribution in the plane right above the cavity, obtained from 3D FDTD simulation. As shown in Fig. 3.4(b), this field distribution can be ideally fitted with $H_z = \sin(\pi x/a)\exp(-\sigma x^2)\exp(-\xi y^2)$, with $a = 0.33$, $\sigma = 0.14$ and $\xi = 14$. The fitted value a agrees with the "period", and σ agrees with that extracted value from Fig. 3.3(d): $\sigma = \frac{\mathrm{d}\gamma}{\mathrm{d}x}\frac{\pi}{a} = 0.13$. Fig. 3.4(c) shows H_z distribution along the dashed line in Figs. 3.4(a) and 3.4(b). Therefore, we conclude that zero cavity length, fixed periodicity and a quadratic tapering of the filling fraction results in a Gaussian field profile, which leads to a high-Q cavity(74).

Finally, the current method results in a cavity whose resonance is asymptotically approaching the dielectric band-edge frequency of the central mirror segment (circled in Fig. 3.3(b)). The deviation from the band-edge frequency can be calculated using perturbation theory(82)(83):

$$\frac{\delta\lambda}{\lambda} = \frac{\int \delta\epsilon|\mathbf{E}_{\parallel}|^2 - \delta(\epsilon^{-1})|\mathbf{D}_{\perp}|^2 dV}{2\int \epsilon|\mathbf{E}|^2 dV} \tag{3.7}$$

$\mathbf{E}_{\parallel}$ is the component of $\mathbf{E}$ that is parallel to the side wall surfaces of the holes and $\mathbf{D}_{\perp}$ is the component of $\mathbf{D}$ that is perpendicular to the side wall surfaces of the holes. Under Gaussian distribution, the major field component $D_y = \cos(\pi/ax)\exp(-\sigma x^2)\exp(-\xi y^2)$, $\delta\epsilon$ perturbation occurs at $\mathbf{r} = \pm(j-1/2)\mathbf{a} + \mathbf{R}_j$, where $R_j = \sqrt{f_j ab/\pi}$ denotes the radius of the j^{th} hole (counted the center), with j=2,3...N, N is the total number of mirror segments at each side. Since the cavity mode has a Gaussian profile, $1/\sqrt{\sigma}$ characterizes the effective length of the cavity mode, and scales linearly with N, with a nonzero intercept due to diffraction limit. For large N, the intercept can be neglected, and thus $\sigma_N = \sqrt{20\times 0.14^2/N}$. Plug

the perturbation induced by the quadratic tapering from $f = 0.2$ to $f = 0.1$ into Eqn. 3.7, the frequency offset $\delta\lambda/\lambda$ vs. N can be obtained. Fig. 3.3(f) shows the frequency offset for different total number of mirror pairs (N), calculated from the perturbation theory, as well as using FDTD simulations. It can be seen that the deviation decreases as the number of modulated mirror segments increases, and is below 1% for $N > 15$.

3.3.2 A deterministic Design Recipe

Therefore, we verify that an ultrahigh-Q, dielectric-mode cavity resonant at a target frequency can be designed using the following algorithm:

(i) Determine a target frequency. For example in our case we want $f_{\text{target}} = 200\text{THz}$. Since the cavity resonant frequency is typically 1% smaller than the dielectric band-edge of the central segment, estimated using the perturbation theory, we shift-up the target frequency by 1%, i.e. $f_{\text{adjusted}} = 202\text{THz}$.

(ii) Pick the thickness of the nanobeam - this is often pre-determined by the choice of the wafer. For example, in our case, the thickness of the nanobeam is 220nm, determined by the thickness of the device layer of our silicon-on-insulator (SOI) wafer.

(iii) Choose periodicity according to $a = \lambda_0/2n_{\text{eff}}$, where n_{eff} is the effective mode index of the cavity and can be estimated by numerical modeling of a strip waveguide that nanobeam cavity is based on. However, we found that the absolute value of the periodicity is not crucial in our design, as long as there exists a bandgap. Therefore, we pick $n_{\text{eff}} = 2.23$, which is a median value of possible effective indices

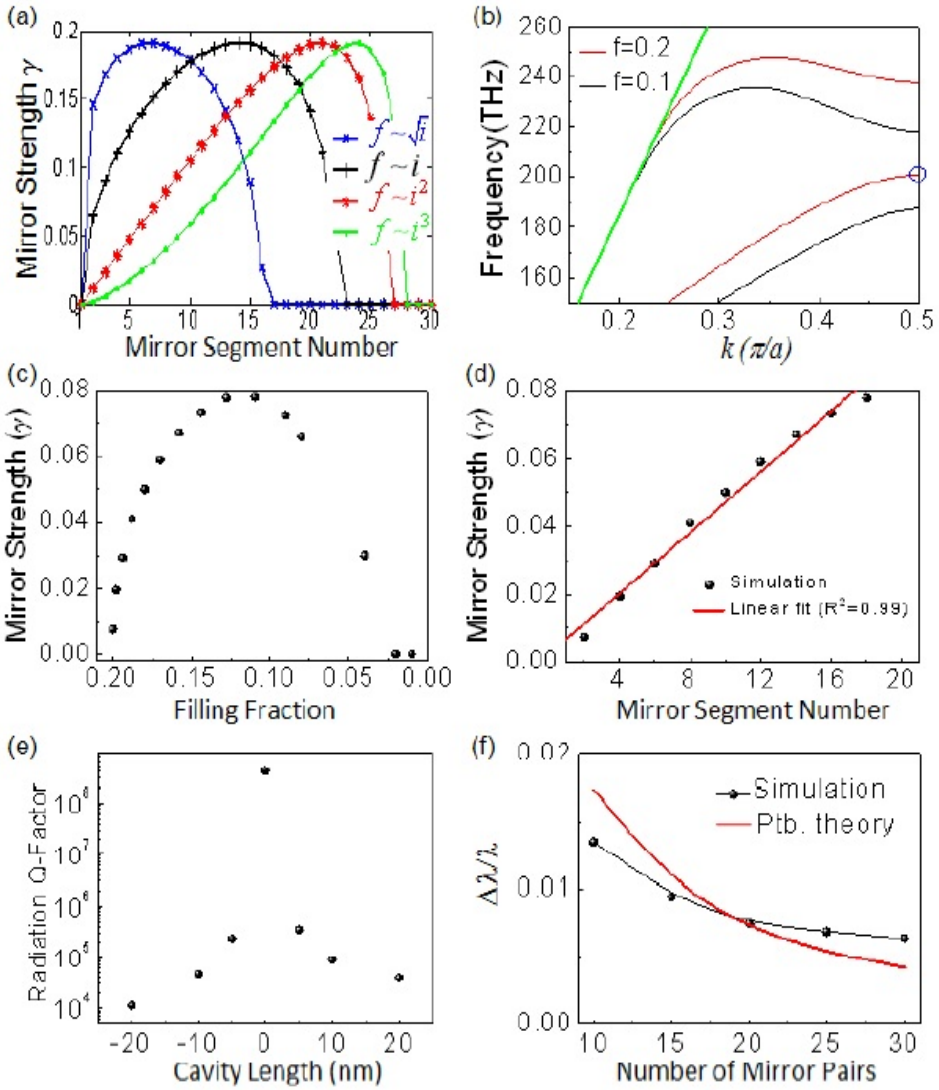

Figure 3.3.— (a) Mirror strengths of each mirror segment for different tapering profiles obtained from the plane wave expansion method ('1' indicates the mirror segment in the center of the cavity). (b) Band diagram of the TE-like mode for $f = 0.2$ and $f = 0.1$. The green line indicates the light line. The circle indicates the target cavity resonant frequency. (c) Mirror strengths for different filling fractions, obtained using 3D band diagram simulation. (d) Mirror strengths as a function of mirror number after quadratic tapering. (e) Radiation-Q factors for nanobeam cavities with different cavity lengths between the two Gaussian mirrors, obtained using 3D FDTD simulations. (f) Resonances of the cavities that have different total number of mirror pair segments in the Gaussian mirror, and their deviations from the dielectric band-edge of the central mirror segment, obtained using both FDTD simulation and perturbation theory.

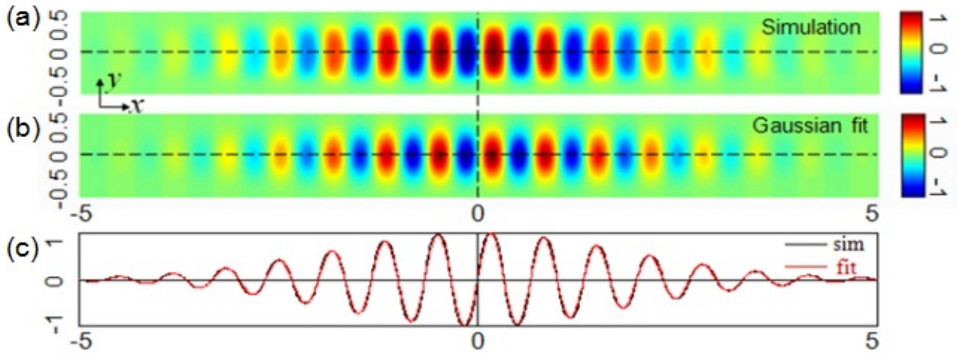

Figure 3.4.— (a) H_z field distribution on the surface right above the cavity, obtained from 3D FDTD simulation. The structure has dimension of $a = 0.33\mu m, b = 0.7\mu m$, the first 20 mirror segments (counted from the center) have fs varying from 0.2 to 0.1, followed by 10 additional mirror segments with $f = 0.1$. (b) H_z field distribution on the surface right above the cavity, obtained from the analytical formula $H_z = \sin(\frac{\pi}{a}x)\exp(-\sigma x^2)\exp(-\xi y^2)$, with $a = 0.33\mu m, \sigma = 0.14, \xi = 14$. (c) H_z field distribution along the dashed line in (a)&(b). Length unit in (a)-(c) is μm.

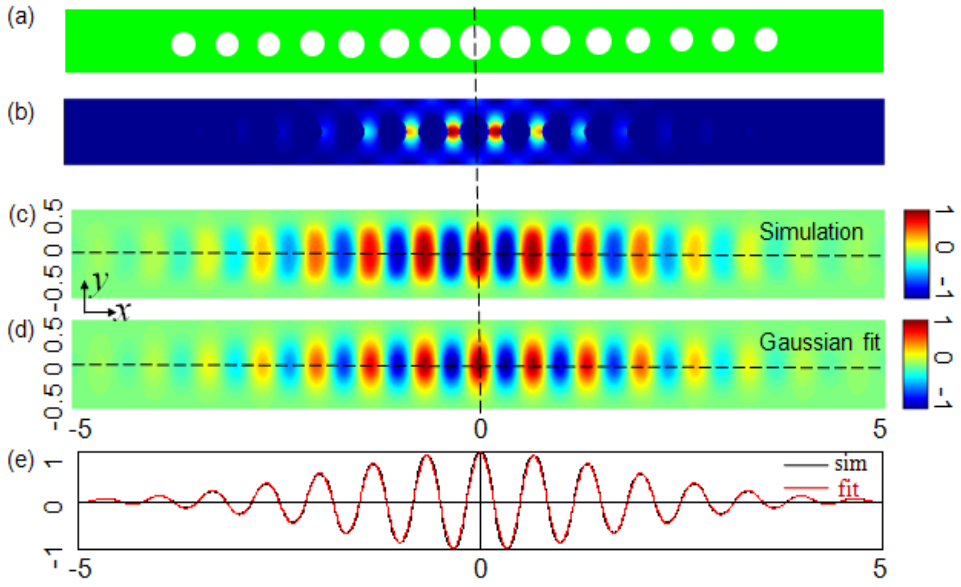

Figure 3.5.— (a) Schematic of the Gaussian nanobeam cavity, with an air hole in the symmetry plane (dashed line). (b) Energy distribution in the middle plane of the cavity obtained from 3D FDTD simulation. (c)&(d) H_z field distribution on the surface right above the cavity: (c) is obtained from 3D FDTD simulation and (d) is obtained from the analytical formula $H_z = \cos(\frac{\pi}{a}x)\exp(-\sigma x^2)\exp(-\xi y^2)$, with $a = 0.33\mu m, \sigma = 0.14, \xi = 14$. (e) H_z field distribution along the dashed line in (c)&(d). Length unit: μm.

in the case of free standing silicon nanobeam ($n_{\text{eff}} \in [1, 3.46]$). This results in $a = 330$nm.

(iv) Set the nanobeam width. Large width increases the effective index of the cavity mode, pulls the mode away from the light line, thus reducing the in plane radiation loss. On the other hand, a large beam width will allow for higher order modes with the same symmetry as the fundamental mode of interest. Using band diagram simulations, we found that the width of 700nm is good trade-off between these two conditions (Fig. 3.3(b)).

(v) Set the filling fraction of the first mirror section such that its dielectric band-edge is at the adjusted frequency: 202THz in our case. Band diagram calculations based on unit cells are sufficient for this analysis. We found that an optimal filling fraction in our case is $f_{\text{start}} = 0.2$ (Fig. 3.3(b)).

(vi) Find the filling fraction that produces the maximum mirror strength for the target frequency. This involves calculating the mirror strength for several filling fractions (Fig. 3.3(c)), each of which takes one or two minutes on a laptop computer. In our case we found that $f_{\text{end}} = 0.1$.

(vii) Pick the number of mirror segments (N) to construct the Gaussian mirror: we found that $N \geq 15$ (on each side) are generally good to achieve high radiation-Qs.

(viii) Create the Gaussian mirror by tapering the filling fractions quadratically from f_{start} (=0.2 in our case) to f_{end} (=0.1) over the period of N segments. From the above analysis, the mirror strengths can be linearized through quadratic tapering (Fig. 3.3(d)).

(ix) Finally, the cavity is formed by putting two Gaussian mirrors back to back, with no additional cavity length in between ($L = 0$). To achieve a radiation-limited cavity ($Q_{\rm wg} >> Q_{\rm rad}$), 10 additional mirrors with the maximum mirror strength are placed on both ends of the Gaussian mirror. We will show in the next section, no additional mirrors are needed to achieve a waveguide-coupled cavity ($Q_{\rm rad} >> Q_{\rm wg}$).

Besides the structure that was proposed in Fig. 3.2(b) (with L=0), the alternative structure which has the air-hole in the symmetry plane, as shown in Fig. 3.5(a), also satisfies (i)-(ix). Both structures result in dielectric-mode cavities, since the bandgap of each mirror segment red-shifts away from the center of the cavity, and thus a potential well is created for the dielectric band-edge mode of the central segment. The difference is that the energy maximum in the air-hole centered cavity is no longer located in the middle of the structure, but instead in the dielectric region next to the central hole (Fig. 3.5(b)). Fig. 3.5(c) shows the H_z field profile in the plane right above the cavity, obtained from FDTD simulation. Fig. 3.5(d) shows the fitted field profile using the exactly the same parameters that are used in the original structure shown in Figs. 3.4(a)-3.4(c), but with sine function replaced by cosine function. Fig. 3.5(e) shows the H_z distribution along the dashed line in Figs. 3.5(c) and 3.5(d).

Armed with the analytical field profile of the cavities: $H_z^{odd}(x) = \sin(\pi x/a)\exp(-\sigma x^2)$ (Fig. 3.4) and $H_z^{even}(x) = \cos(\pi x/a)\exp(-\sigma x^2)$ (Fig. 3.5), we can obtain the radiation losses and far fields of the cavities using the Fourier space analysis(4). The Fourier transforms can be analytically obtained $\mathrm{FT}(H_z^{odd}) = (\exp(-(k+\pi/a)^2/4\sigma) - \exp(-(k-\pi/a)^2/4\sigma))/i\sqrt{8\sigma}$ and $\mathrm{FT}(H_z^{\rm even}) = (\exp(-(k+\pi/a)^2/4\sigma) - \exp(-(k-\pi/a)^2/4\sigma))/\sqrt{8\sigma}$. Under $\sigma a^2 << 1$,

both distributions have their Fourier components strongly localized at $k = \pm\pi/a$, as is verified by FDTD simulations in Fig. 3.6(a) and 3.6(b). Since $H_z^{odd}(x)$ is an odd function, it always has a zero Fourier component at $k = 0$. Therefore, dielectric-centered cavities should have higher Q-factors. However, in high-Q cavity designs, $\sigma a^2 << 1$ is satisfied and thus both dielectric-centered and air-centered cavities have comparable Q-factors. FDTD simulation shows that the above H_z^{odd} and H_z^{even} cavities have $Q_{\text{tot}} = 3.8 \times 10^8$ and $Q_{\text{tot}} = 3.5 \times 10^8$ respectively. The mode volume of the H_z^{odd} cavity is $0.67(\lambda_{\text{res}}/n_{\text{Si}})^3$, smaller than the H_z^{even} cavity ($V = 0.76(\lambda_{\text{res}}/n_{\text{Si}})^3$).

The far field radiation patterns (obtained using FDTD simulations) of the two cavities are shown in Fig. 3.6(c) and 3.6(d). The powers, in both cases, are radiated at shallow angles ($> 70^\circ$ zenith angle) to the direction of the waveguide. The H^{odd} cavity has even less radiated power at small zenith angles, consistent with the above analysis. By integrating the zenith and azimuth angle dependent far field emission, we found that 32% and 63% of the power emitted to $+\hat{z}$ direction can be collected by a NA=0.95 lens, respectively for H^{odd} cavity and H^{even} cavity.

3.3.3 Dielectric-mode Nanobeam Cavities

Since the dielectric-centered H_z^{odd} cavity has smaller V than the H_z^{even} one, we focus our discussion in the H_z^{odd} case. Using the above design algorithm, we design the Gaussian mirror and put 10 additional mirrors with the maximum mirror strength on both ends of the Gaussian mirror to obtain the radiation-limited cavity ($Q_{\text{wg}} >> Q_{\text{tot}}$). We find in Fig. 3.7 that Q_{tot} increases exponentially and V increases

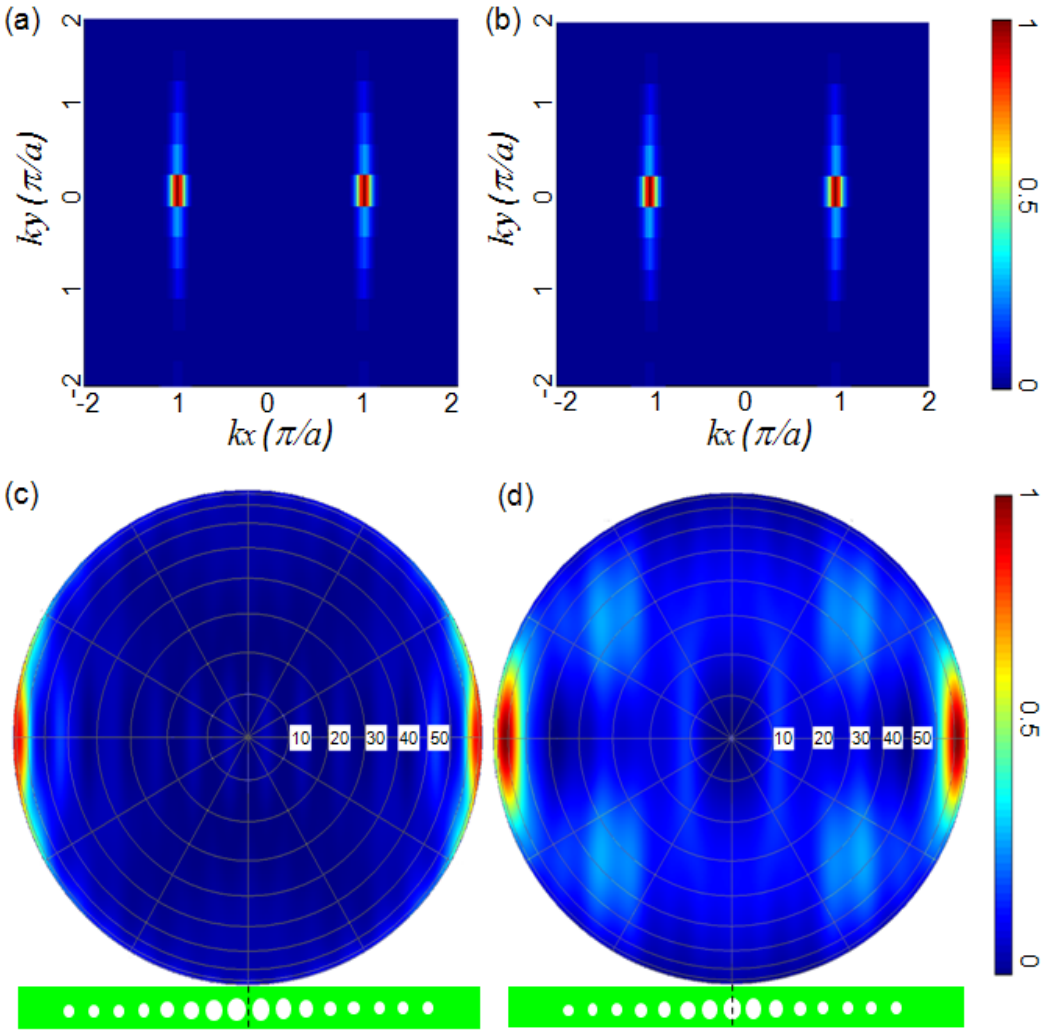

Figure 3.6.— (a)&(b) The distribution of the spatial Fourier components of the cavity mode, obtained from 3D FDTD simulation: (a) for the H_z^{odd} cavity and (b) for the H_z^{even} cavity respectively. (c)&(d) The far field profile of the cavity mode obtained from 3D FDTD simulation: (c) for the H_z^{odd} cavity and (d) for the H_z^{even} cavity respectively. The inset cavity structure shows the orientation of the waveguide direction in (c)&(d). Dashed line indicates the symmetry plane.

linearly as the total number of mirror pairs in the Gaussian mirror (N) increases. A record ultra-high Q of 5.0×10^9 is achieved while maintaining the small mode volume of $0.9 \times (\lambda_{\mathrm{res}}/n_{\mathrm{Si}})^3$ for $N = 30$.

Our design strategy has an additional important advantage over other types of photonic crystal cavities(3)-(73), that is: the cavity naturally couples to the feeding waveguide, as the hole radii decrease away from the center of the cavity. High-Q and high transmissions (T) cavities are possible with the above design steps (i)-(ix), with no additional "coupling sections" needed. We study T and Q_{total} dependence on the total number of mirror pair segments in the Gaussian mirror (N) in Fig. 3.7(b). Partial Q-factors ($Q_{\mathrm{rad}}, Q_{\mathrm{wg}}$) were obtained from FDTD simulations, and T was obtained using $T = Q_{\mathrm{total}}^2/Q_{\mathrm{wg}}^2$(82). As shown in Fig. 3.7(b), we achieved a nanobeam cavity with $Q = 1.3 \times 10^7, T = 97\%$ at $N = 25$.

The ultra-high Q mode that we deterministically designed is the fundamental mode of the cavity. Meanwhile, higher order cavity modes also exist. The number of higher order modes depends on the width of the photonic band gap and total number of mirror segments in the Gaussian mirror. To reduce the simulation time, we study the higher order modes of a waveguide-coupled cavity, that has a total number of 12 mirror pair segments, possessing a moderate Q-factor. Fig. 3.8(a) shows the transmission spectrum obtained from FDTD simulation, by exciting the input waveguide with a waveguide mode, and monitoring the transmission through the cavity at the output waveguide. The band-edge modes are observed at wavelengths longer than 1.6μm and shorter than 1.3μm. Figs. 3.8(b)-3.8(d) shows the major field-component (E_y) distribution of the three cavity modes. As expected, the eigenmodes alternate between symmetric and anti-symmetric modes.

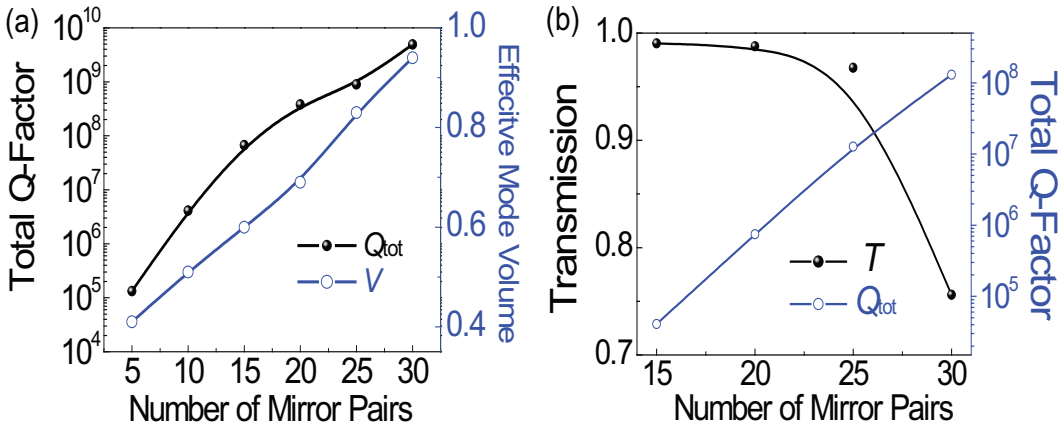

Figure 3.7.— (a) Total Q-factors (log(10) scale) and effective mode volumes $(V/(\lambda_{\mathrm{res}}/n_{\mathrm{Si}})^3)$ of nanobeam cavities for different total number of mirror pair segments in the Gaussian mirror. In each case, 10 additional mirror segments with f=0.1 (maximum mirror strength) are added on both ends of the Gaussian mirror. Therefore, the total-Q of the cavity is limited by radiation-Q. A record ultra-high Q of 5.0×10^9 is achieved with a Gaussian mirror that comprises 30 mirror segments and an additional 10 mirror pairs on both ends. (b) On-resonance transmissions and total Q-factors (log(10) scale) v.s the total number of mirror pair segments in the Gaussian mirror. In this case additional mirror pairs (10 of them) are not included. A record high-T (97%) and high-Q (1.3×10^7) cavity is achieved at $N = 25$.

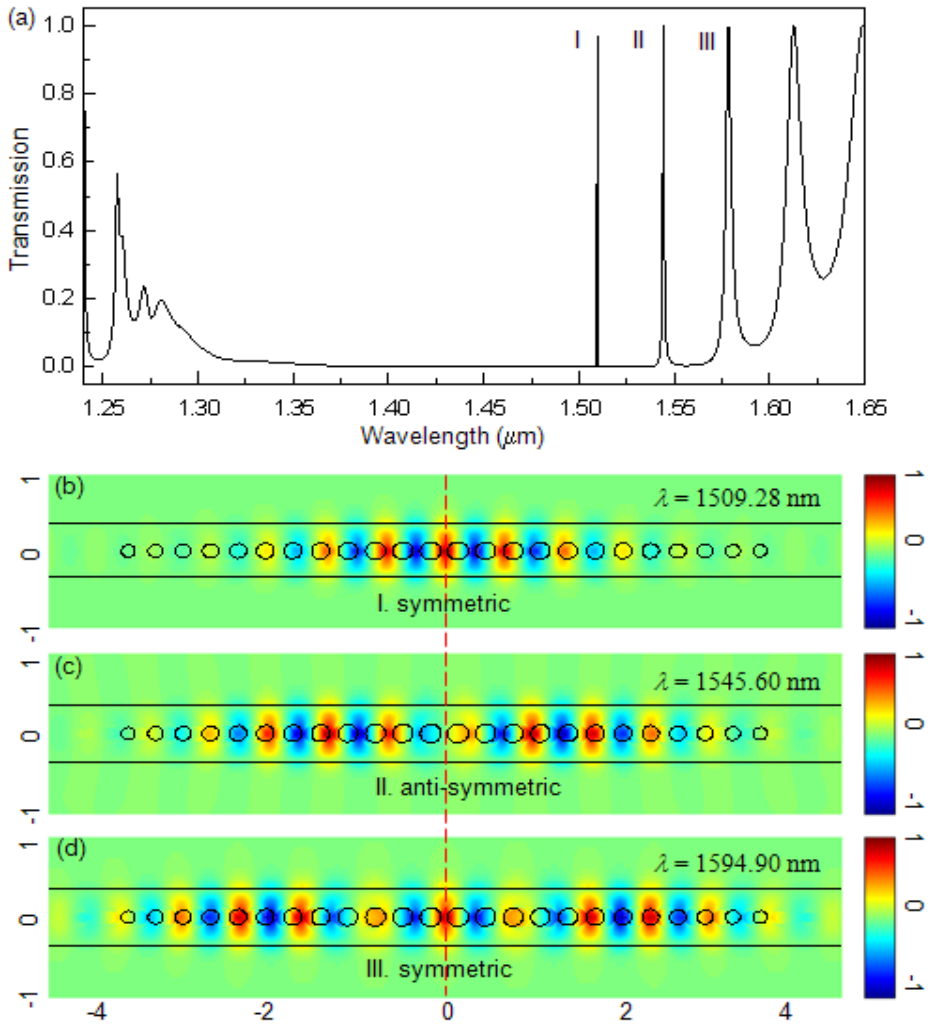

Figure 3.8.— (a) Transmission spectrum of the cavity from FDTD simulation. (b)-(d) The E_y field distribution in the middle plain of the nanobeam cavity. Resonances and symmetries of the modes are indicated in the plot. Symmetry plane is indicated by the dashed line. Length unit in (b)-(d) is μm.

Symmetry plane is defined perpendicular to the beam direction, in the middle of the cavity (dashed line in Fig. 3.8). The total Q-factors of modes I-III are 10,210, 1,077 and 286 respectively. Effective mode volumes of them are 0.55, 0.85 and 1.06 respectively. We note that transversely odd modes are well separated from the transversely symmetric cavity modes, hence were not considered in Fig. 3.8.

3.3.4 Air-mode Photonic Crystal Nanobeam Cavities

An air-mode cavity concentrates the optical energy in the low index region of the cavity. Therefore, these cavities are of interest for applications where strong interactions between light and material placed in the low index region of the cavity is required, including nonlinear optics(47), optical trapping(50), biochemical sensing(51) and light-atom interaction(84). The ultra-high Q air-mode nanobeam cavity is realized by pulling the air-band mode of photonic crystal into its bandgap, which can also be designed using the same design principles that we developed for dielectric-mode cavities. In contrast to the dielectric-mode case, the resonant frequency of the air-mode cavity is determined by the air band-edge frequency of the center mirror segment. Then, to create the Gaussian confinement, the bandgaps of the mirror segments should shift to higher frequencies as their distances from the center of the cavity increase. This can be achieved by progressively increasing the filling fractions of the mirror segments away from the center of the structure (instead of decreasing in the dielectric-mode cavity case). One way to accomplish this is to increase the size of the holes away from the center of the cavity. While this may be suitable for non-waveguide coupled (radiation-Q limited) cavities, it is not ideal for

a waveguide-coupled cavity, where high transmission efficiency through the cavity is required. For this reason, we employ the design that relies on tapering of the waveguide width instead of the hole size. Similar geometry was recently proposed by Ahn et. al.(85) for the design of a dielectric-mode photonic crystal laser.

The same design steps can be followed as in the dielectric-mode cavity case, with the following changes: First, the adjusted frequency (198THz) is 1% lower than the target frequency (200THz). (The thickness of the nanobeam is 220nm and period is 330nm, same as previous case.) Second, the nanobeam width at the center of the cavity is $w_{\text{start}} = 1\mu$m (Fig. 3.9(a)), with the hole radii kept constant at 100nm. Third, to create the Gaussian mirror, the beam widths are quadratically tapered from $w_{\text{start}} = 1\mu$m to $w_{\text{end}} = 0.7\mu$m, which produces the maximum mirror strength (band diagrams shown in Fig. 3.9(a)). This procedure involves calculating the mirror strength for several beam widths (Fig. 3.9(b)), each takes one or two minutes on a laptop computer. As shown in Fig. 3.9(c), the mirror strengths are linearized after the quadratic tapering. In order to achieve a radiation-Q limited cavity, 10 additional mirror segments are placed at both ends of the Gaussian mirror that has beam width $w_{\text{end}} = 0.7\mu$m.

Similar in the dielectric-mode cavity cases, H_z^{odd} and H_z^{even} air-mode cavities can be formed by placing the air and dielectric in the central symmetric plane of the cavity, respectively. Again, we will focus on H_z^{odd}, air-mode cavities and the conclusions will be valid to the H_z^{even} cavities as well. Fig. 3.10(a) shows the total Q of nanobeam cavities hat have different total number of mirror pair segments in the Gaussian mirrors. We have achieved a record ultra-high Q of 1.4×10^9, air-mode nanobeam cavity. As shown in Fig. 3.10(a), the effective mode volumes of the

air-mode cavities are much larger than the dielectric-mode cavities.

As we have pointed out, the tapering-width approach (as compared to tapering hole radii) offers a natural way of coupling the nanobeam air-mode cavity to the feeding waveguide. Since the width of the beam is decreasing, the cavity naturally couples to the feeding waveguide. We study T and Q_{total} dependence on the total number of mirror pair segments in the Gaussian mirror (N) using FDTD simulations. As shown in Fig. 3.10(b), we were able to design a nanobeam cavity with $Q = 3.0 \times 10^6, T = 96\%$ at $N = 25$.

The ultra-high Q cavity that we were able to design is the fundamental mode of the cavity. Higher order modes coexist with the fundamental modes inside the band gap. Fig. 3.11(a) shows the transmission spectrum of a waveguide-coupled air-mode nanobeam cavity, that has 15 mirror pair segments in the Gaussian mirror. The band-edge modes are observed at wavelengths longer than 1.6μm. The modes in the range of 1.2μm to 1.35μm are formed by the higher order band modes in Fig. 3.9(a). Figs. 3.11(b)-3.11(c) show the major field-component distribution (E_y) of the two cavity modes inside the bandgap. The total Q-factors of these two modes are 23,935 and 5,525 respectively. The effective mode volumes are 2.32 and 3.01 respectively.

3.3.5 Coupling between a Taper Lensed Fiber and the Nanobeam Cavity

The easiest way to characterize the nanobeam cavities are shown in Fig. 3.12. Light from tunable lasers are coupled to the naonbeam cavities through optical fibers, and collected by detectors, again via optical fibers. However, since silicon has a high

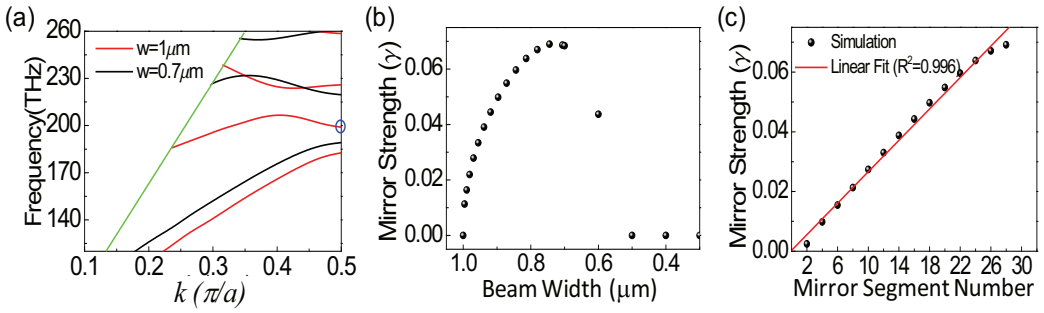

Figure 3.9.— (a) TE band diagram for an air-mode nanobeam cavity. Hole radii r = 100nm, a = 330nm, b=1μm (red) and b=0.7μm (black). (b) Mirror strengths for different beam widths. (c) Linearization of mirror strengths after quadratic tapering the beam widths.

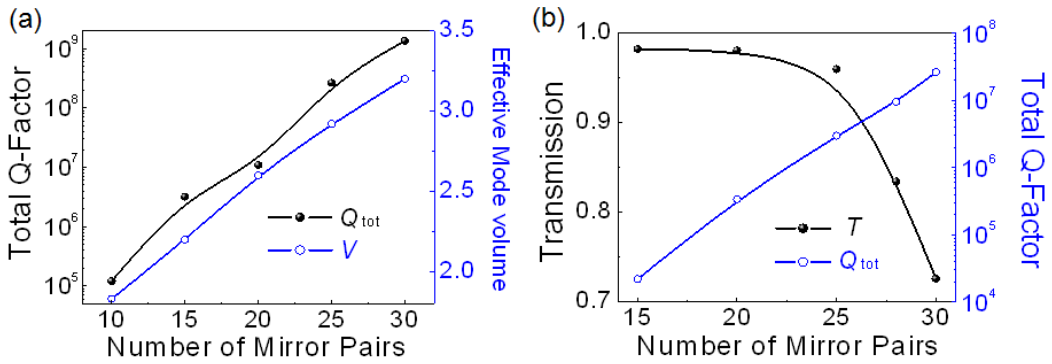

Figure 3.10.— (a) Total Q-factors (log(10) scale) and effective mode volumes $(V/(\lambda_{\rm res}/n_{\rm Si})^3)$ of the nanobeam cavities for different total number of mirror pair segments in the Gaussian mirror. In each case, 10 additional mirror segments with w=0.7μm are added on both ends of the Gaussian mirror, so that the total-Q of the cavity is limited by radiation-Q. A record ultra-high Q of 1.4×10^9 is achieved with a Gaussian mirror that comprises 30 mirror segments and 10 additional mirror pairs on both ends. (b) On-resonance transmissions and total Q-factors (log(10) scale) v.s the total number of mirror pair segments in the Gaussian mirror. In this case additional mirror pairs (10 of them) are not included. A record high-T (96%) and high-Q (3.0×10^6) cavity is achieved at $N = 25$.

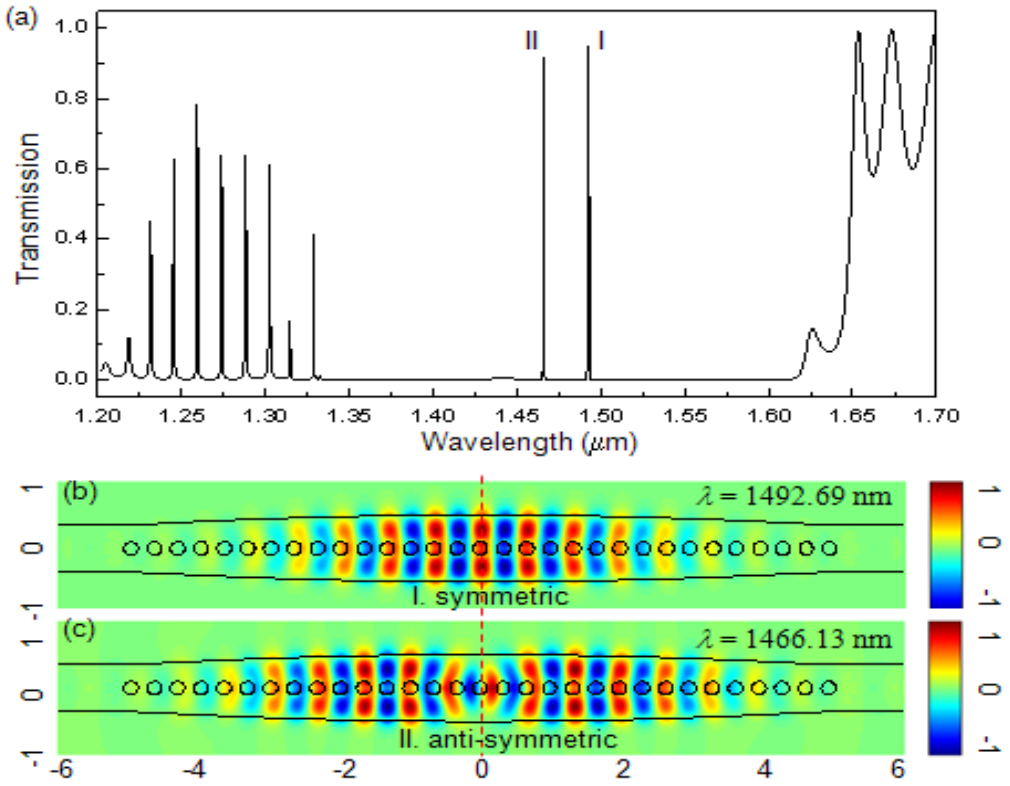

Figure 3.11.— (a) Transmission spectrum of the cavity from FDTD simulation. (b)&(c) The E_y field distribution in the middle plain of the nanobeam cavity. Resonances and symmetries of the modes are indicated in the plot. Symmetry plane is indicated by the dashed line. Length unit in (b)&(c) is μm.

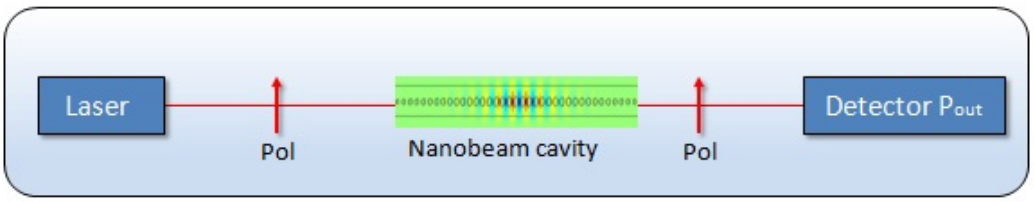

Figure 3.12.— Schematics of setup to characterize the nanobeam cavities. Pol denotes polarizers to filter out unwanted TM component.

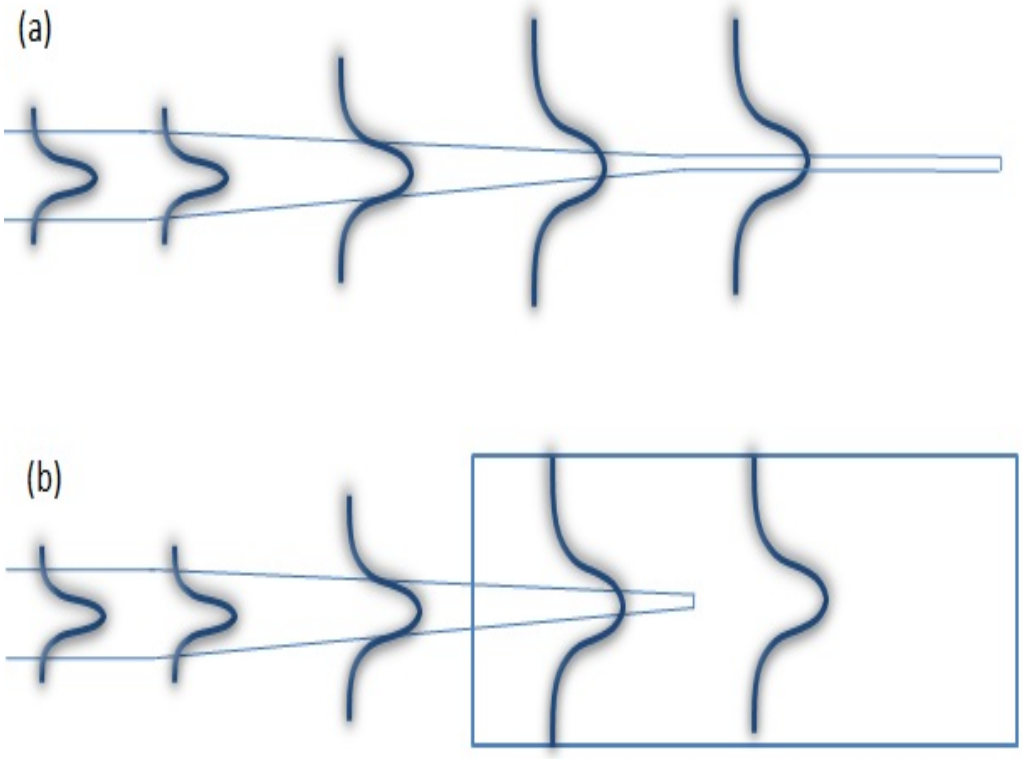

Figure 3.13.— Schematics of two possible mode-conversion structures for efficient light coupling. (a) The silicon waveguide is tapered to smaller width at which the optical mode extends to match the mode of a optical fiber. In this case, a symmetric structure is required, i.e. the whole structure needs to be capped by silica. (b) The silicon waveguide is tapered into a large polymer pad with lower index, and thus mode is adiabatically transformed from silicon waveguide to the mode of the pad, which matches well to the fiber.

refractive index, it tightly confines the optical mode to a sub-micron spot diameter (on the order of $R = \lambda/2n$). On the other hand, a fiber tip typically has a spot size on the order of microns at 1550nm. Therefore a spot size converter is required to facilitate efficient coupling from fiber tip to the nanobeam cavity. This is typically achieved by two methods, as illustrated in Fig. 3.13.

The first approach (Fig. 3.13(a)) is to taper the size of the silicon waveguide to a small width. As the width of the waveguide decreases, the mode extends. At an optimal width, the extended mode size will well match the fiber mode size (typically around $2\mu m$, commercial tapered the fiber).

The second approach couples the silicon waveguide mode to a large polymer waveguide pad (typically 2 or 3 microns width, material with smaller refractive index). As is shown in Fig. 3.13(b), the guided mode is adiabatically converted from the silicon waveguide's mode to the polymer pad's mode.

In our experiment, the silicon nanobeam waveguide has thickness $t = 220nm$, width $w = 550nm$ and is on a silica substrate. In various cases, the structure are capped by either silica(index 1.45), SU-8(1.58) or cytop(1.34). We will calculate the transmission efficiency in approach I and II respectively.

Approach I: Silicon waveguide is tapered down to w_2. The whole structure is capped by silica, SU-8 or cytop.

Approach II: Silicon waveguide intrudes into a SU-8 polymer pad with $2\mu m \times 2\mu m$ cross section. Inside the SU-8 pad, the silicon waveguide width is tapered from w_1 to w_2, and stops penetrating at w_2.

In both approach I and II, a taper-lensed fiber is in-line coupled to the end of the taper.

First we determine the the end of the tip width w_2. In approach I, it is determined by calculating its maximum collection efficiency by a NA=0.4 or 0.5 lens. In order to be collected by the lens, the end width w_2 should be reasonably small so that the mode is well extended, i.e. has a small effective NA. We will optimize the geometry according to TE case, and calculate the corresponding values for the TM cases at the same geometry. Fig. 3.14 shows the collection efficiency of a TE like mode by a lens with NA=0.4 and NA=0.5 respectively. On the maximum collection, w_2=130nm, 180nm and 210nm for nanobeam capped by silica, SU-8 and cytop respectively. Under these conditions, the collection efficiency for the TM like mode is, for silica: 0.81(NA0.4), 0.90(NA0.5) for SU-8: 0.64(NA0.4), 0.73 (NA0.5); for cytop: 0.61(NA0.4), 0.71(NA0.5). In approach II, we find that the mode overlap is unity between the mode of the silicon waveguide ($w_1 = 550\mu$m) and that of the same waveguide and additionally enclosed by a SU-8 pad. The end of the tip width w_2 is determined by overlapping the SU-8 pad modes with and without the silicon waveguide, which has a tip width w_2. Fig. 3.15 shows that a 50nm waveguide tip width in SU-8 pad has a near unity mode overlap both for TE and TM mode. Note that the facet reflection losses has been taken into account in the collection efficiencies.

To calculate the feeding efficiency from the tapered fiber to the waveguide, we launch a Gaussian mode which is focused by a lens with NA=0.4. Fig. 3.16, 3.17, 3.18 show the feeding efficiency from the taper lensed fiber to the fundamental mode of the silicon waveguide that is capped by silica, SU-8 and cytop respectively.

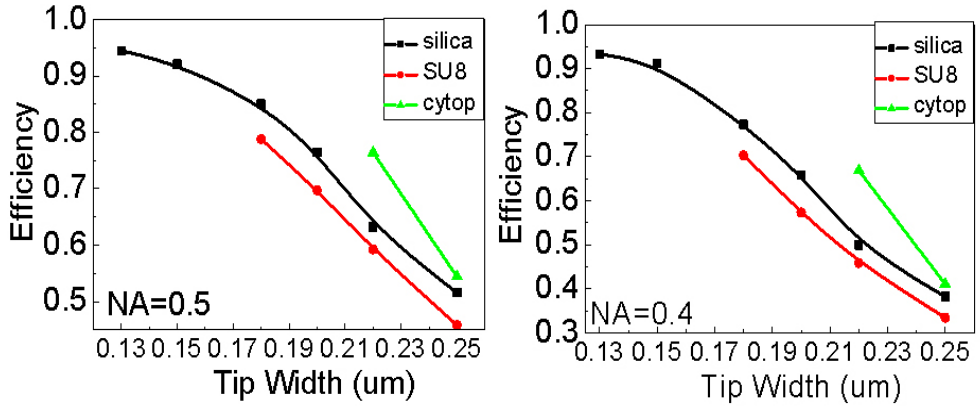

Figure 3.14.— The collection efficiency for a silicon waveguide with different tip width using a taper lensed fiber with NA=0.5(a) and NA=0.4(b) at 1550nm. In each case, the silicon waveguide has thickness 220nm, is on silica substrate and capped by silica, SU-8 or cytop.

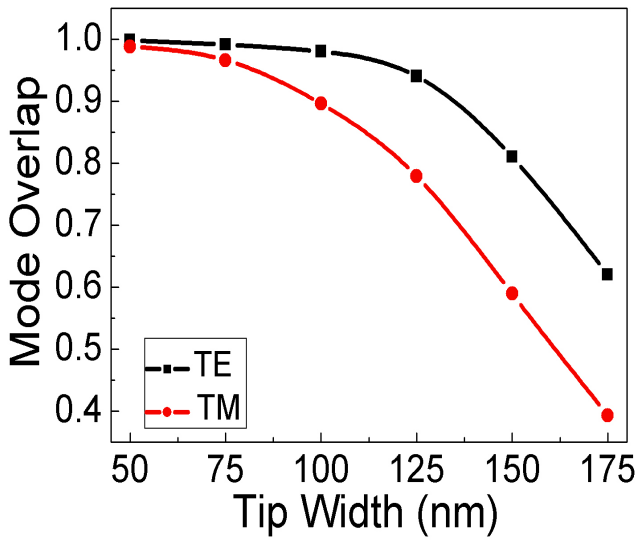

Figure 3.15.— The mode overlap between the SU-8 pad mode ($3\mu m \times 3\mu m$) with the silicon waveguide, which has a tip width as shown in the x axis.

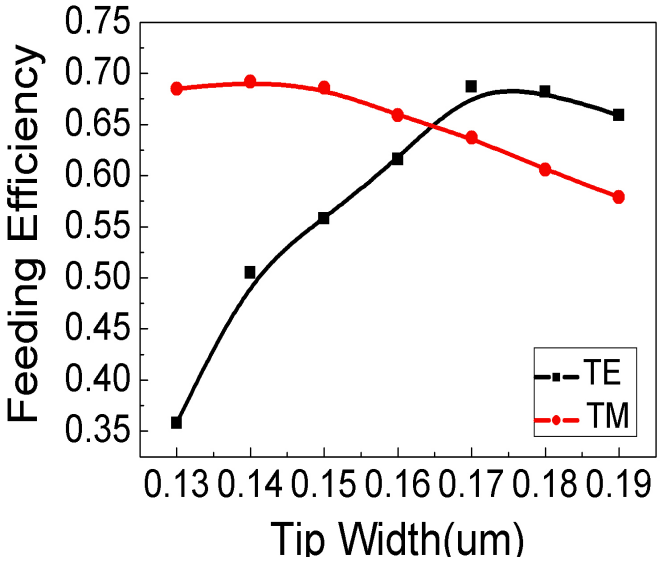

Figure 3.16.— The feeding efficiency from the taper lensed fiber with NA=0.4 to the silicon waveguide that is capped by silica and that has width as shown in the x axis.

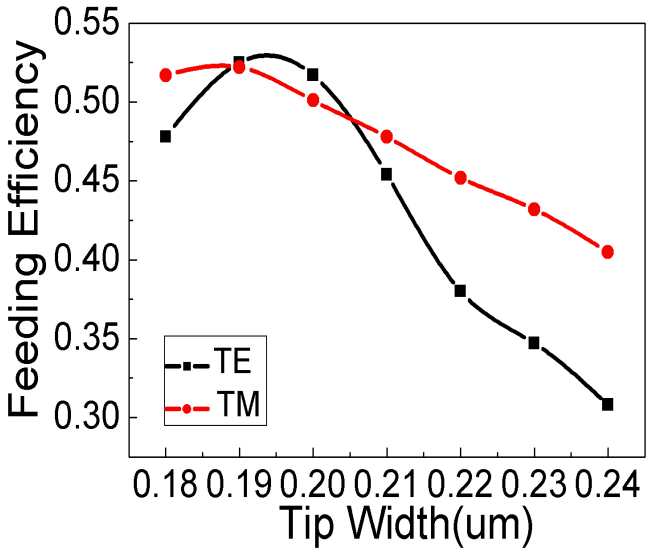

Figure 3.17.— The feeding efficiency from the taper lensed fiber with NA=0.4 to the silicon waveguide that is on silica, capped by SU-8 and that has width as shown in the x axis.

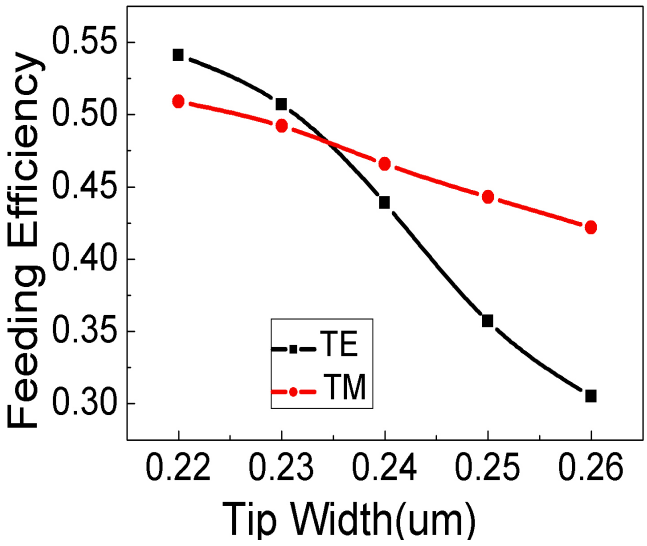

Figure 3.18.— The feeding efficiency from the taper lensed fiber with NA=0.4 to the silicon waveguide that is on silica, capped by cytop and that has width as shown in the x axis.

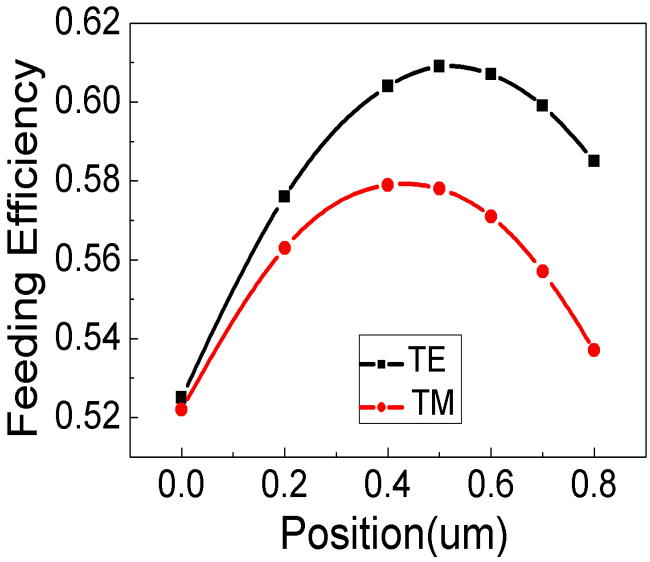

Figure 3.19.— The feeding efficiency from the taper lensed fiber with NA=0.4 to the silicon waveguide(with $w_2 = 0.19\mu m$) that is on silica and capped by SU-8. The x axis shows the vertical position of the fiber to the center of the silicon waveguide.

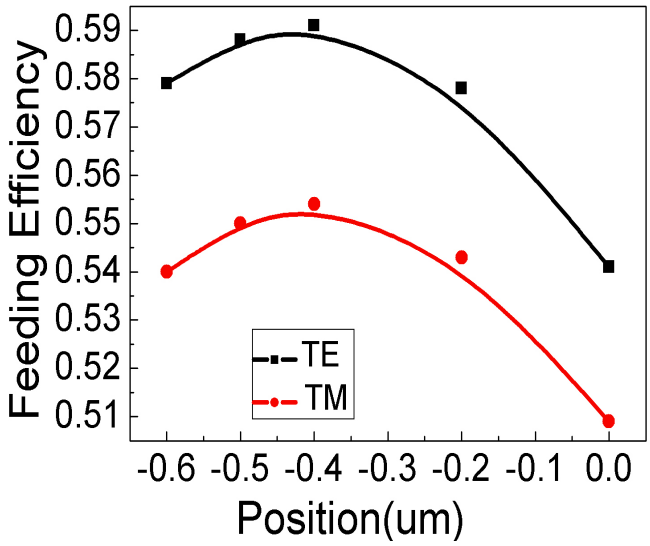

Figure 3.20.— The feeding efficiency from the taper lensed fiber with NA=0.4 to the silicon waveguide(with $w_2 = 0.22\mu m$) that is on silica and capped by cytop. The x axis shows the vertical position of the fiber to the center of the silicon waveguide.

Table 3.1: Collection effiency of the SU-8 pad mode by taper lensed fiber at 1550nm

pad size	NA 0.4 (TE)	NA 0.5(TE)	NA 0.4(TM)	NA 0.5 (TM)
2×2	0.71	0.83	0.72	0.83
2.5×2	0.86	0.86	0.84	0.81
3×2	0.78	0.88	0.78	0.87
3.5×2	0.80	0.89	0.80	0.89
4×2	0.82	0.90	0.82	0.89
3×3	0.85	0.92	0.85	0.92
4×4	0.84	0.92	0.84	0.92

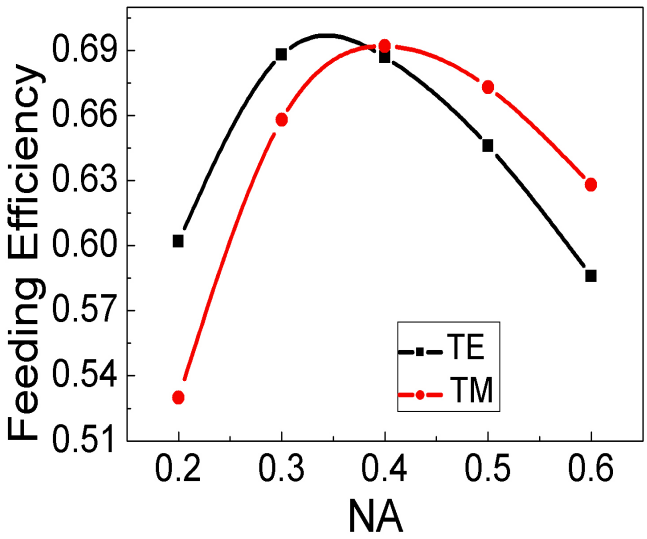

Figure 3.21.— The feeding efficiency from the taper lensed fiber with different NAs to the silicon waveguide that is capped by silica and that has width $w_2 = 0.17\mu m$ and $w_2 = 0.14\mu m$ for TE and TM cases respectively .

Table 3.2: Feeding efficiency from the taper lensed fiber to the fundamental mode of SU-8 pad at 1550nm

pad size	NA 0.4 (TE)	NA 0.5(TE)	NA 0.4(TM)	NA 0.5 (TM)
2×2	0.71	0.79	0.72	0.79
2.5×2	0.75	0.81	0.75	0.81
3×2	0.78	0.81	0.78	0.80
3.5×2	0.79	0.79	0.78	0.77
4×2	0.79	0.75	0.77	0.73
3×3	0.83	0.80	0.83	0.80
4×4	0.81	0.64	0.81	0.64

The taper lensed fiber is aligned to the center of the silicon waveguide. And apparently, for SU-8 and cytop cases, this would not be the optimal position due to the asymmetry of the geometry. Fig. 3.19 and Fig. 3.20 further show the vertical position of the fiber to the center of the silicon waveguide. Figs. 3.16-3.19 all assume the input fiber has a NA=0.4. Different NA lenses would concentrate the light into different spot sizes, the one match best with the waveguide mode would produce best feeding efficiency. Fig. 3.21 shows the feeding efficiencies as the NAs of the lenses change (waveguide is capped by silica). Note also that the facet reflection losses has been taken into account in the feeding efficiencies.

With the taper tip width determined by the collection of the fiber, next we calculate the mode conversion efficiency by the taper. In the simulation, the tapered region is divided into N small sections. The feeding waveguide mode is decomposed into all the supporting modes(guided and leaky) of the first section. They propagate at different phase velocity and are coherently added up at the end of the first section. Then it is again decomposed into all the supporting modes of the second section. This procedure goes succeedingly and eventually all the decomposed modes are overlapped with the final propagating mode at the end of the taper. This

Table 3.3: Taper efficiency-linear taper length $150\mu m$. The pad is $2um$ by $2um$.

type	w_2(nm)	TE in	TE out	TE total	TM in	TM out	TM total
silica	130	78.5%	80.8%	63.4%	97.4%	98.2%	95.6%
SU-8	180	86.7%	86.6%	75.0%	98.3%	98.3%	96.6%
cytop	220	88.2%	88.0%	77.6%	99.5%	99.6%	99.1%
pad	50	95.5%	95.4%	91.1%	98.7%	95.1%	93.9%

method converts 3D FDTD simulations to 2D mode solving and also eliminates the artificial reflections by the PML in 3D FDTD simulation. But this method does not account for the interference of the forward propagating field with back-reflected field. However as we confirmed, for all our taper designs below, the reflected field is more than 3 orders of magnitude smaller than the forward propagating field. In the output, waveguide is tapered down from w_1 to w_2. In the input, waveguide is tapered up from w_2 to w_1, exactly symmetric to the output case. The results of the fundamental mode conversion efficiency of a $150\mu m$ long taper are summarized in Table3.3 and Table3.4. Note that for the pad case, the loss due to the imperfect mode overlaps when the silicon waveguide core is terminated (as shown in Fig. 3.15) and when the pad is terminated have been included in the Table3.3 and Table3.4.

The loss is due to the coupling to the radiating modes, which can be suppressed by using gentler tapering. Fig. 3.22 shows the conversion efficiency at the output tapering section for the case that the silicon waveguide is capped by silica.

The upper limit efficiency is summarized in Table.3.5. It is determined by the feeding and collecting efficiencies. The mode conversion efficiency asymptotes to unity as the length of the taper region increases.

Table 3.4: Taper efficiency-parabolic taper length $150\mu m$. The pad is $2um$ by $2um$.

type	w_2(nm)	TE in	TE out	TE total	TM in	TM out	TM total
silica	130	90.6%	89.4%	81.0%	99.2%	98.8%	98.0%
SU-8	180	93.6%	93.5%	87.5%	99.6%	99.4%	99.0%
cytop	220	95.0%	93.1%	88.4%	99.7%	99.3%	99.0%
pad	50	95.5%	95.2%	91.0%	99.1%	91.9%	91.1%

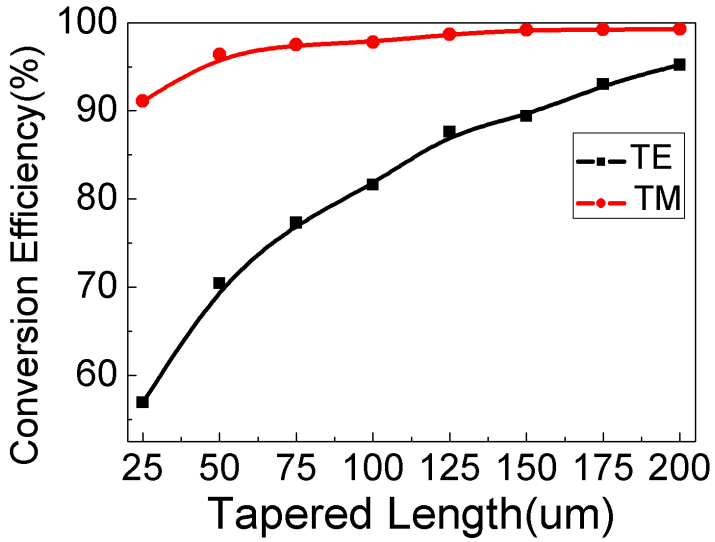

Figure 3.22.— The mode conversion efficiency at the output tapering section for silicon waveguide capped by silica case.

Table 3.5: The upper limit of the total (fiber to fiber) coupling efficiency. The upper limit is calculated for the TE case, and TM results are under the same geometric parameters as in the TE case.

type	input w_2	output w_2	limit(TE)	limit(TM)
silica	0.13	0.17	0.66	0.52
SU-8	0.18	0.19	0.43	0.37
cytop	0.22	0.22	0.39	0.34
pad($3\mu m \times 3\mu m$)	0.05	0.05	0.71	0.71

3.3.6 Characterization

To experimentally verify our designs, we fabricated a waveguide-coupled cavity in a SOI wafer with a 220 nm device layer on a 2 μm buried oxide. A negative electron-beam lithography resist, Foxx-17 (Dow Corning) diluted in Anisole in a 1:6 ratio, was used for e-beam lithography. The film was spun coated onto the sample at 5000 rpm and then baked at 90°C on a hot plate for 5 min, resulting in a total film thickness of 135 nm. Patterns were defined using a standard 100kV e-beam lithography tool (Elionix) and developed in tetramethyl ammonium hydroxide (25% TMAH) followed by a thorough de-ionized water rinse. The devices were etched in a reactive ion etcher (STS-ICP RIE) using SF_6, C_4F_8, and H_2 gases(73). The SEM images of the fabricated device are shown in Fig. 3.23.

Approach II in the previous section was used as the spot size converter (89) (SU-8 pad is 2 μm $\times$ 2 μm cross-section).

Since we are motivated by the bio-sensing applications of our cavities, we cover the cavities with a protective chemically-inert polymer. Unfortunately, PMMA ($n = 1.45$), assumed in the design phase, was found to be unsuitable and therefore the devices were covered with CYTOP, a more robust polymer with a refractive index $n_{\text{clad}} = 1.34$. We found that the smaller refractive index of the top cladding compared to the simulated one slightly affects the performance of our cavities: using 3D FDTD modeling we found that the cavity resonance is shifted to a smaller wavelength ($\lambda_{\text{model}} = 1517$nm), the cavity Q_{total} is 2.72×10^6, and the on-resonance transmission is $T = 75\%$.

We characterized the device by scanning a tunable laser source from 1470 to

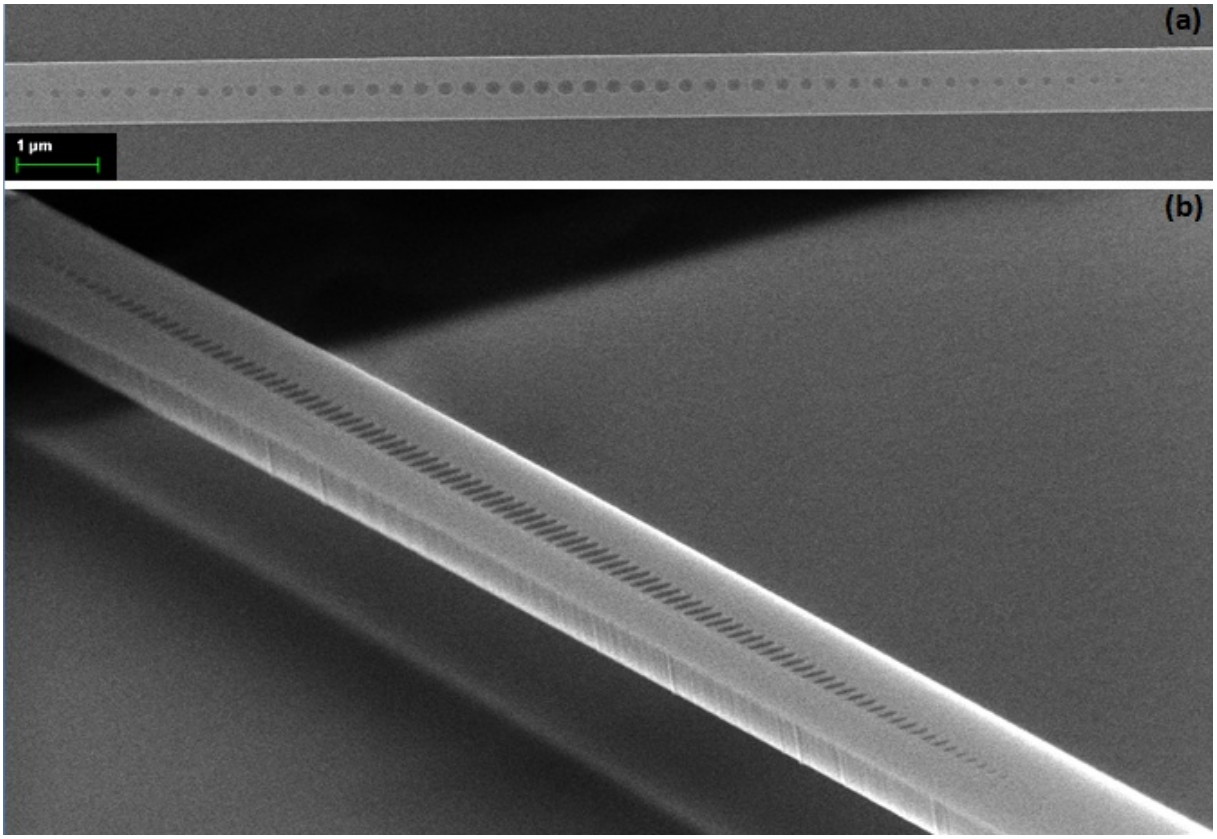

Figure 3.23.— (a) Top view SEM image of the nanobeam cavity. (b) Perspective view of the nanobeam cavity (holes are circular, appeared as elliptical due to the imaging direction).

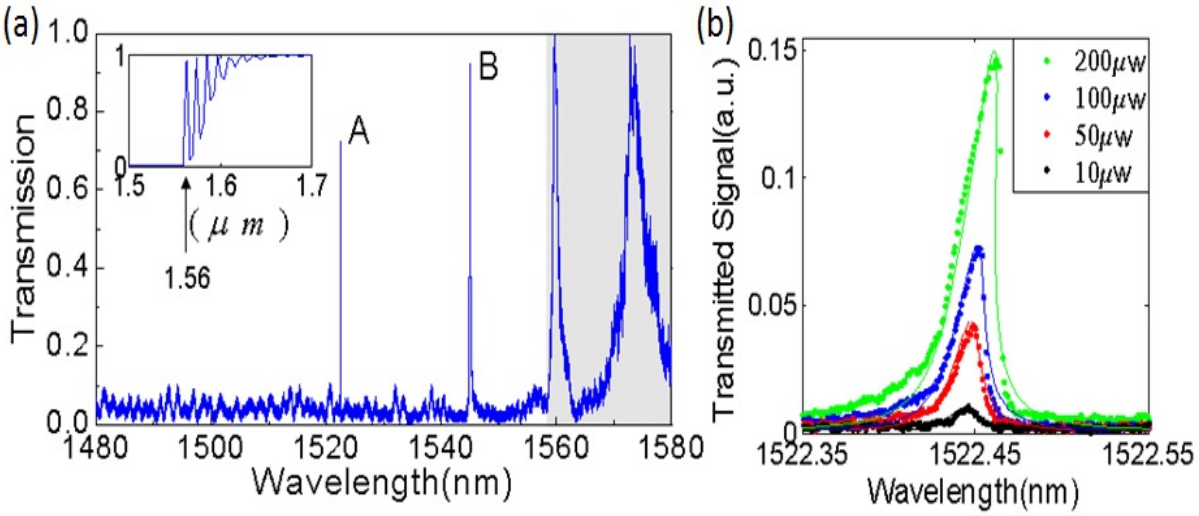

Figure 3.24.— (a) Experimental transmission spectrum when input power is $100\mu W$. The signal is normalized by the band-edge modes (shaded region), which have unity transmission, as verified by 3D-FDTD simulations shown in the inset. Due to the very large photon life time of our ultra-high Q cavity ($\tau_{\text{photon}} = Q/\omega \sim 1\text{ns}$), it becomes nearly impossible to model transmission through the cavity (resonant tunneling) using the 3D FDTD method directly. Hence, the high-Q cavity mode does not appear in the simulated spectrum. (b) Zoom-in of the transmitted signal of the fundamental mode (mode A) at different input power levels (measured at the fiber tip). The dots are experimental data and the lines are fitted curves using equation (3.8).

1580 nm. A tapered fiber (2.5-μm spot diameter) is used to couple light in and out of the polymer waveguide. A polarizer is placed at the output to filter out the TM-like mode. Fig. 3.24(a) shows the experimental transmission spectrum through one of the resonators. A nonlinear bistable lineshape is observed, as shown by the power-dependent spectra in Fig. 3.24(b). We fitted the experimental data using the following expression, typical of a nonlinear bistability

$$T = \frac{P_{out}}{P_{in}} = \frac{Q_{\text{total}}^2/Q_{\text{wg}}^2}{1 + (P_{out}/P_0 - 2(\lambda - \lambda_0)/\gamma_0)^2}, \tag{3.8}$$

where $P_0 = 3gQ_{\text{total}}Q_{\text{wg}}(\omega/(2nc))^2\chi^{(3)}$ is the measured power in the presence of a third-order nonlinearity, g is a nonlinear feedback parameter introduced by Soljacic et al., and γ_0 is the natural cavity linewidth (90). $g \sim 1/V_{\text{eff}}$ is a measure of the field confinement in the nonlinear region. From the fits, we obtained an experimental $Q = 80,000$ and an on-resonance transmission $T = 73\%$ for the on-substrate and polymer-capped cavity. This corresponds to a $Q_{\text{sc}} = 500,000$, which is comparable to our previously reported results for a free-standing photonic crystal nanobeam cavity(73). The demonstrated transmission is much higher than previous work on a cavity with a similar Q factor(91)(92).

3.4 Summary

In summary, we briefly discussed ring resonators and presented a detailed analysis and a deterministic design of the ultra-high Q photonic crystal nanobeam cavities and verified with experiments. With this method, $Q > 10^9$ radiation-limited cavity, and $Q > 10^7, T > 95\%$ waveguide-coupled cavity are deterministically designed. These Q-factors are comparable with those found in whispering gallery mode

(WGM) cavities(86)-(88) and have ultra-small mode volumes, typically two or three orders of magnitude smaller than WGM ones. Furthermore, energy maximum can be localized in either the dielectric region or air region with this method. Although we demonstrate designs for TE-like, transversely symmetric cavity modes, the design method is universal, and can be applied to realize nanobeam cavities that support TM-polarized modes, as well as line-defect 2D photonic crystal cavities. We believe that the proposed method will greatly simplify the processes of high Q nanobeam cavity design, and thus enable both fundamental studies in strong light and matter interactions, and practical applications in novel light sources, functional optical components (filters, delay lines, sensors) and densely integrated photonic circuits.

Chapter 4

Photonic Crystal Nanobeam Cavities for High-Sensitivity, Label-free Sensing

4.1 Introduction

4.1.1 Sensing Principle

Optical cavity sensing schemes are based on monitoring shifts of the resonances of high-Q cavities, due to analyte-induced refractive index changes in the near-field of the structure. These changes can be localized perturbations due to the adsorption of analyte onto the cavity surface (e.g. adsorption of proteins), or global perturbations in the background refractive index due to a change in the bulk concentration of the analyte (e.g. differences in glucose concentrations in an aqueous solution). As

illustrated in Fig. 4.1, resonance of the cavity is shifted as molecules come into the cavity mode, and the equilibrium of the shift indicates the concentration of the molecules in the solution. The shift of the resonance is typically proportional to $V_{\text{molecule}}/V_{\text{mode}}$, therefore, an optical cavity with small mode volume will enhance the sensitivity of the detection. Photonic crystal nanobeam cavities, with its wavelength-scale mode volume (typically 100-1000 times smaller than WGM cavities), can in principle offer much higher sensitivity. The other important factor is the Q-factor. It determines the resolution that the resonance shift can be differentiated. Higher Q results in narrow resonance line-width, and finer resolution.

4.1.2 Sensor Fabrication

We chose the photonic crystal nanobeam cavity geometry and employed the deterministic design method introduce in Chapter 3. The photonic crystal nanobeam cavity(74) consists of a tapered array of holes (periodicity 330nm), defined along a 600nm wide ridge waveguide. The cavity region was approximately $15\mu m$ long. The SEM image of the center part and its mode profile (obtained from FDTD simulation) are shown in Fig. 4.2.

The device was fabricated on a silicon-on-insulator (SOI) wafer with a 220 nm device layer on a 3μm buried oxide(73). The structure was defined by electron-beam lithography using Hydrogen SilsesQuioxane (HSQ) as the resist, followed by reactive ion etching (C_4F_8/SF_6) of silicon. The polymer pad method (Approach II in Chapter 3.3.5) was used to achieve efficient coupling between a commercial tapered optical fiber (Ozoptics inc.) and silicon waveguide. The fiber-waveguide coupler consists of

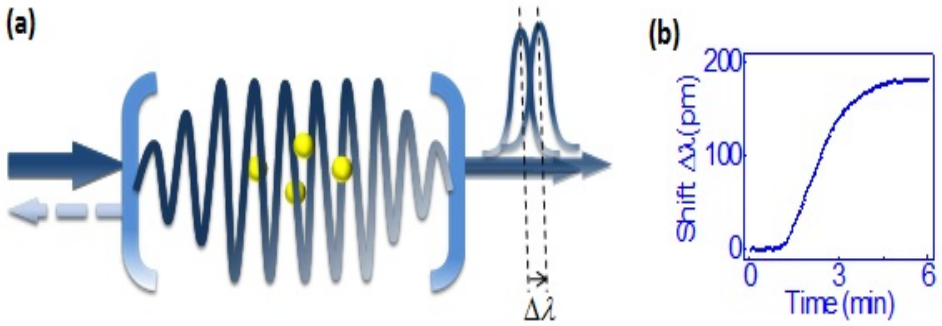

Figure 4.1.— (a) The resonance of the cavity is shifted as molecules come into the cavity mode, changing the optical path. (b) A resonance v.s time plot indicates the concentration of target molecules in the solution.

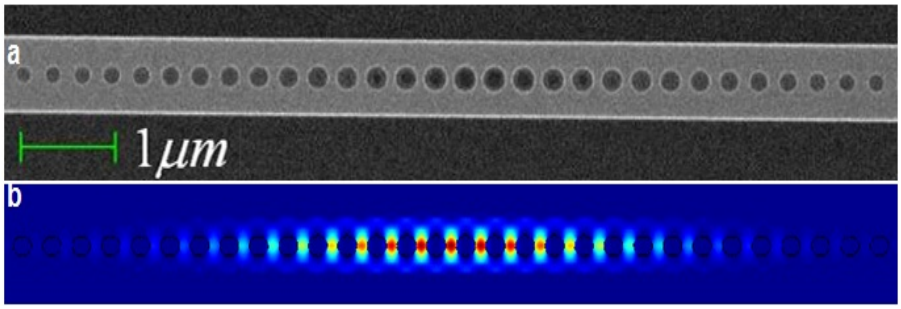

Figure 4.2.— (a) SEM image of a representative silicon nanobeam cavity (top view). (b) FDTD simulation of the energy density distribution in the cavity on resonance, showing an optical mode volume in sub micrometer-cubed scale.

a 3 μm $\times$ 3μm cross-section polymer (SU-8 resist) waveguide, defined through a second electron-beam lithography step. In the mode conversion section, the width of the silicon waveguide was linearly tapered from 600nm to 50nm over a length of 500μm, in order to adiabatically couple the light from the SU-8 waveguide to silicon waveguide(74).

4.1.3 Fluidic Channel

We used fluidic channel to deliver the sample to the chip. The fluidic channel was made of polydimethylsiloxane (PDMS, Sylgard 184, Dow Corning) with two millimeter-diameter holes on both ends as inlet and outlet. A piece of solid PDMS was cut into 4mm×1mm×1mm (length×width×height) blocks and was bound to silicon wafers after oxygen plasma treatment. These blocks served as a template for replica-molding. To prevent adhesion during replication, the template was exposed under vacuum to vapors of (1H,1H,2H,2H-perfluorooctyl)trichlorosilane (Gelest Inc.). A 10:1 mixture of PDMS resin and cross-linker (Sylgard 184) was poured over the template cured at 70°C for 2 hours. The cured PDMS channels were then pealed off the wafer and 2mm-diameter holes were punched at ends of the channel to define the inlet and outlet for tubing.

We sealed the PDMS channel over the chip containing the cavities using one of two different techniques, in order to realize either a permanent or temporary seal to the silicon chip. To realize the permanent seal, a thin layer liquid PDMS precursor (10:1 resin:cross-linker, Sylgard 184) was first evenly painted onto the underside of the channel walls and they were treated with oxgen-plasma. After Oxygen plasma

treatment of the silicon chip, the channel was stamped onto the chip and the PDMS glue layer was cured at 70°C for 3 hours. To realize the temporary seal, the PDMS channel was physically clamped on to the chip, using a home-made clamp (shown in Fig. 4.3(b)) fabricated with laser cutter. This allowed us to thoroughly clean the chip and re-use it multiple times. In order to allow the use of sonication in our cleaning procedure, we protected the polymer pads from detaching by depositing a film of the low-index polymer - CYTOP (Bellex Inc.) on top. To expose the nanobeam cavity region to analyte, the CYTOP layer was removed from the cavity region in oxygen plasma through a photolithographically defined mask.

4.1.4 Sensing Set-up

A photo of the sensing setup is shown in Fig. 4.4. Inset (a) shows the zoom in around the chip. Chip and fluidic channel is mechanically sealed with the home-made clamp. Inset (b) shows the schematic of the setup: the light from the tunable laser source was coupled into the nanobeam cavity with tapered optical fibers, and light is coupled out the same way to a detector. The optical polarizers were used to filter out the unwanted TM polarization component.

4.2 Sensing Experiment

4.2.1 Refractive Index Sensing

First, we calibrated the sensor using DI water, methanol, acetone, and IPA, whose refractive indices have been measured in the near-infrared(93). The fluid were delivered to the sensor with the fluidic channel, during which the resonances wavelength of the cavity were monitored. The shift of the resonance should be proportional to the refractive indices of different solutions.

The equilibrated wavelengths are shown in Fig. 4.6. The experimental data fit to a linear calibration curve and were in good agreement with FDTD simulation. According to the linear fit to the experimental data, the wavelength shift per refractive index unit (RIU) was 83nm/RIU.

To identify our detection limit, we sweep the laser (Santec 510) and extract the resonances as only pure water is flown into the cell. As indicated in Fig. 4.14, the fluctuation is on the order of 1pm, therefore our sensor can detect a minimum refractive index change of 1.2×10^{-5}RIU. This detection limit is due to the laser wavelength fluctuation, as shown in Fig. 4.5(a), where a high resolution wavemeter is used to track the laser output wavelength.

4.2.2 Glucose Sensing

Next, we exploited the sensor to demonstrate quantitative detection of small glucose concentrations in solution by monitoring small changes in refractive index.

Resonance shifts were calculated using the resonance of the cavity when immersed in DI water as the baseline.

The resonance shifts at different glucose concentrations are shown in Fig. 4.7, and were fit to a linear curve. Inset figure shows the real-time response of the sensor at the smallest detectable concentration. Based on the calibration in Fig. 4.6, we estimated the refractive index change of $1.2\text{cm}^3/g$ of sugar concentration, which is in good agreement with data measured at visible wavelengths(96). A detection limit of 10mg/dL was achieved, capable of discriminating the abnormal sugar blood level in human body. Zirk et al.(97) showed that electrical conductivity measurements (which depends on osmolality) can be combined with refractive-index sensing to generate accurate measurements of blood glucose levels in vivo. By integrating our silicon-based optical sensor side-by-side with microelectronic circuit (in the same silicon device layer) a compact, inexpensive, integrated, sensing platform for blood-glucose monitoring could be achieved.

4.2.3 Single Nanoparticle Detection

In the above two cases, the nanobeam cavity was used to detect a global index change of the solution. The wavelength shift, in this case, scales as $\Gamma_{\text{water}} = \int_{\text{water}} \epsilon|E|^2 d\text{V} / \int_{\text{all}} \epsilon|E|^2 d\text{V}$, i. e. the amount of the field that is confined in the solution. As a result, the mode volume of photonic crystal does not manifest after the integration.

In this section, we will use the nanobeam sensor to detect individual nanoparticles, the wavelength shift of which, in this case, scales as $V_{\text{molecule}}/V_{\text{mode}}$.

To improve the detection limit, we used a more stable laser (Agilent Inc.). We also found that it is crucial to mechanically stabilize the laser, by putting acoustic foams beneath and around the laser. As is shown in Fig. 4.5(b), a wavelength stability of 0.1pm is achieved.

Polystyrene particles with diameters 25nm, 50nm and 200nm are injected to the sensor. The cavity resonance are measured every 0.1 second for 1 minute. As shown in Fig. 4.8, the discrete resonance jumps indicate the detection of single nanoparticles, as individual particles come to the cavity mode volume. The overall trend of the curve is due to a combination effect of temperature drift, laser wavelength drift, as well as gradual change of the refractive index of silicon as solutions are injected into the sensor, which was also observed in (94). The inset shows the resonance steps for the particle size d=25nm and 50nm.

From perturbation theory introduced in Chapter 3, we have

$$\Delta\lambda \propto r^3 e^{-r/L} \tag{4.1}$$

r is the radius of the particle (d=2r), L is the characteristic length of the cavity field, that can be obtained from FDTD simulation. If we take log of the above equation, then

$$\texttt{log}(\Delta\lambda) + r/L = 3\texttt{log}(r) + \texttt{Constant} \tag{4.2}$$

By fitting the evanescent field to an exponentially decaying profile, we obtained $L = 51nm$ (Fig. 4.9). Fig. 4.10 shows the $\texttt{log}(\Delta\lambda) + r/L$ v.s $\texttt{log}(r)$ plot. A linear fit gives a slope of 2.98 ± 0.17, which agrees well with the above equation. Therefore, we believe we have demonstrated detection of 25nm-size single polystyrene nanoparticle, which is the smallest available polystyrene nanoparticle.

4.2.4 Single Protein Detection

To demonstrate detection of single protein molecule, we injected 2pM of streptavidin carried in PBS solution into the sensor. Prior to that, the chip was cleaned by oxygen plasma and immersed in 2% 3-aminopropyltrimethoxysilane in ethanol for 10 minutes, rinsed thoroughly and heated at 80°C for 2 hours.

The resonance shift is shown in Fig. 4.11. A visible step ∼0.1pm is observed. Fig. 4.11 also plots the resonance shift for 5pM streptavidin. Since nanobeam cavity has small mode volume, after a few clear steps, binding of the streptavidins on the sensor decreases its sensitivity to new streptavidin molecules, and smears out the binding steps.

4.3 Improve the Sensitivity Using Nonlinear Bistability

The Q-factor of the cavity is a key parameter that determines the lowest detection limit of conventional cavity-based sensors. Therefore, most cavity based sensors operate in visible wavelength range, where absorption of water, the common carrier fluid, is negligible. However, technologically it would be much more relevant and applicable if one could use sensors that operate in telecom wavelength range, where there is an abundance of inexpensive, robust, reliable, and widely tunable laser sources. Furthermore, such sensing platform could be realized in silicon, using CMOS compatible fabrication techniques, enabling integration with micro-electronics control circuitry. Unfortunately, since water absorbs heavily in telecom range, this is

simply not possible and sensitivity is limited by water absorption. As shown in Fig. 4.12, the Q-factor is decreased when the sensor is surrounded by water, compared to that by air, as water has higher refractive index. Furthermore, since water absorbs at telecom and heavy water does not, the Q-factor in water is more than half smaller than in heavy water. Several sensitivity enhancement schemes have been proposed, including those based on active nanocavities (lasers) with gain(99)(100) and asymmetric Fano-like resonances(101)(102).

To overcome this, the bistable cavity sensing (BCS) scheme that we propose and demonstrate here takes advantage of optical bistability due to strong thermo-optic effect in our silicon-based high-Q cavities, as we have shown in Chapter 3. Qualitatively, as the wavelength of the laser source approaches the cavity resonance, optical energy builds up inside the cavity. A portion of the energy is converted into heat, inducing a change in the refractive index of silicon(103)-(105). This power dependent refractive index produces a bistable region(106) in the cavity transmission spectrum (shown as dashed line in Fig. 4.13(a)). As a result, sweeping the wavelength of the input laser in an increasing manner across the cavity resonance causes the cavity to operate at one stable state, right up until the laser wavelength reaches the bifurcation point at the long-wavelength end of the bistable region (shown as solid line in Fig. 4.13(a)). At this wavelength, energy is released from the cavity and the cavity transmission drops discontinuously to the low-transmission state. Our sensor operates by monitoring analyte-induced shifts in the wavelength at which this output signal discontinuity occurs. Importantly, the wavelength uncertainty of this drop has a sharpness limited only by the wavelength resolution and noise of the laser, and is *independent of the cavity Q-factor*. In addition, the

transmission drop can be orders of magnitude larger than the noise level of the system (detector in particular), resulting in high signal-to-noise ratio (SNR) in our system. The temporal response of the thermo-optical effect is on the order of 0.5μs(105), which is slow for optical signal processing, and is therefore typically overlooked for applications in telecommunications. This time constant is, however, suitable for biosensing applications since many biological processes occur at longer time scales(108). Other nonlinear mechanisms (e.g. χ^3 in silicon, χ^2 in III-V materials, opto-mechanical Kerr-like nonlinearity, etc), and a broad range of cavity structures(103)-(105) could also be used in a BCS scheme, particularly if an increase in operation speed is necessary.

We compared the sensitivity of the nanobeam sensor operating in the linear regime and in the BCS regime, by adjusting the power of the laser (using external optical attenuator) to be below and above the characteristic power necessary for bistability, respectively. We stabilized the laser output power using a feedback loop. We also adjusted the output power of the cavity using optical attenuators. These were done to maintain a constant SNR at the detector in both sensing schemes, allowing a direct comparison between the two techniques. A comparison of the noise level of the two techniques is shown in Fig. 4.14. In the linear regime, the resonance was extracted by tracking the wavelength associated with the maximum transmitted power, the fluctuation is found to be 3pm. It is limited by the cavity linewidth(γ) and the noise in the photonic circuit, that can be estimated with: $\sigma_{\text{Loz}} = \gamma/(4.5\ \text{SNR}^{0.25})$ (107). In the BCS regime, the nonlinear resonance was extracted by tracking the wavelength that corresponds to the half of the maximum transmitted power. The nonlinear method showed significantly better resolution

(≈1pm), limited by the stability of our laser (Santec 510, Fig. 4.5(a)). This indicates that BCS detection limit is not bound by cavity linewidth, as predicted. Fig. 4.14 also shows the signal averaging method based on the fitting of the cavity resonance with the Lorentzian lineshape. The noise level is on par with the BCS, indicating that BCS method is inherently immune to detector noise.

Next, we used the BCS method to detect the adsorption of a small number of protein molecules onto the cavity, the surface of which was functionalized with amine-terminated silanes. In addition to optical bistability, this measurement takes advantage of the nanobeam cavity's small mode volume to enhance its sensitivity. We measured the nonlinear resonance shift after the injection of Bovine Serum Albumin (BSA) solutions at different concentrations. Each point in Fig. 4.15(a) represents the resonance shift for a given BSA solution after the adsorption process has reached equilibrium. Discernable shifts above the noise-level were observed starting from 0.1aM concentration BSA in water (The real-time response is shown in Fig. 4.16). The low limit of detection of our device can be explained in part by the long range electrostatic interactions between positively charged surface and BSA, which carries a significant negative charge at neutral pH. Increasing the ionic strength with 150mM NaCl decreased the sensitivity to 1fM. This indicates that electrostatic interactions between the sensor surface and the BSAs were helpful in transporting the BSAs on to the surface(110). The same experiment was also performed with the well-know surface plasmon resonance based instrument (Biacore™ 3000). Fig. 4.15(a) showed multiple orders of sensitivity improvement of the nanobeam sensor over Biacore in solutions with both high ionic strength and low ionic strength.

To confirm the absorption of BSA on the nanocavity, 1aM BSA labeled with

Alexa fluor 555 (invitrogen) was detected on the nanobeam sensor (Fig. 4.15(b)), and the sensor chip was subsequently imaged by fluoresence microscopy (Fig. 4.15(c)). By calibrating the image with measurements of single BSA molecules adsorbed to silicon chip, we estimated that about 185 BSA molecules were adsorbed to the sensor surface. This is in good agreement with the calculated BCS shift using perturbation theory. Fluorescent images from these experiments were difficult to acquire possibly because BSAs dissociated from the sensor surface before imaging. Improving the stability of the laser source from 1pm to <10fm(108) using standard laser stabilization techniques(109) should further improve the sensitivity of our system by more than two orders of magnitude.

4.4 Digital Biosensing

In this section, we theoretically analyze a sensing scheme: named as digital sensing, based on the optical bistability, that does not require sweeping the laser wavelength. Fig.4.17 shows the output v.s input power at different detunings normalized by the natural linewidth of the cavity when no nonlinearity is present in the system. The threshold for the system to exhibit bistable state is $\delta > \sqrt{3}$.

Digital sensing mechanism can be illustrated in following way: (i) the system is initialized in state A on the blue curve. (ii) The arrival of analyte results in a red-shift of the cavity resonance (since the analyte has higher index than carrying fluid, e.g. water), resulting in smaller detuning, so that now more power is coupled to the cavity and normalized input P/P_0 increases. The consequence of this is that the system jumps from blue curve (point A) to red curve (point B). (iii) This results

in the stark change of the power transmitted through the cavity which can be easily detected. Interestingly, even after the analyte leaves the cavity region, the system remains in the state B (high transmission state). That is, due to optical bistability, the systems has a built in memory and remembers if analyte was present or not. Therefore, we coin this detection scheme as digital sensing. After the read-out phase is over, the system can be brought back to initial state A, and prepared for next detection event, simply by turning the laser off for short period of time (assuming that additional binding sites are available for a subsequent detection event). The initial state can be placed in the shaded region. Initializing at higher input power (close to the bistable region) will make the system more sensitive to perturbations. However, initializing at lower input power is more immune to the noise.

For those analyte which has a lower index than its environment, the initial state must be placed on the higher transmission state. And the signal would be a sudden drop instead of a jump. To compare the sensitivity of this digital sensing and normal spectral based sensing, the green curve shows the perturbation the analyte must produce, i.e. the resonance shifts by one linewidth, which is evidently a much greater perturbation. The fulfillment of digital sensing requires a stable laser source. The system is naturally immune to noise on the detector side. The power stability and wavelength stability of the laser source will be the limit of the detection.

4.5 Decrease the Cost Using Polymer Cavity Sensor

Micron to nanometer scale devices based on polymeric materials have gained more and more attention due to its high flexibility, and potential of low cost. Examples of successful applications can be found in broadband communications(111), large screen and flexible displays(112), solar cells(113)(114), biomedical detection(115)(116) and etc. However, it has been a challenge to achieve high Q photonic crystal (PhC) cavities made of polymeric materials due to the low index contrast between available materials. While there has been some recent demonstrations of 2D (119) and 1D (121) photonic crystal cavities in relatively low-index-contrast platforms ($n_{\mathrm{cav}}/n_{\mathrm{bg}} \sim 1.5$) achieving simultaneously high quality factors and small modal volumes in this regime has remained elusive.

In this section, we demonstrate all-polymer photonic crystal nanobeam cavities, fabricated in the electron-beam resist ZEP520 ($n = 1.54$) on a substrate of the spin-on fluoropolymer, CYTOP ($n = 1.34$). Despite having an extraordinarily small index-contrast ($n_{\mathrm{cav}}/n_{\mathrm{bg}} = 1.15$) we achieved Qs as high as Q=36,000 - an order of magnitude higher than the state of the art for $n_{\mathrm{cav}}/n_{\mathrm{bg}} = 1.5$ (121). The ability to achieve high Q with this index contrast allows us to fabricate cavities which are on-substrate (i.e. not suspended). Furthermore, polymeric nanobeam cavities have much smaller mode volume compared to the polymeric ring resonator with the same Q factor and made of the same material. Due to the high Q-factors and small volumes we observe, for the first time, optical bistability in the polymeric cavities at hundred microwatt power levels. Furthermore, because of the extended evanescent

field as a result of the low index of polymer, we demonstrated that polymer cavities, as biomedical sensors, have higher sensitivity over the widely demonstrated silicon based sensors(117). The simplified fabrication process of polymeric cavities potentially eliminates the need of clean-room facilities and can be scaled up for mass production(118).

The nanobeam cavity geometry consists of a ridge waveguide perforated with gratings of elliptical holes. The cavity was designed using the deterministic high-Q design method that we previously introduced. The distances between neighboring holes are kept the same as 550nm. There are in total 100 grating sections on both sides. The first 50 grating sections are 50 ellipses whose dimensions linearly decrease from the center to both ends of the $3.2\mu m$-wide and 550nm-thick waveguide, followed by 50 ellipses that have the same dimensions. In the linearly decreasing section, the major axes of the ellipses decrease from 1.44μm to 1.22μm, and the minor axes decrease from 165nm to 140nm. The reason for choosing elliptical shape instead of circular shape is because elliptical grating sections have larger bandgap and higher reflectivity to confine the optical mode. In our design, we considered a cavity having refractive-index $n_{\mathrm{cav}} = 1.54$ (e.g. ZEP520) surrounded by a background index $n_{\mathrm{bg}} = 1.34$. At this level of index contrast, a symmetric structure is essential to minimize coupling into substrate modes. A symmetric structure can be fabricated simply by adding a capping layer of CYTOP on top of the on-substrate cavity, however we note that the refractive index of the CYTOP layer also well matches the refractive index of many common liquids (e.g. water). Thus an equivalent optical structure is formed by immersing the cavity in water instead of adding a polymer capping layer. We used this geometry in our measurements as such a geometry

is ideal for optofluidic and sensing applications. We determined the theoretical mode profile and Q of the cavity mode using FDTD method. The mode profile is shown in Fig. 4.18(a), with a simulation Q=86,000. The device was fabricated directly via electron-beam lithography in the positive-tone resist ZEP520 (Zeon Corp.) resist ($n = 1.54$) supported by a 3.2μm layer of the low-index fluoropolymer CYTOP (AGC inc.) ($n = 1.34$) on a silicon chip. The CYTOP layer was deposited by multiple spin-coating steps. The polymer layers were sufficiently thin that no charging effects were observed using a 100kV electron-beam (Elionix Inc.), even in the absence of an added conductive layer. Fig. 4.18(b) shows the scanning electron micrograph (SEM) of the center region of a nanobeam cavity.

A schematic of the measurement setup is shown in Fig. 4.18(c). A tunable telecom laser source was coupled to the edge of the chip through a tapered fiber (TF, Ozoptics inc.) after a fiber polarization controller (FPC). Light was then collected from tapered fiber followed by a second FPC and an inline polarizer (Pol) to the detector. The two FPCs filter out the unwanted TM polarization component that is not in resonance with the cavity. We measured the cavities submerged in D_2O, which has negligible absorption in the telecom frequency range. Fig. 4.19 (a) shows the full spectrum of one of the cavities. The highest Q we obtained was 36,000 in D_2O, as shown in Fig. 4.19(b). Not only is the index ratio of our system much lower (index ratio=1.15), the Q-factor is almost an order of magnitude higher than previously demonstrated low index silica PhC cavities suspended in air (Q=5,000, index ratio=1.46)(121).

Small mode volumes are a significant advantage of PhC nanobeam cavities over the whispering gallery mode (WGM) cavities (e.g ring resonators, microspheres etc.)

since the strength of light and matter interaction scales inversely with V. A general trade off holds that higher Q-factors require larger mode volumes(76). Maintaining high Qs in low-index contrast cavities will increase the size of the ring resonators and PhC cavities. However, we found that the mode volumes required to achieve a given Q are much larger for ring resonators than for our nanobeam PhC cavities. We illustrated this by comparing the mode volumes of nanobeam cavities with ring resonators that have the same waveguide dimensions, and made of the same materials (ZEP on CYTOP immersed in D_2O). Fig. 4.19 (c) shows the relationship between Qs and mode volumes for the ring resonators with varying radii and for the nanobeam cavities with different number of tapered hole pairs (i.e. varying lengths). Notably, the ring resonators required to achieve the *measured* Qs of our nanobeam cavities have about 50 times larger mode volume, even *theoretically*.

Due to both high Qs and the small Vs, we were able to observe optical bistability(106) in our nanobeam cavity. Though optical bistability due to the thermo-optic effect (i.e. change of refractive index due to heat) has been widely observed in silicon cavities(74)(103)(104)(105), this is the first report of bistability in all-polymeric cavities. In contrast to the silicon case, polymer has a negative thermo-optic coefficient (dn/dT) (111) causing the resonance of the cavity to blue-shift with increasing power (Fig. 4.19(d)). Quantitatively, the heat that is converted from optical energy due to the absorption of polymer can be obtained from: $h = 2\sqrt{T}P_{\mathrm{in}}Q_{\mathrm{total}}/Q_{\mathrm{abs}}$. Thermal equilibrium is reached through conduction and convection processes. The thermal resistance of the cavity relates the heat generated in the cavity to the temperature rise at the center of the cavity by $\delta \mathrm{T} = h \cdot R_{\mathrm{th}}$. Therefore the resonance shift due to the thermo-optic effect can be

expressed as:

$$\delta\lambda = 2\sqrt{T}Q_{\text{total}}/Q_{\text{abs}}\frac{\mathrm{d}\lambda}{\mathrm{d}n}\frac{\mathrm{d}n}{\mathrm{dT}}R_{\text{th}}P_{\text{in}} \tag{4.3}$$

The thermo-optic coefficient for ZEP 520 is expected to be $\frac{\mathrm{d}n}{\mathrm{dT}} \sim -10^{-4}$.(111) Using the thermal conductivity $\sigma_{\text{th}} = 0.16\text{Wm}^{-1}\text{K}^{-1}$(122) and heat capacity $C_p \sim 1.5Jg^{-1}\text{K}^{-1}$, the thermal resistance of the cavity structure was estimated to be $R_{\text{th}} = 4.8 \times 10^4\text{KW}^{-1}$ from FEM simulation(105). Neglecting all the other heating effects, as well as higher order nonlinear effects that could change the index of the polymer, our experimentally observed resonance shift of 20pm at 170μW input power indicates $Q_{\text{abs}} \sim 10^6$ for linear absorption in the ZEP 520 layer, in agreement with the literature (123)(124).

Due to the low index contrast, the evanescent field of the polymeric cavity is more extended into the surrounding medium than the widely used silicon based nanophotonic sensors. As a result, the resonance shift of a polymeric cavity in response to the bulk refractive index change in the surrounding media is larger. Furthermore, our cavity design is optimized for optofluidic integration, with index-matching between the substrate and the fluid layer. To illustrate the potential for such an all-polymer platform for label-free sensing(117), we measured the shift in the cavity resonance in response to varying glucose concentration in water. The glucose solution was delivered to the cavity via a fluidic channel that was integrated on top of the chip. The channel was made of polydimethylsiloxane (PDMS, Sylgard 184, Dow Corning) with two millimeter-diameter holes on both ends as inlet and outlet. The channel walls were painted with a CYTOP layer to maintain index-matching in the waveguide. Fluid injection was kept at a constant rate of 50μL/min. The time response to the lowest reproducibly detectable concentration

(10mg/dL) is shown in 4.20 (a), along with the null response to pure DI water and the response to 20mg/dL glucose solution. The resonance shifts of glucose solutions at different concentrations are shown in 4.20 (b). Between each measurement, pure DI water was injected to the cavity and the cavity resonance shifted back to its original value. The response of the sensor to the concentration of the glucose solution exhibits excellent linearity covering the whole range of clinically relevant levels (4.20 (b)). We calculated that the wavelength shift per refractive index unit (RIU) to be $S = 386$nm. This is about 4 times larger than similar PhC structures made of silicon, and is about about 2 times larger than for ring resonators(107). The figure of merit (FOM $= SQ/\lambda = 9190$) is orders of magnitude larger than surface plasmon resonance based sensors (typically 8-23 (125)) and metamaterial sensors (330 (126)). Given the <1pm fluctuation in resolving the cavity resonance (4.20 (a)), our sensor can detect a minimum refractive index change of 2×10^{-6}RIU. 4.20 (b) further shows a direct comparison of our nanobeam sensor with the most well-known industrial label-free biosensors by repeating the same measurement on Biacore^{TM} 3000. Notably, nanobeam sensors demonstrated about 5 times improvement in the detection limit.

In summary, we achieved high-Q cavities in low-index-contrast polymeric materials. We observed bistability that originated from thermo-optic effect of the polymer, exhibiting a negative thermo-optic coefficient. We demonstrated high sensitivity and linearity of the polymeric nanobeam sensor in response to different glucose concentrations in water. The ability to realize high-Q/V nanophotonic resonators in a non-suspended all-polymer platform makes these devices potentially accessible to a broad range of materials as well as simple and scalable fabrication

techniques such as interference lithography, imprint lithography, and replica molding.

4.6 Summary

In this chapter, we demonstrated that the photonic crystal cavity is an ideal platform for bio-medical sensing. We demonstrated sensing of solutions with different refractive index, sensing of glucose concentration, detecting of single nano-particles and single streptavidin molecule. We also proposed to use the nonlinear bistable effect to improve the detection limit. We successfully demonstrated feasibility of fabricating high-Q cavities with polymeric material, which opens up new route to decrease the sensor cost, as well as to make new functional sensors with versatile polymers.

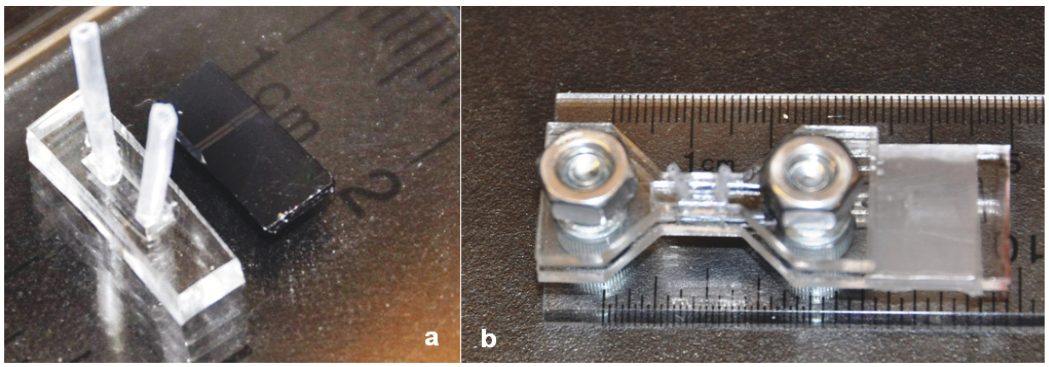

Figure 4.3.— (a) Photograph of the silicon chip (right) and the PDMS channel (left) before binding. (b) Photograph of the silicon chip and the PDMS channel clamped using the home-made acrylic support.

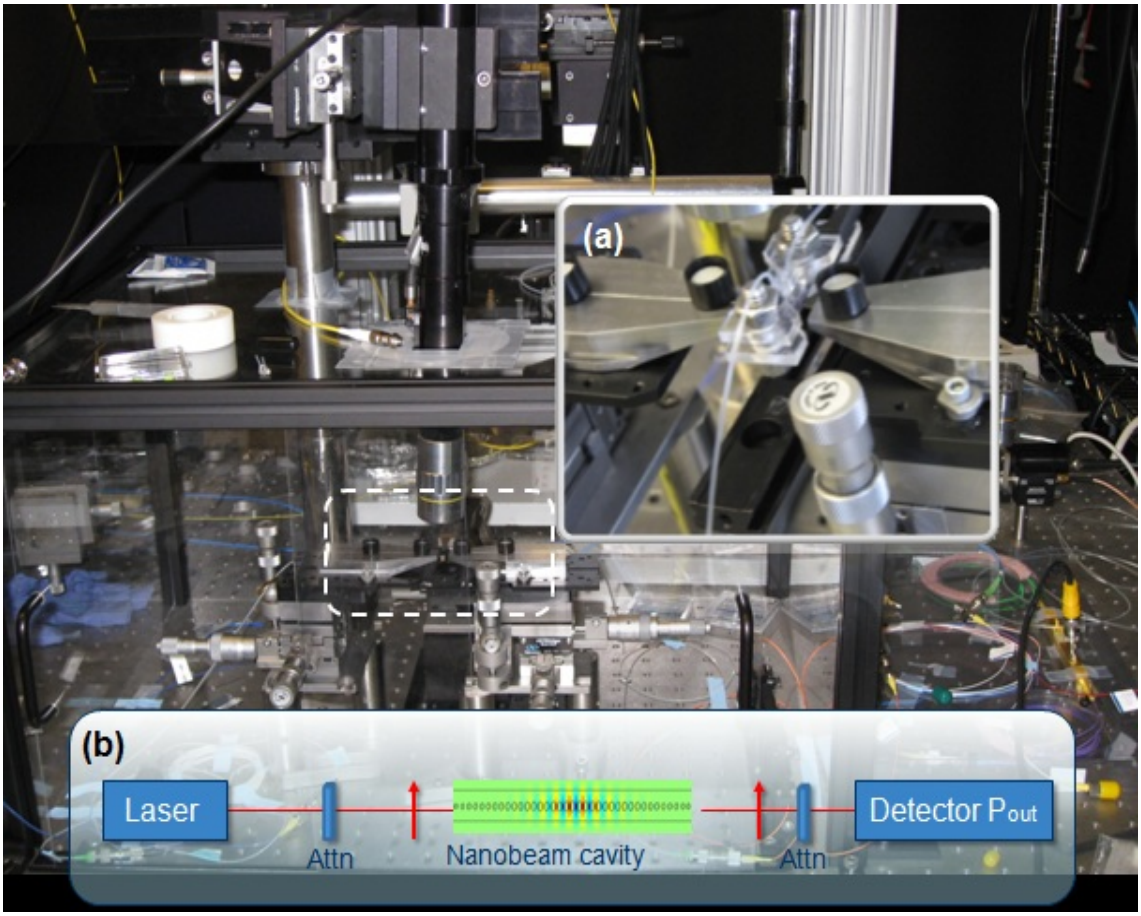

Figure 4.4.— Photograph of the setup. Inset (a) shows the zoom-in photo of the fiber coupling configuration. Inset (b) illustrates the schematic of the experimental setup. Attn denotes optical attenuator, the two arrows before and after the nanobeam cavity are optical polarizers, used to filter out unwanted TM polarization component.

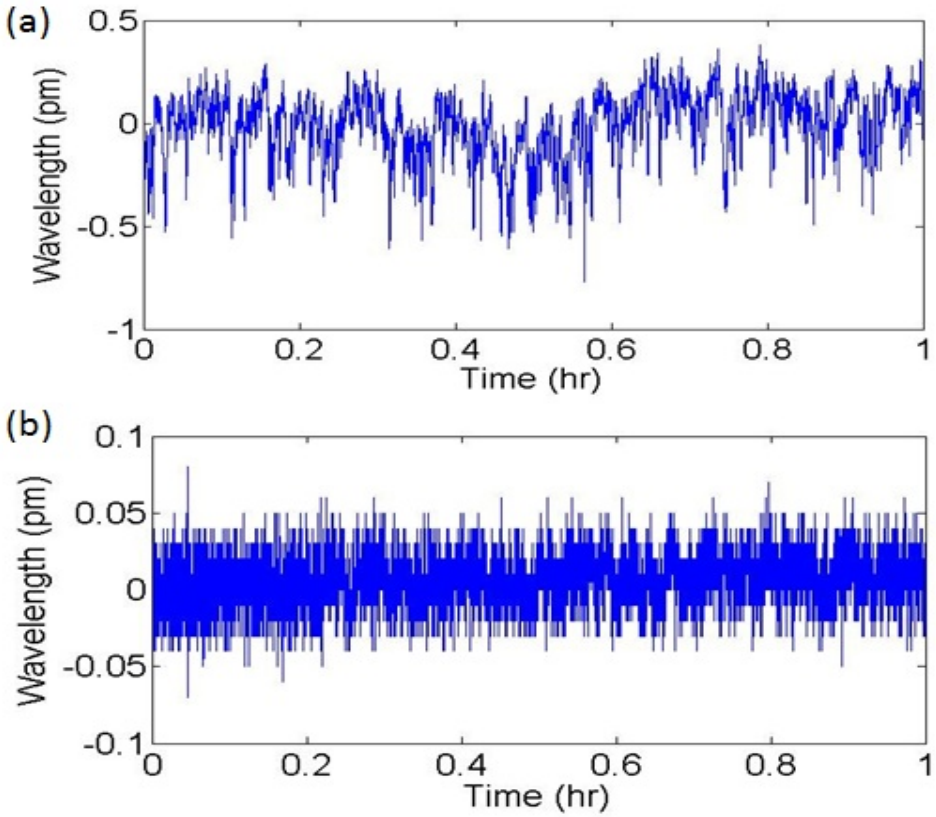

Figure 4.5.— (a) The wavelength fluctuation of Santec laser monitored by a high resolution wavemeter. (b) The wavelength fluctuation of the Agilent laser monitored by a high resolution wavemeter after mechanical isolation.

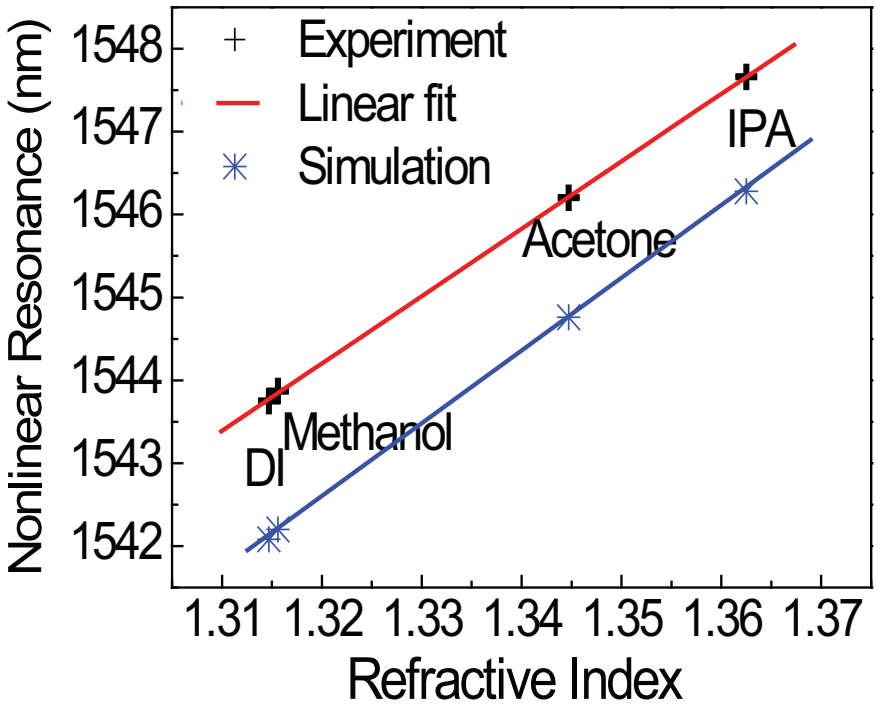

Figure 4.6.— Cavity resonances when the microfluidic channel is filled with DI water, methanol, acetone and isopropanol (IPA). The indices of these solutions were measured in telecom wavelength in (93). The red line is the linear fit to the experimental data. Blue dots are obtained from the FDTD simulations.

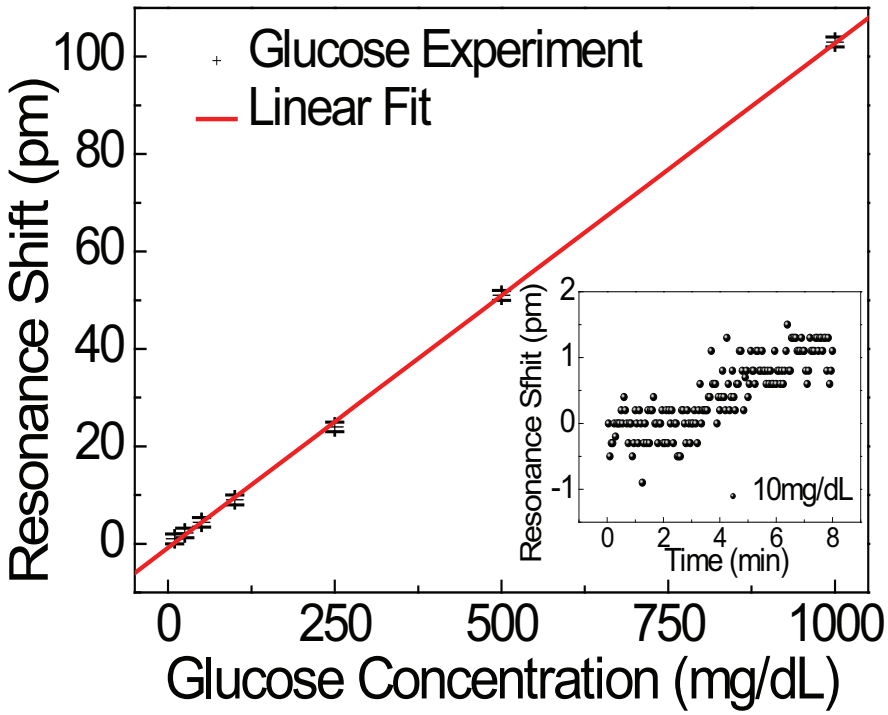

Figure 4.7.— Equilibrated resonance shifts in different concentrations of glucose solutions in water, showing discernable shift at concentrations. Inset shows real-time monitoring of the cavity resonances in response to the introduction of a 10mg/dL glucose solution in the fluidic channel. Measurement was taken under continuous fluid flow at 0.2mL/min.

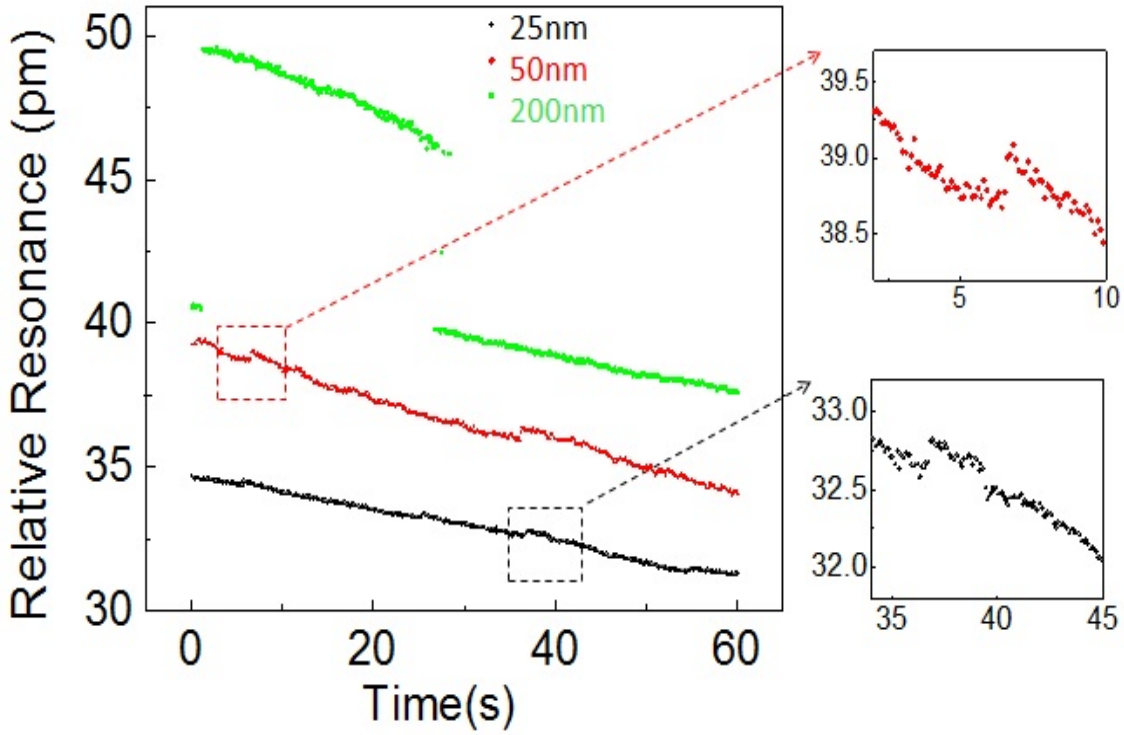

Figure 4.8.— The discrete resonance jumps indicate the detection of single nanoparticles. Polystyrene particles of 25nm, 50nm, 200nm were delivered to the sensor through the fluidic channel.

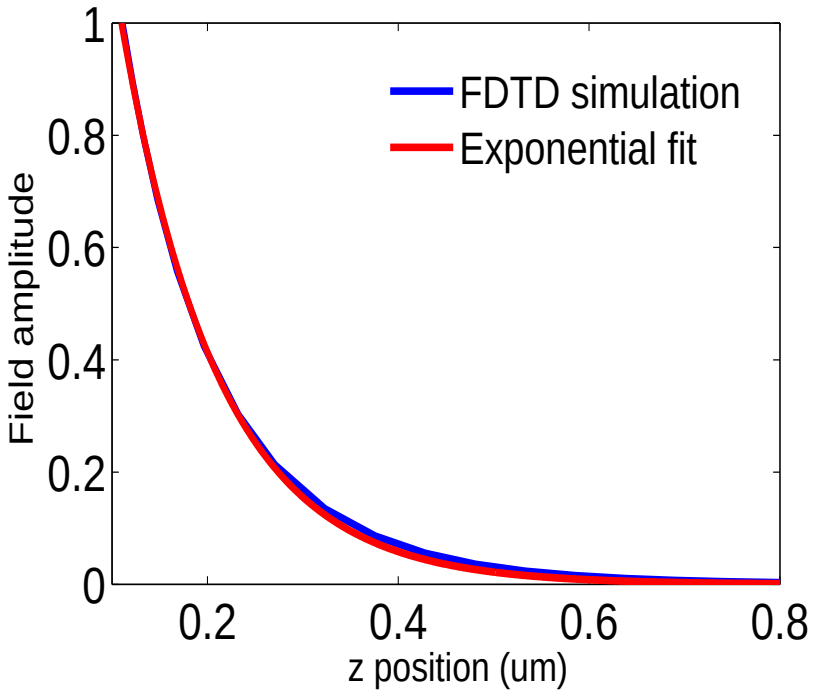

Figure 4.9.— The evanescent field profile away from the surface of the cavity.

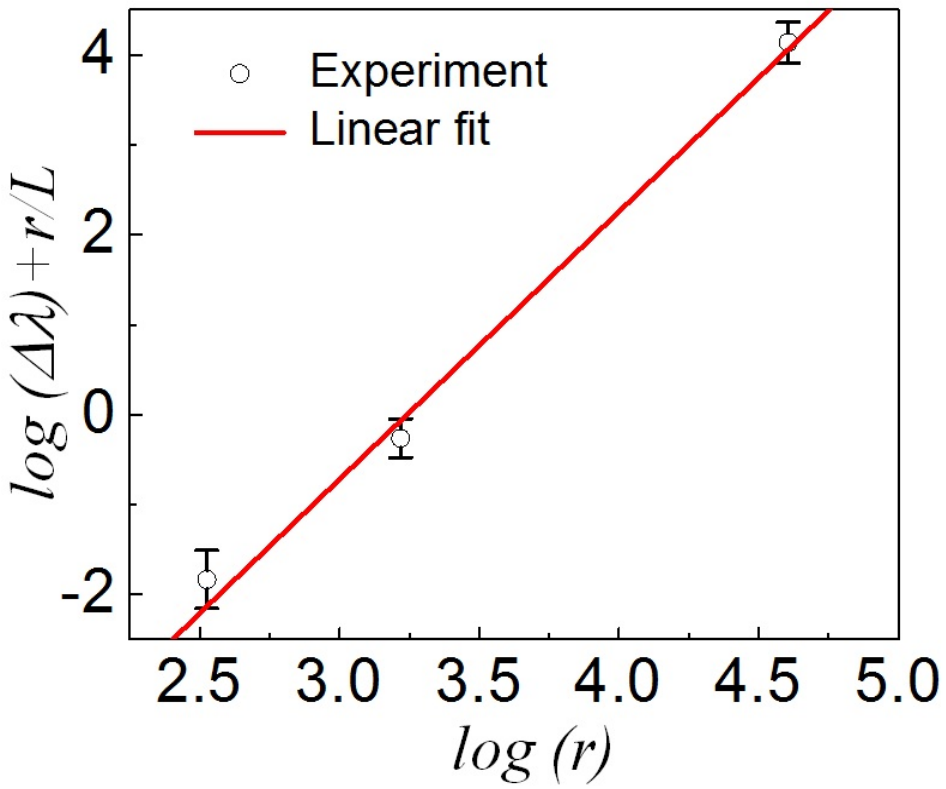

Figure 4.10.— The discrete resonance jumps indicate the detection of single nanoparticles. Polystyrene particles of diameters 25nm, 50nm, 200nm were delivered to the sensor through the fluidic channel.

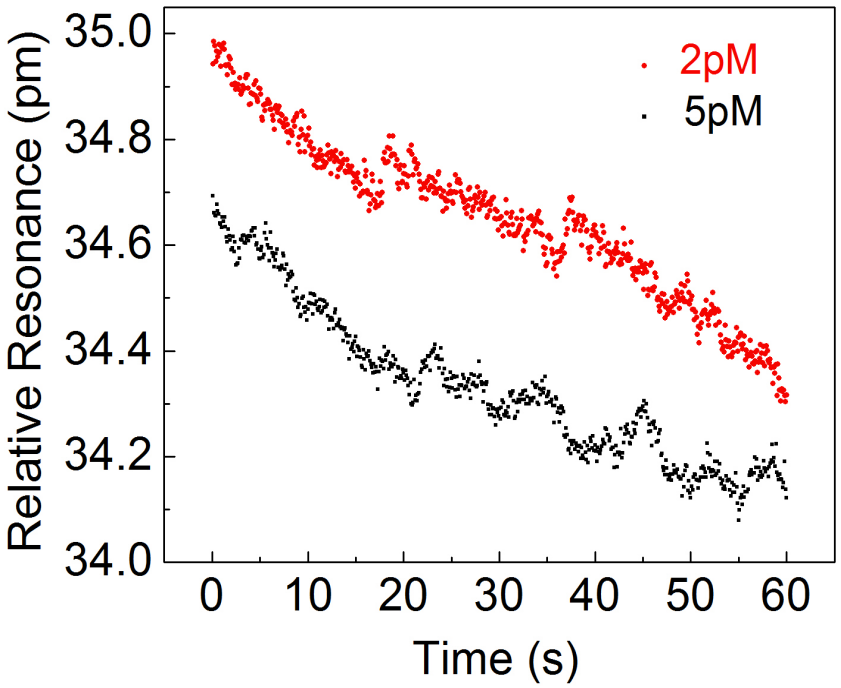

Figure 4.11.— Detection of single streptavidins at 2pM and 5pM in PBS solution.

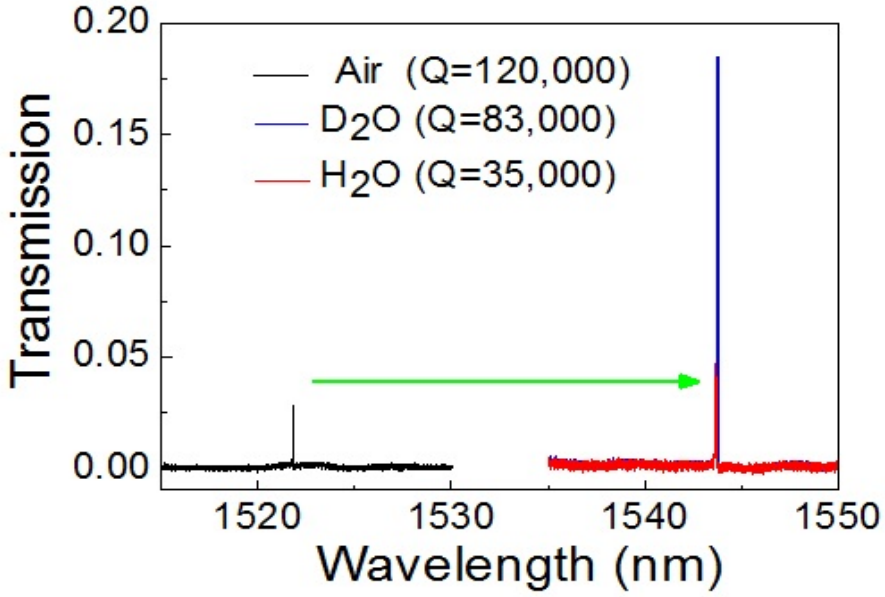

Figure 4.12.— (a) Resonances and Q-factors when the nanobeam cavity is immersed in air, water and heavy water.

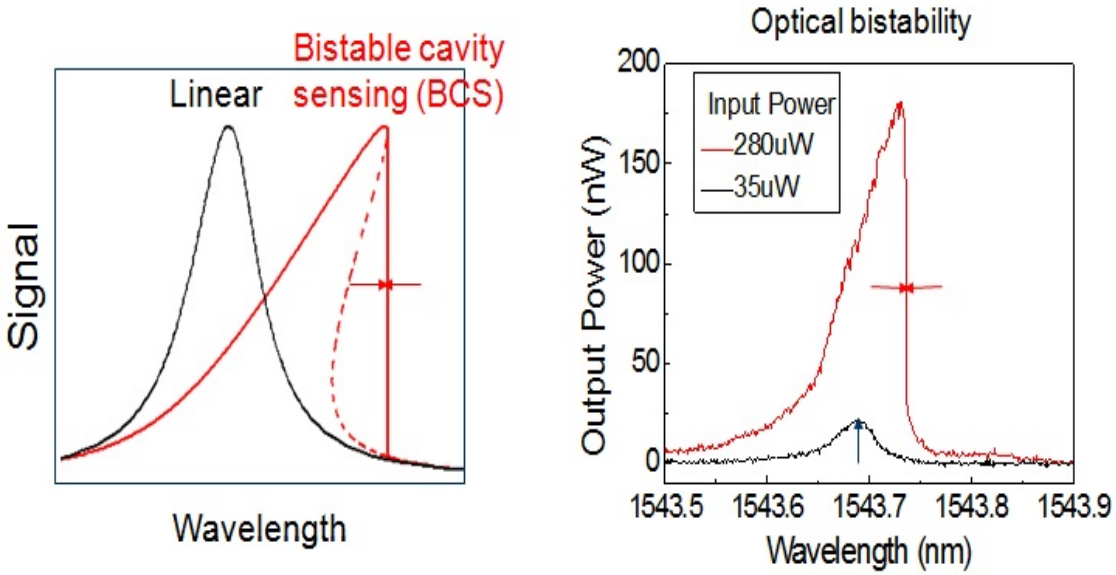

Figure 4.13.— (a) Comparison (schematics) of the conventional linear tracking method and the BCS tracking method. The solid line shows the spectral response when the laser wavelength is swept from short wavelengths to long wavelengths (black for linear, red for BCS). The sharp drop in power at the edge of the bistable region, with an effective width limited only by the frequency resolution and stability of the laser, serves as an ideal tracking feature for monitoring small shifts induced by analytes. (b) Experiment spectrum demonstrating the nonlinear response when the power is above the nonlinear threshold.

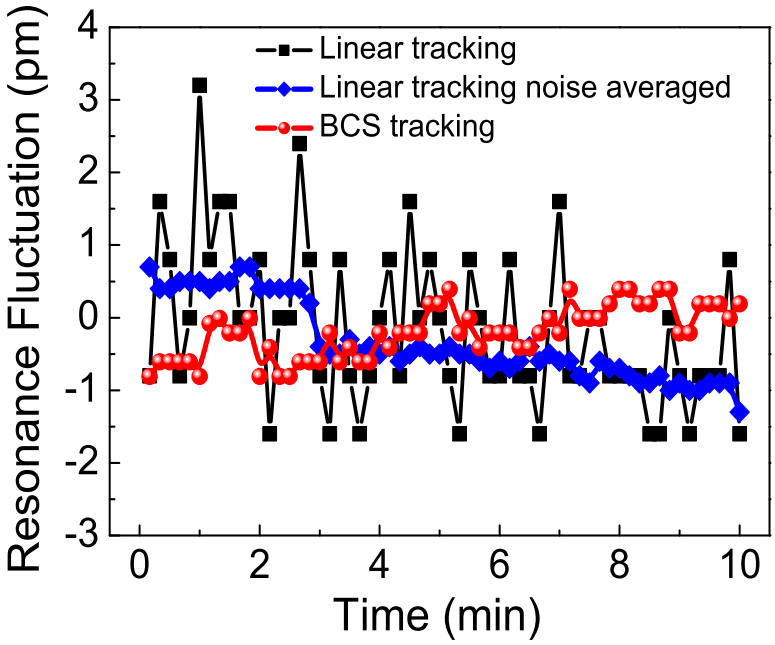

Figure 4.14.— Comparison of the noise level in the linear tracking method, linear tacking with noise averaging using the Lorentzian fitting, and the BCS tracking method (with Santec laser). BCS tracking shows significant improvement over the linear tracking, and is comparable to the noise averaged fitting method. This indicates that BCS method is immune of noise of the detector.

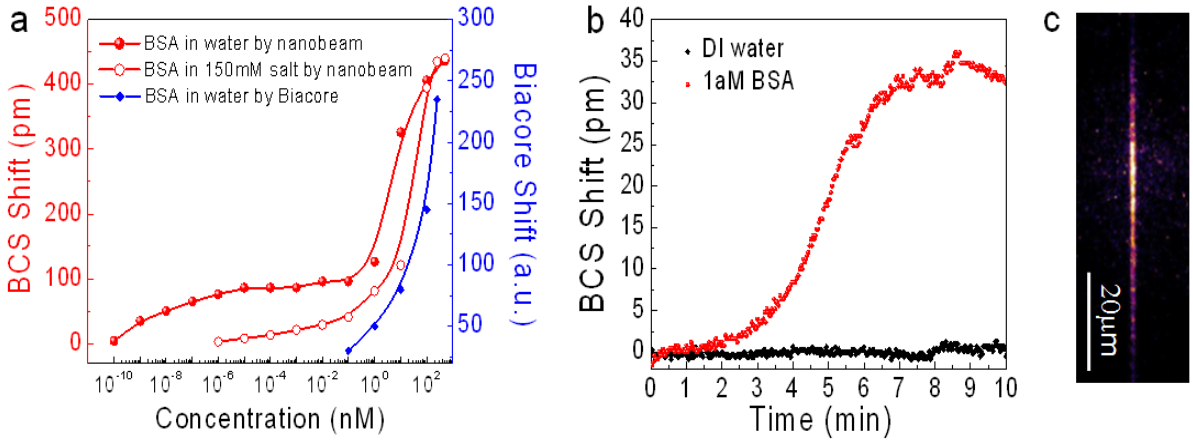

Figure 4.15.— (a) Equilibrated resonance shifts in the nonlinear resonances due to the adsorption of BSA onto nanobeam cavity at different BSA concentrations, showing a saturable adsorption isotherm. Measurement was taken under continuous fluid flow at 0.5mL/min in DI water and in 150mM NaCl. The same experiment was also performed with Biacore™ 3000 instrument, indicating that nanobeam sensor improved sensitivity by 9 orders of magnitude. The Biacore™ gold chip was functionalized by immersing in the 2mM NH_2-C_xH_y-SH in ethanal overnight. (b) The real-time monitoring of the nonlinear resonance following the injection of 1aM BSA (labeled with fluorophores) solution in the microfluidic channel. (c) Fluorescence image of the nanobeam cavity that was used in the sensing experiment.

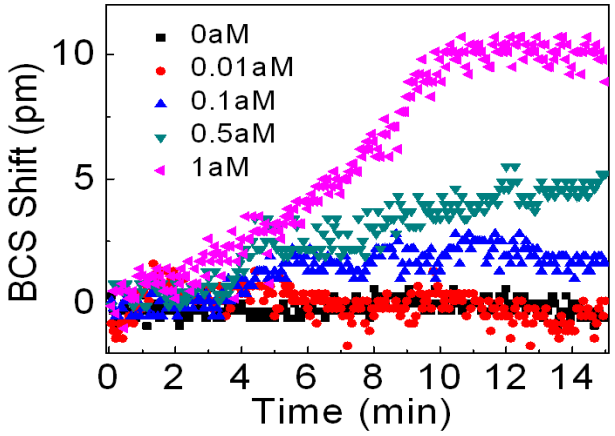

Figure 4.16.— The resonance shift induced by BSA molecules adsorbed on the sensor surface from BSA concentrations of 0aM (pure DI water), 0.01aM, 0.1aM, 0.5aM and 1aM BSAs were injected into the microfluidic channel. The sensor was regenerated with Sodium dodecyl sulfate (SDS) between different concentrations. We hypothesize that the discrepancies in the 1aM response between the current figure and Fig. 3(b) were likely due to inconsistency the surface functionalizations, as well as insufficient regeneration of the sensor between each experiment.

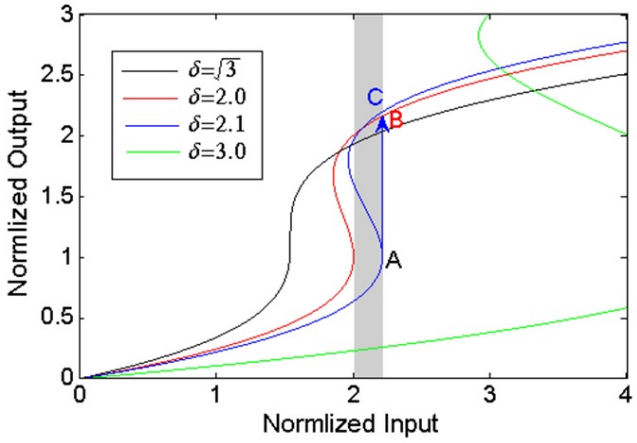

Figure 4.17.— Output-input power relation at different detunings, when $Q_{\text{total}} = Q_{\text{wg}}$. The power is normalized by the characteristic power of nonlinearity, detuning (δ) is normalized by the cavity linewidth when no nonlinearity is present.

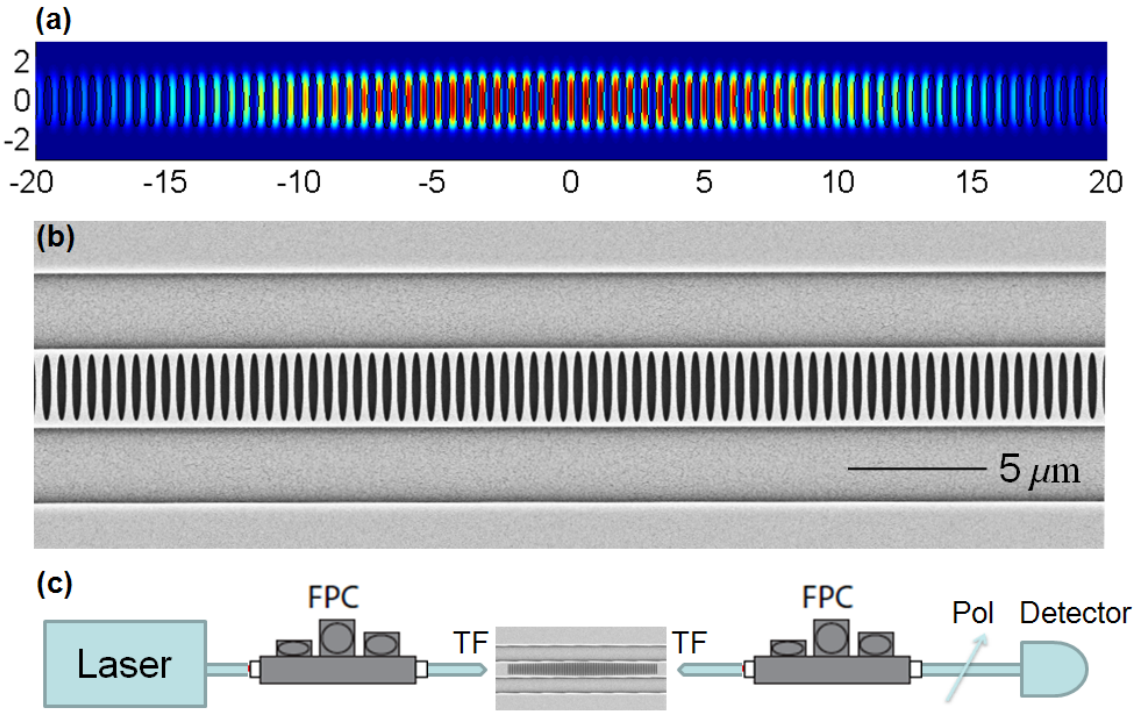

Figure 4.18.— (a) Energy density distribution of the cavity mode from FDTD simulation. (b) Scanning electron micrograph of the polymeric nanobeam cavity. (c) Schematics of the measurement setup. A tunable laser source is coupled to the edge of the chip through a tapered fiber (TF, Ozoptics inc.) after the fiber polarization controller (FPC), and collected from tapered fiber followed by a second FPC and an inline polarizer (Pol) to the detector. The two FPCs are to filter out unwanted TM polarization component that is not in resonance with the cavity.

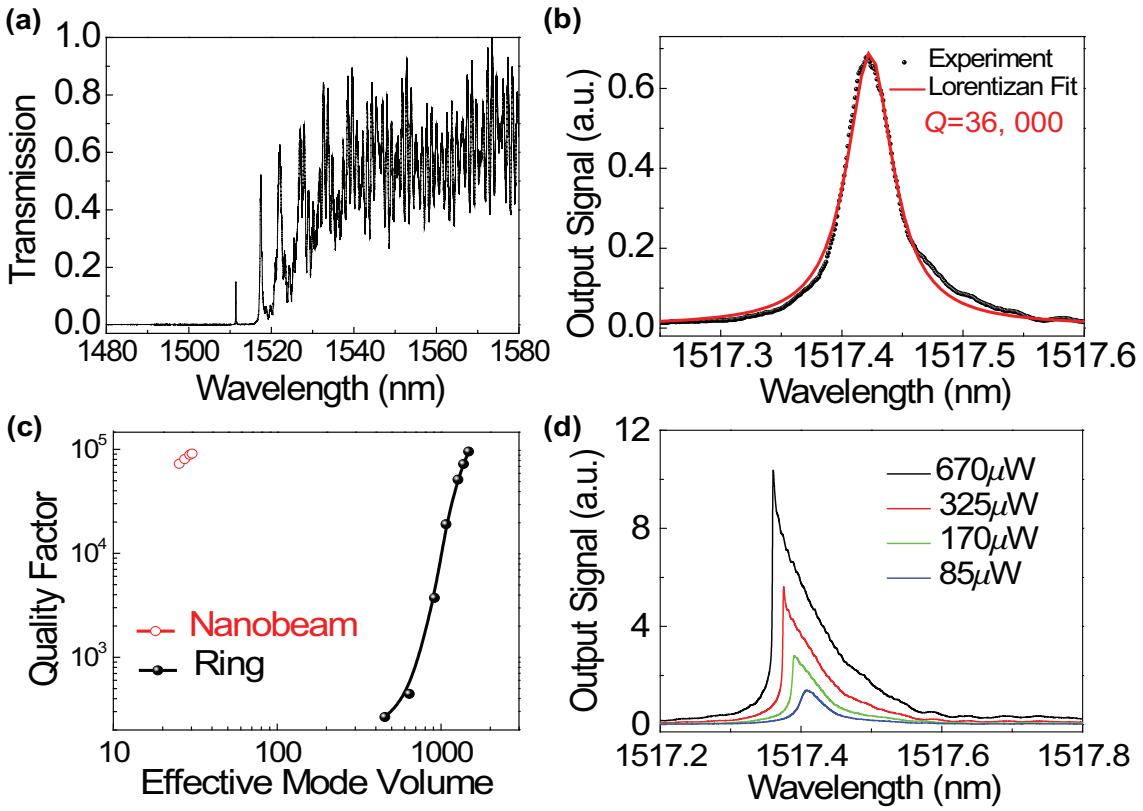

Figure 4.19.— (a) Measured optical transmission spectrum of a high-transmission polymeric nanobeam cavity in D_2O. The cavity mode has Q=11,000 with a high on-resonance transmission 15%. (b) The experimental transmission spectrum of the designed high Q cavity mode. Q of 36,000 is extracted from Lorentzian fit. (c) Comparison of theoretical Q factors and mode volumes between PhC nanobeam cavities and ring resonators with the same waveguide dimension. Mode Volumes are normalized by $(\lambda/n_{\mathrm{ZEP}})^3$. The number of tapered hole pairs in the nanobeam cavities are varied from 45 to 60, with an additional 50 hole pairs on both ends of the tapered section. The radii of the rings are varied from 25μm to 80μm. (d) Transmission spectra of the cavity mode at different input powers, showing optical bistability. The power levels indicated in the legend correspond to the powers coupled into the on-chip waveguide. The laser wavelength was swept from shorter to longer wavelengths across the cavity resonance.

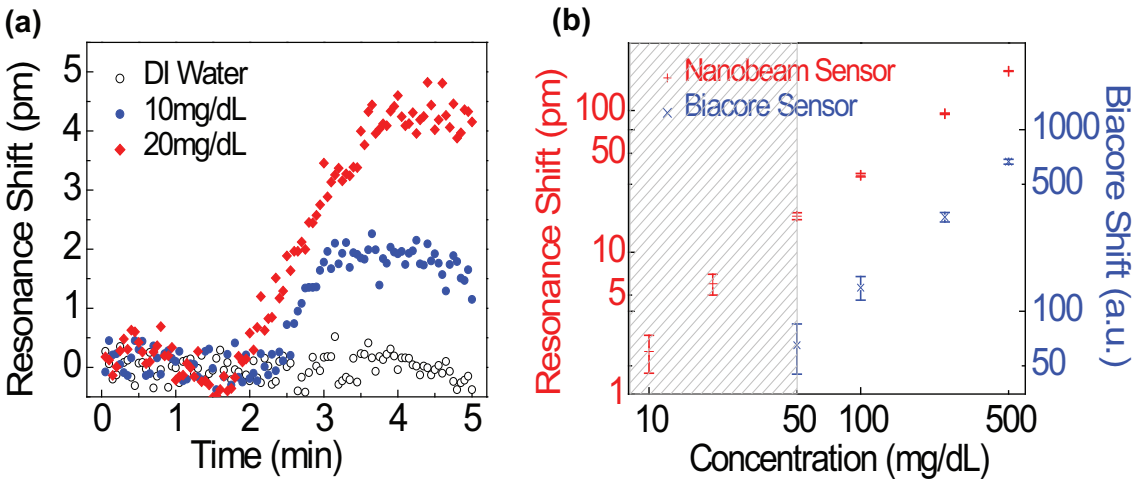

Figure 4.20.— (a) The real-time response of the resonance shift in response to the infusion of pure DI water, and glucose solutions with concentrations of 10mg/dL and 20mg/dL. (b) Equilibrated resonance shifts in different concentrations of glucose solutions in DI water measured by the nanobeam sensor and Biacore™ 3000 instrument respectively. The Biacore chip was functionalized with (11-Mercaptoundecyl)tetra(ethylene glycol) terminated with PEG to prevent adsorption of molecules on the gold surface to insure the measured responses are due to the bulk glucose index change.

Chapter 5

Instrumentation - From Single Molecule to Portable Biosensor

5.1 Introduction

With the discovery of new disease biomarkers and emergence of new pathogenic strains of bacteria and viruses, rapid and sensitive biomolecular detection is increasingly important in biomedicine and public health. While ultra-sensitive and specific fluorescence based assays have enabled a number of scientific advances and commercial applications, the labeling process is often complex, difficult to control, can interfere with receptor affinity, limits the throughput and results in long assay time.

5.2 Fabrication of Sensor Chips with Foundry Technology

The foundry provides wafer scale technologies based on deep UV (DUV) lithography with 193nm and 248nm exposure wavelengths. These 200mm DUV exposure tools are used for micro-electronics manufacturing in technology nodes down to 90nm. For fabrication of silicon photonics circuits, mask technologies of 0.13um to 0.25um are used. The step-and-scan tools replicate the mask over the wafer many times. Depending on the die size, 50 to 1000 chips per 200mm wafer are obtained in a couple of minutes. The wafers enter the step-and-scan tools through a track, which fully automatically spins the resist and anti-reflective coating and performs the pre-bake and after exposure the post-bake steps and development steps. Most silicon photonics researchers in academics use e-beam lithography for fabrication of integrated devices. With these e-beam tools, a high resolution and rapid turn-around can be achieved, and no masks are needed. Deep UV lithography tools at 193nm and 248nm wavelengths are more expensive and a mask-based technology but are currently the only way to do circuit-level research and demonstrate large-scale integrated photonic ICs. The benefits of DUV lithography is its large field size. ICs with many photonic integrated devices can be prototyped, for complex circuits, testing many devices or large parameter sweeps. Second, it produces large amount of chips. With DUV lithography, fabricating 200 or 1000 chips is as easy as fabricating one. This is beneficial for research involving post-processing of silicon ICs such as for heterogeneous integration, biosensing, etc.

Fig. 5.1 shows a photograph of the wafer that we designed and ordered for

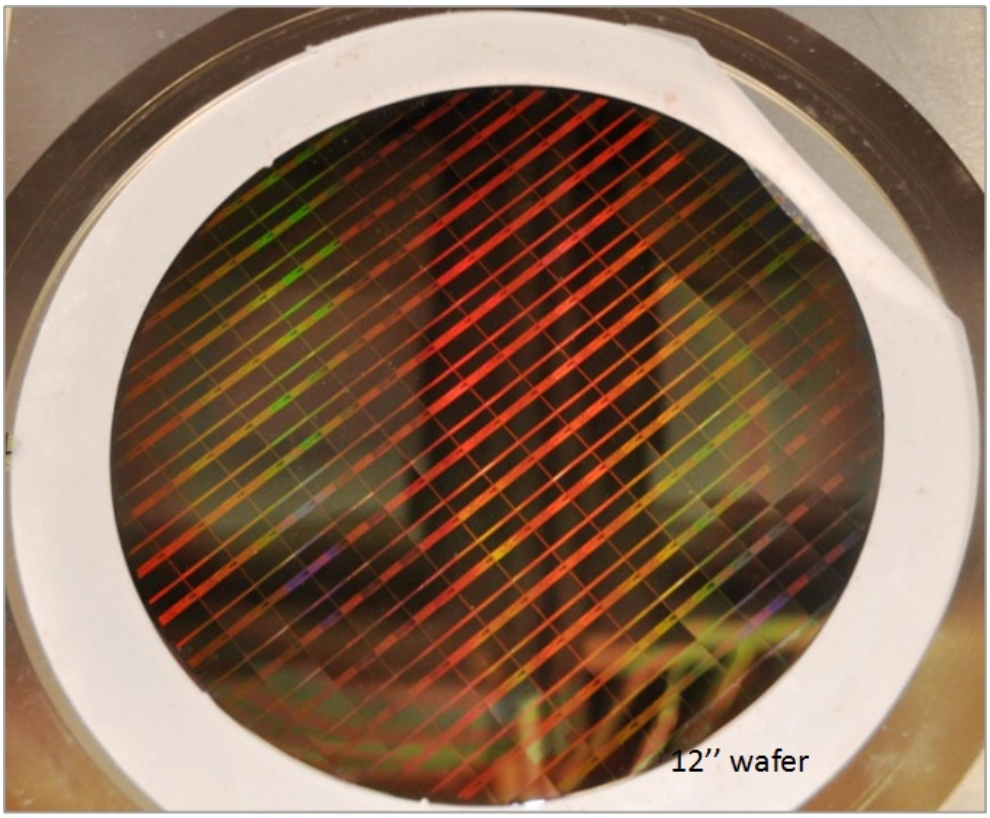

Figure 5.1.— Photograph of the 12" wafer fabricated by silicon foundry.

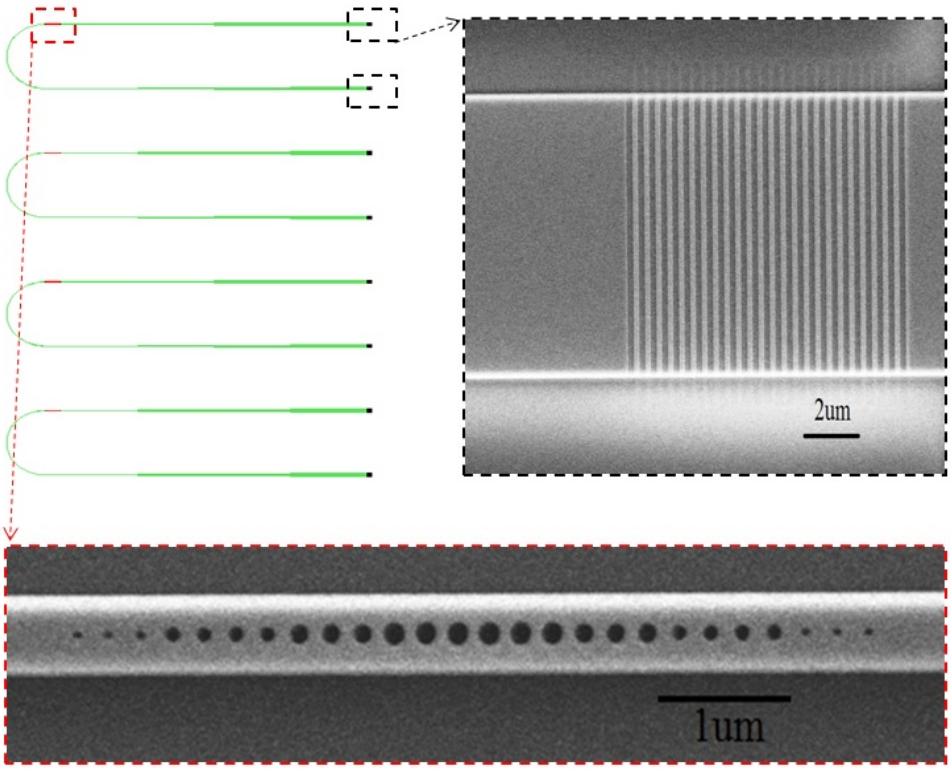

Figure 5.2.— (a) Schematic of an array of 6 optical circuits on the chip. Each optical circuit consists of the nanobeam cavity (red squared), two grating couplers (black squared), and optical waveguide connecting both. (b) SEM image of the grating coupler. (c) SEM image of the nanobeam cavity.

fabrication in the European IMEC silicon photonics foundry. The 12" wafer was diced into about 200 pieces, with each piece 12.36mm×13.80mm. On each piece, an array of optical circuits (containing nanobeam cavity, optical waveguide, grating couplers) were fabricated, as shown in Fig. 5.2(a). Fig. 5.2(b) shows the SEM image of the grating coupler. The distance between the two grating couplers are $250\mu m$, which fits to commercial fiber arrays. In this scheme, one grating coupler acts as input and the other as output. Fig. 5.2(c) shows the SEM image of the nanobeam cavity, which is the sensing region.

5.3 Optical Read-out Instrument

In Chapter 3 and 4, the nanobeam sensor is coupled in-line to an optical fiber. Such configuration allows high coupling efficiency, and integrating a microfluidic channel on top of the sensor. However, the alignment tolerance is as small as 0.5μm on each side, challenging for instrument automation, and inline coupling from both edge of the chip is not compatible with wafer scale testing. Therefore, we developed a grating based vertical coupling scheme.

A photograph of the instrument is shown in Fig. 5.3. Commercially available fiber arrays, each separated by 250μm standard, were used such that any two adjacent fibers could be accurately aligned to the gratings corresponding to in/out coupling. Previous work shows minimizes second order reflection occurring during coupling can be minimized by mounting the fiber array at 10° to the vertical(127). For initial alignment, the objective was used to locate the fiber with the grating. The fibers were located 2mm above the grating, which results in low signal, but

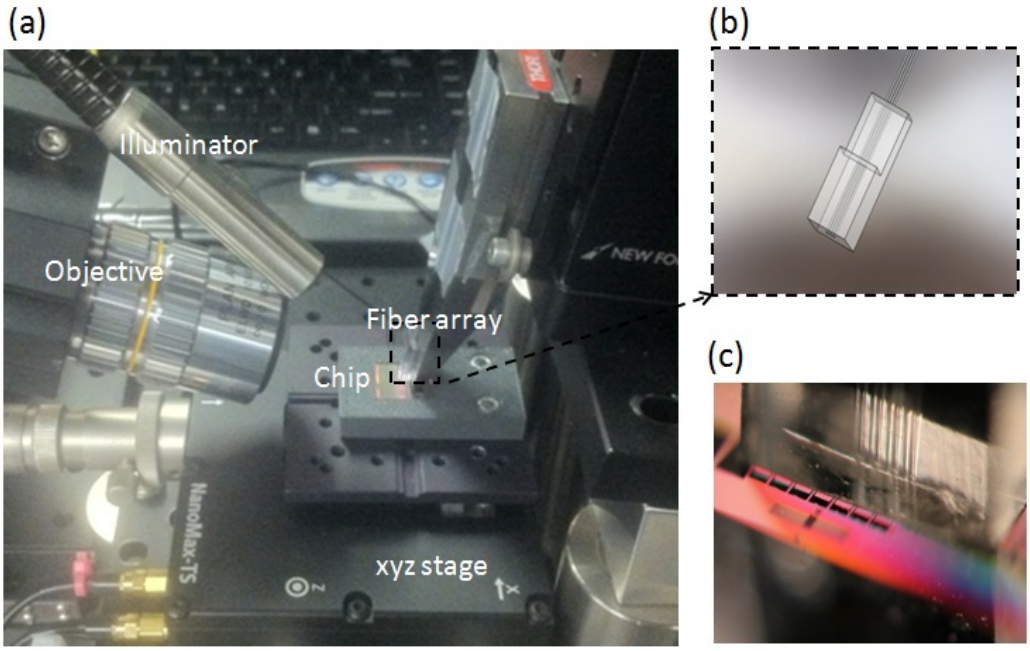

Figure 5.3.— (a) Photograph of the Instrument. It consists of a 10x objective to align the fiber with the grating, optical illuminator to light up the view of the objective, xyz stage that mounts the sensor chip, and fiber array mounted on a wedged stage. (b) Schematic of the fiber array. It consists of an array of optical fibers with 250μm spacing. The fiber array is commercially available (Oz optics inc.). (c) The optical image from the objective when the fiber is on the grating.

easy alignment. The input wavelength was chosen at 1550nm, the designed center wavelength of the coupling. The optical chip was situated on a 3-axis piezoelectric stage beneath the fiber array. Once initial coupling is achieved, the chip is raised to 20m below the fiber array. An automated scan was performed by the piezo- stage to locate the optical coupling position.

A tunable laser source (from 1480nm to 1580nm) is used to probe the transmission of the nanobeam cavity. A typical transmission signal is shown in Fig. 5.4. A clear resonance at 1498nm is observed. By fitting the resonance to a Lorentzian profile, we obtained Q of 2,100.

This set-up is different from the fiber butt-coupling set-up that we discussed in Chapter 3. The advantage of the current grating set-up is (1) Sensors can be placed in 2D format, or at arbitrary position on the chip. In contrast, the fiber-waveguide configuration requires the optical waveguides penetrate to the edge of the chip; (2) vertical coupling geometry is ideal for wafer-scale (or chip-scale) scanning (3) advantageous for instrumentation due to large tolerance of the grating coupler (typically $> 3\mu$m as shown in Fig. 5.5), as compared to the fiber-waveguide coupling scheme (typically $< 0.5\mu$m).

To study the tolerance of this grating coupling approach, we performed a position scan and plot the intensity in Fig. 5.5. The efficiency drops by half as the misalignment was increased to $\pm 3\mu$m.

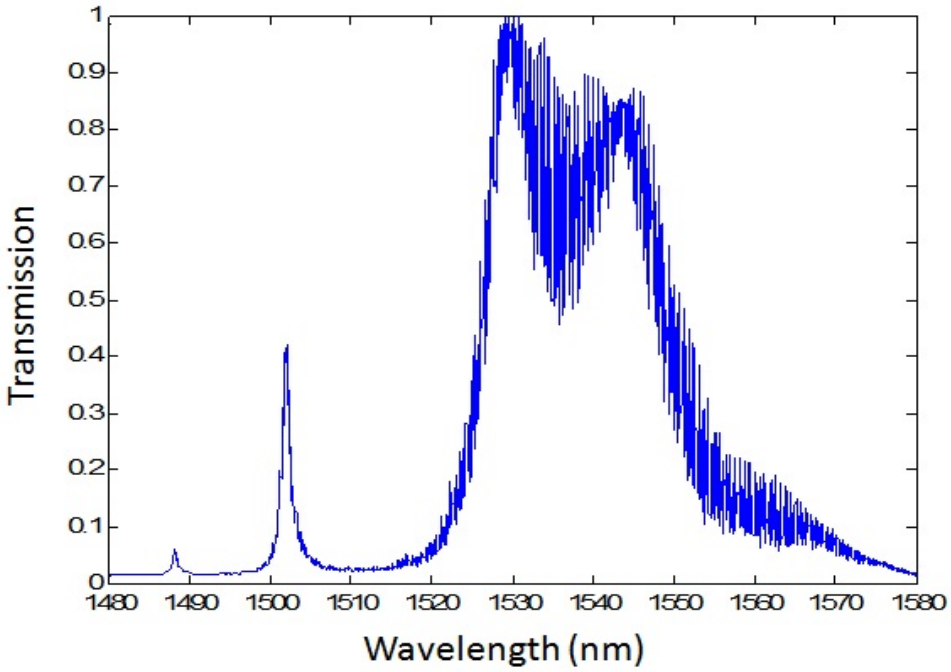

Figure 5.4.— Transmission signal from the chip. The signal is normalized to the maximum value of its pass band. The resonance is located around 1488nm, with Q of 2,100.

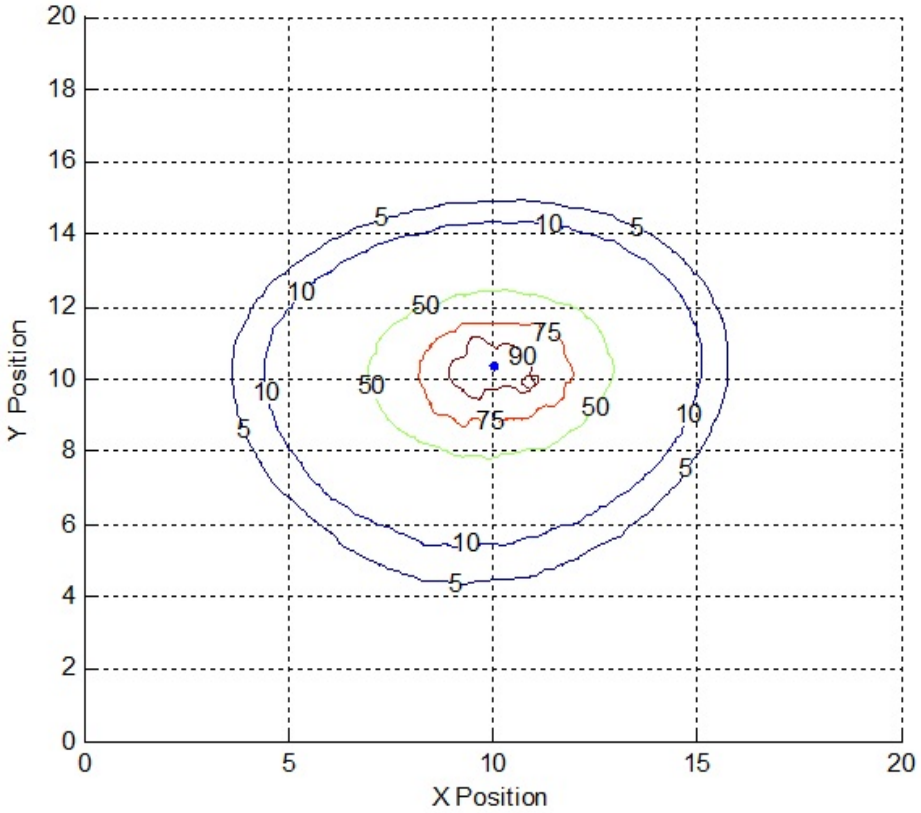

Figure 5.5.— Contour plot of the transmitted power as the stage is scanned $\pm 10\mu$m from its maximum value.

5.4 Testing of the Sensor

5.4.1 Refractive Index Sensing

To characterize the sensor, the resonance wavelength was measured after each of Methanol, Acetone, and IPA was dropped on to the chip, as shown in Fig. 5.6. A sensitivity of 89nm/RIU was achieved, showing slight improvement over the 83nm/RIU demonstrated in Chapter 4.

5.4.2 Protein Sensing

Three concentrations of streptavidin were tested sequentially on a single chip as well as a saline buffer solution. The resonance wavelength found from data recorded on thirty second intervals following each addition of 10L drop of a new concentration. Upon completion, the device was rinsed with a buffer saline solution to remove any streptavidin not bound to the optical cavities, and then the resonance wavelength re-measured. As the streptavidin binds to the cavity, a shift in resonance can be seen (Fig. 5.7). When the 1μM concentration is added, the cavity is quickly saturated and this effect is no longer seen. The decrease in resonance wavelength at this point is likely caused by a decreasing bulk index that is the result of a high local concentration of streptavidin that disperses with time. The resonance wavelength showed minimal shift from this rinse, confirming the protein had successfully bound. This also shows the resonance shift was caused by protein binding as opposed to bulk changes in refractive index, confirming the detection of 1pM streptavidin.

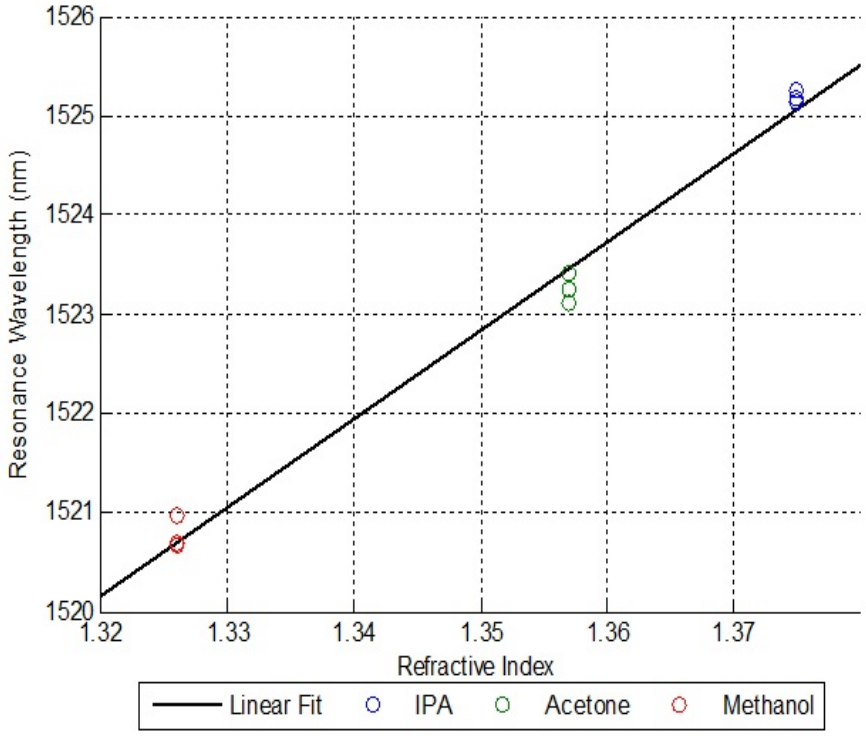

Figure 5.6.— Cavity resonances when methanol, acetone and isopropanol (IPA) are dropped on to the chip. The black line is the linear fit to the experimental data.

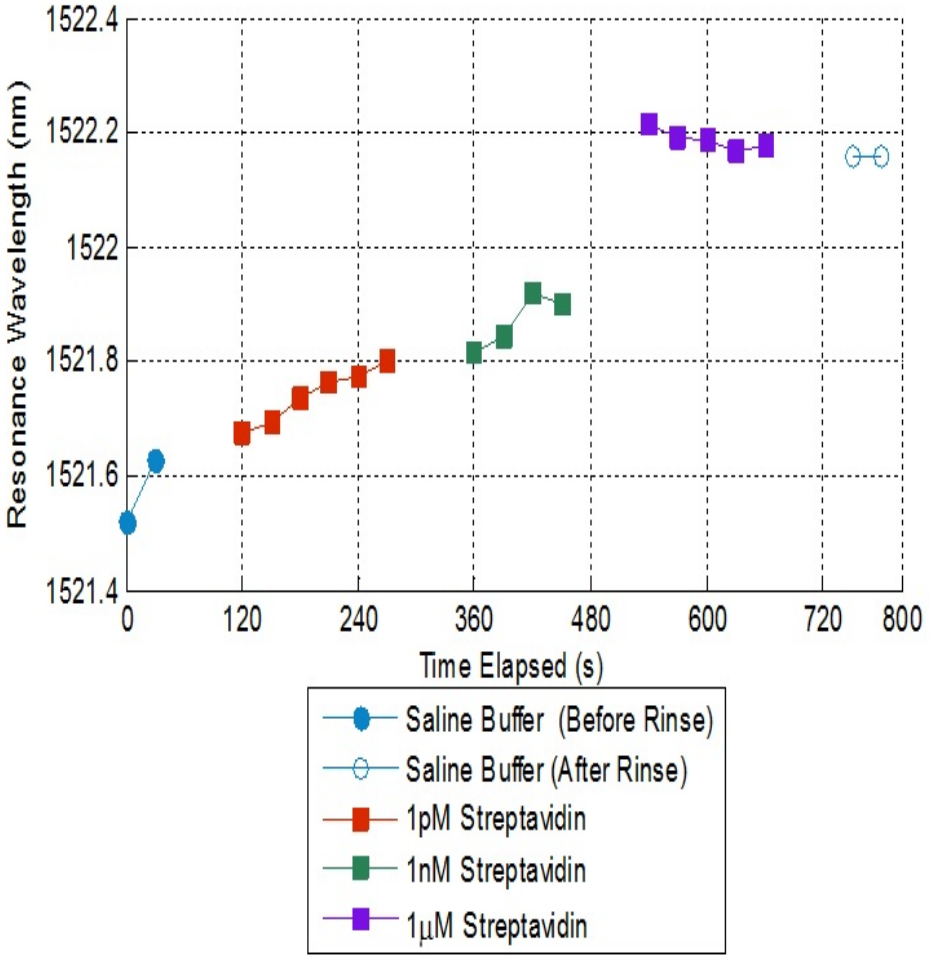

Figure 5.7.— Cavity resonances when streptavidin solution (1pM, 1nM and 1μM were dropped on to the sensor. Prior to that, the chip was cleaned by oxygen plasma and immersed in 2% 3-aminopropyltrimethoxysilane in ethanol for 10 minutes, rinsed thoroughly and heated at 80°C for 2 hours.

5.5 Summary

We discussed the efforts toward instrumentation of the nanobeam sensor technique. Two essential progresses have been demonstrated from Chapter 4 towards the instrumentation and commercialization.

First, we demonstrated that the silicon chips that were fabricated with the large scale silicon photonics foundry technology function well. Nanoscale photonic structures can be fabricated with E-beam lithography technique in standard cleanroom settings. However, E-beam lithography suffers from slow speed, high cost, and low volumes, and thus is not scalable. The demonstration of the foundry chips show high promise of the scalability and cost-effectiveness of this technology.

Second, the signal read-out configuration is modified from the planar fiber-waveguide coupling to the vertical grating coupling configuration. This reduces the number of optical stages by half, decreases the cost and ease the alignment procedure. As we have shown, the tolerance of the grating coupling is an order of magnitude better than the fiber-waveguide configuration. In addition, commercial fiber arrays that have multiple fibers with standard spacings are commercially available. With fiber arrays, multiple sensors can be probed simultaneously, and thus is ideal for high-throughput, multiplexed detection.

To further package the sensor into a portable instrument, we 3D printed additional parts to fit around a 3-axis motorized stage (Thorlabs Inc.), as illustrated in Fig. 5.8. The photograph is shown in Fig. 5.9. The stages are programmed to automatically scan over the chip to locate the coupling position. The chip is located

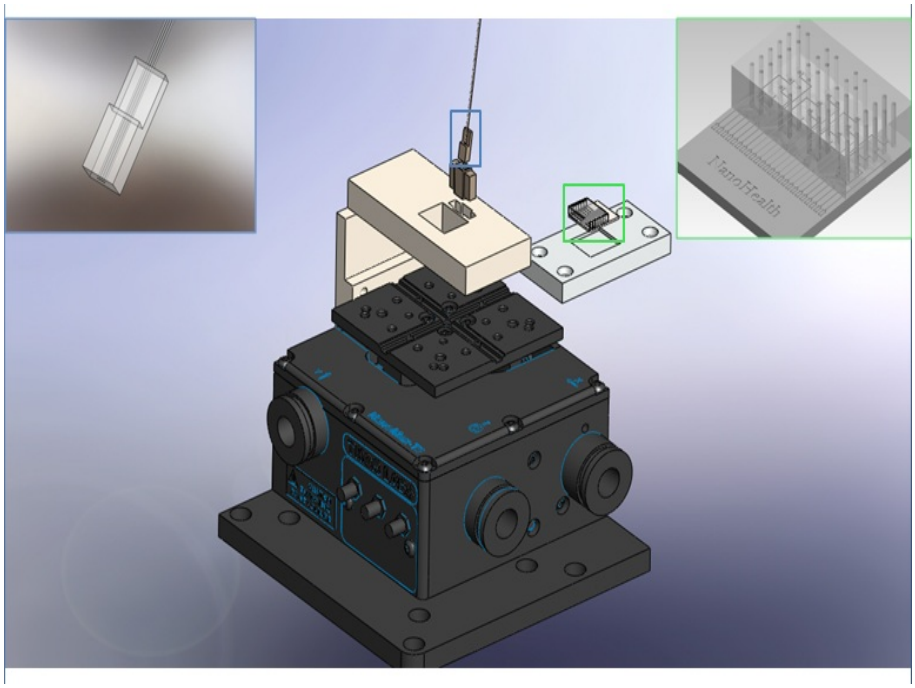

Figure 5.8.— Schematic of the portable instrument. Two inset shows the schematics of the fiber bundles, and the sensor chip, with PDMS micro-fluidic channels on top.

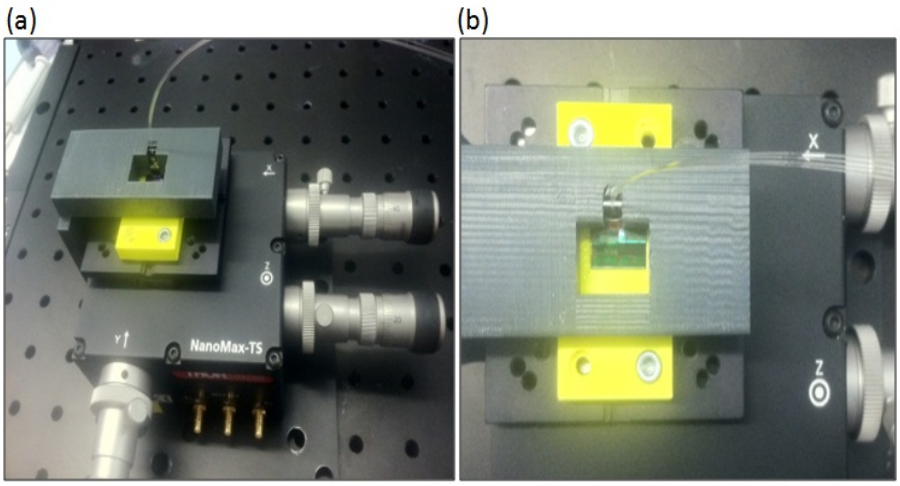

Figure 5.9.— Photo of the portable instrument. Yellow component is the holder of the sensor chip. To replace the sensor chip, the yellow part can be screwed off. (a) Perspective view. (b) Top view.

on a plastic holder, replaceable by screwing off the stage. Optimizing and testing of this portable set-up is in progress.

Chapter 6

Conclusions and Future Directions

6.1 Conclusions

This thesis discusses designs and experiments of various photonic nanostructures to manipulate light on nano- to micro- scale, especially to modify the light-matter interaction property, and achieve novel applications in quantum optics and bio-molecule detection.

The first half of the thesis focuses on the design of the photonic nanostructures to manipulate light on nano- to micro- scale.

In Chapter 2, we proposed and demonstrated nano-slot waveguides and photonic crystal nanobeam waveguides as an ideal platform to control the absorption and emission of emitters, and therefore achieve useful applications in quantum communications.

In Chapter 3, we demonstrated a deterministic method to design high-Q, small

mode volume photonic crystal nanobeam cavities. We discussed in detail different designs, the mode properties, far field properties, coupling method, fabrication techniques and characterizations of the nanobeam cavities. This lays out the foundation of the biomedical sensing applications for the second half of the thesis.

The second half of the thesis focuses on the application of photonic crystal nanobeam cavities in the label-free sensing of biomedical substances.

Chapter 4 demonstrates detection of solutions with different refractive index (aceton, methanol, IPA etc.), glucose concentration, single polystyrene nanoparticles and single streptavidin bio-molecules. Chapter 4 proposes a novel nonlinear optical method to further enhance the sensitivity. Chapter 4 also demonstrates high quality nanobeam cavities fabricated in polymers, that open up a new route to decrease the cost, as well as to achieve novel applications with functional polymers.

With the promising applications that demonstrated in Chapter 4, Chapter 5 discusses the instrumentation of the nanobeam cavity sensor for a new generation of biosensors with high sensitivity and high integration. The sensor is capable of detecting low abundance biochemical particles (e.g proteins, viruses and etc) in real-time. The advantage of current technology is (1) high sensitivity (2) high throughput and (3) low-cost in mass-production, leveraging silicon technology. Furthermore, the sensor can be integrated with electronic components and versatile forms of fluidic/gas channels; and supports high throughput and parallel detection.

6.2 Future Directions

Increase sensitivity: Although we have demonstrated the detection of single streptavidins, they are relatively large protein molecules. The detection limit of the current technology is on the order of 10nm-size molecule. Smaller molecules like antigens, nuclei acid are useful biomarkers for disease diagonosis and fundamental research.

The sensitivity is determined by the mode volume, and Q of the cavity. Although the designed Q is much higher than the experiment value, improving Q is difficult since it requires more powerful nanofabrication technique than E-beam lithography. Decreasing the mode volume is possible, for example, by combining the nano-slot effect that we introduced in Chapter 2 with the nanobeam cavity.

The other way to increase the sensitivity is to operate at smaller wavelength. Currently, to leverage the silicon technology, our sensing experiment is performed at 1550nm. Decreasing the wavelength to visible or near-UV will improve the detection limit. Polymer nanobeam cavities are good candidates for visible and near-UV applications.

Finally, the BCS method also shows high promise in improving the detection limit. Current data in Chapter 4 indicate BCS method outperforms the maximum tracking linear method and is on the same order with the Lorentzian fitting method. Since the detection limit of BCS method is imposed by the laser stability, improving the laser property is also a promising route to improve the detection limit.

Specificity of the assay: Our demonstrations in the current thesis did not

involve simultaneous detecting of several difference subjects. In real applications, it is equally important (if not more) to know what is the detected substance as to detect the substance. However, the optical method does not differentiate two molecules with similar indices.

To remedy this problem, the antigen-antibody lock and key method can be used to differentiate molecules. The nanobeam cavities can be functionalized with antibodies prior to the assay, and signals from different cavities will indicate the corresponding antigens.

Packaging: To further commercialize the technology will involve packaging of the set-up. Proof-of-concept progresses towards instrumentation have been demonstrated in Chapter 5, however, automation of the instrument, software controlled user-interface, temperature reference and control of the sensor, optimization of the fluidic circuits to minimize the reagent volumes, sample handling procedures and etc. remained to be developed.

Assay in complex mixture: To facilitate the application of the technology in real diagnostics, assays in complex mixture (e.g blood) have to be carried out and compared to the gold standard results. Standard operation procedures (SOP) to functionalize the sensor chips, to perform the assay and to quality control various batches of the sensors must be carried out.

References

[1] T. F. Krauss, R. M. DeLaRue, S. Brand, Nature **383**, 699-702 (1996)

[2] J. S. Foresi et. al., Nature **390**, 143-145 (1997).

[3] Y. Akahane, T. Asano, B. S. Song, and S. Noda, Nature **425**, 944-947 (2003)

[4] J. Vuckovic, M. Loncar, H. Mabuchi, and A. Scherer, IEEE Journal of Quantum Electronics, **38**, 850-856 (2002)

[5] V. R. Almeida et al., Opt. Lett. **29**, 1209-1211 (2004)

[6] Q. Xu et. al., Opt. Lett. **29**, 1626-1628 (2004)

[7] R. Sun et al., Opt. Express **15**, 17967-17972 (2007)

[8] J. T. Robinson, K. Preston, O. Painter and M. Lipson, Opt. Express **16**, 16659-16669 (2008)

[9] C. C. Lin, D. G. Deppe, and C. Lei, IEEE J. Quantum Electron. **30**, 2304-2313 (1994)

[10] C. F. Janz and J. N. McMullin, IEEE, J. J. Quantum Electron. **31**, 1344 (1995)

[11] M. Galli et. al., Appl. Phys. Lett. **89**, 241114 (2006)

[12] C. Creatore et. al., Appl. Phys. Lett. **94**, 103112 (2009)

[13] S. T. Ho, S. L. McCall, and R. E. Slusher, Opt. Lett. **18**, 909-911 (1993)

[14] J. T. Robinson et. al., Phy. Rev. Lett. **95**, 143901 (2005)

[15] Meystre. P. & Sargent III, M. *Elements of Quantum Optics,* 3rd ed. (Springer-Verlag, New York, 1999)

[16] H. Mabuchi and A. C. Doherty, Science **298**, 1372-1377 (2002) and refereces therein.

[17] K. M. Gheri and H. Ritsch, Phys. Rev. A **56**, 3187 (1997)

[18] D. E. Chang, A. S. Sorensen, E. A. Demler and M. D. Lukin, Nature physics **3**, 807-812 (2007)

[19] E. M. Purcell, H. C. Torrey, and R. V. Pound, Phys. Rev. **69**, 37 (1946)

[20] A. Beveratos et. al., Phys. Rev. A. **64**, 061802(2001)

[21] S. Strauf et. al, Phys. Rev. Lett. **96**, 127404 (2006)

[22] M. D. Lukin, Rev. Mod. Phys. **75**, 457 (2003)

[23] V. S. C. Manga Rao and S. Hughes, Phys. Rev. Lett. **99**, 193901(2007)

[24] T. Lund-Hansen et. al., Phys. Rev. Lett. **101**, 113903 (2008)

[25] I. Friedler et. al., Opt. Express, **17**, 2095-2110 (2009)

[26] J. P. Burke et al., Phys. Rev. A. **65**, 043411(2002)

[27] G. L. J. A. Rikken, and Y. A. R. R. Kessener, Phys. Rev. Lett. **74**, 880 (1995)

[39] M. Fleischhauer, S. F. Yelin, and M. D. Lukin, Opt. Commun. **179**, 395 (2000)

[29] A. V. Gorshkov et. al., Phys. Rev. Lett **98**, 123601 (2007)

[30] H. J. Kimbal, Nature **452**, 1023 (2008)

[31] M. A. Nielsen and I.L. Chuang, "Quantum Computation and Quantum Information", Cambridge University Press, 2000

[32] L. M. Duan, M. D. Lukin, J. I. Cirac and P. Zoller, Nature **414**, 413 (2001)

[33] L. M. Duan et. al., Phys. Rev. A. **73**, 062324 (2006)

[34] D. L. Moehring et. al., Nature **449**, 68-71 (2007)

[35] J. I. Cirac, P. Zoller, H. J. Kimble, and H. Mabuchi, Phy. Rev. Lett. **78**, 3221 (1996)

[36] A. D. Boozer et. al., Phys. Rev. Lett. **98**, 193601 (2007)

[37] L. Jiang, J. M. Taylor, A. S. Sorensen and M. D. Lukin, Phy. Rev. A **76**, 062323 (2007)

[38] M. V. Dutt et. al., Science **316**, 1312 (2007)

[39] M. Fleischhauer, S. F. Yelin, and M. D. Lukin, Opt. Commun. **179**, 395 (2000)

[40] L. Novotny and B. Hecht, "Principles of Nano-optics", Cambridge University Press (2006)

[41] A. Yariv and P. Yeh, "Photonics: Optical Electronics in Modern Communications", Oxford University Press (2006)

[42] J. Wrachtrup, F. J. Jelezko, Phys.: Condens. Matter **18**, 807-824 (2006)

[43] P. Neumann et. al., Science **320**, 1326 (2008)

[44] J. L. O'Brien, Science **318**, 1567 (2007)

[45] K. J. Vahala, Nature **424**, 839-846 (2003).

[46] J. L. O'Brien, A. Furusawa, and J. Vuckovic, Nat. Photonics **3**, 687-695 (2009).

[47] J. Leuthold, C. Koos, and W. Freude, Nat. Photonics **4**, 535-544 (2010).

[48] M. Eichenfield, J. Chan, R. Camacho, K. J. Vahala, and O. Painter, Nature **462**, 78-82 (2009).

[49] D. Van Thourhout and J. Roels, Nat. Photonics **4**, 211-217 (2010).

[50] D. G. Grier, Nature **424**, 21-27 (2003).

[51] D. Psaltis, S. R. Quake, and C. Yang, Nature **442**, 381-386 (2006).

[52] E. Yablonovitch, Phys. Rev. Lett. **58**, 2059-2062 (1987).

[53] S. John, Phys. Rev. Lett. **58**, 2486 (1987).

[54] O. Painter et. al., Science **284**, 1819-1821 (1999).

[55] S. G. Johnson, S. Fan, A. Mekis, and J. D. Joannopoulos, Appl. Phys. Lett. **78**, 3388-3390 (2001)

[56] J. Ctyroky, J. Opt. Soc. Am. A **18**, 435-441 (2001).

[57] M. R. Watts, S. G. Johnson, H. A. Haus, and J. D. Joannopoulos, Opt. Lett. **27**, 1785-1787 (2002).

[58] J. M. Geremia, J. Williams, and H. Mabuchi, Phys. Rev. E **66**, 066606 (2002).

[59] M. Burger, S. J Osher, and E. Yablonovitch, IEICE Trans. Electron. **E87C**, 258C265 (2004).

[60] B. S. Song, S. Noda, T. Asano, and Y. Akahane, Nat. Mater **4**, 207-210 (2005).

[61] S. Tomljenovic-Hanic, C. M. de Sterke, and M. J. Steel, Opt. Express **14**, 12451-12456 (2006).

[62] E. Kuramochi, M. Notomi, S. Mitsugi, A. Shinya, T. Tanabe, and T. Watanabe, Appl. Phys. Lett. **88**, 041112 (2006).

[63] K. Nozaki, S. Kita and T. Baba, Opt. Express **15**, 7506-7514 (2007).

[64] Y. Tanaka, T. Asano, and S. Noda, J. Lightwave Technol. **26**, 1532 (2008).

[65] M. Notomi, E. Kuramochi, and H. Taniyama, Opt. Express **16**, 11095 (2008).

[66] P. Velha, E. Picard, T. Charvolin, E. Hadji, J. C. Rodier, P. Lalanne, and E. Peyrage, Opt. Express **15**, 16090-16096 (2007).

[67] S. Reitzenstein et al. Appl. Phys. Lett. **90**, 251109 (2007).

[92] A. R. Md Zain, N. P. Johnson, M. Sorel, and R. M. De La Rue, Opt. Express **16**, 12084 (2008).

[69] Y. Zhang and M. Loncar, Opt. Express **16**, 17400-17409 (2008).

[70] M. W. McCutcheon and M. Loncar, Opt. Express **16**, 19136-19145 (2008).

[71] L. D. Haret, T. Tanabe, E. Kuramochi, and M. Notomi, Opt. Express **17**, 21008-21117 (2009).

[72] J. Chan, M. Eichenfield, R. Camacho, and O. Painter, Opt. Express **17**, 3802-3817 (2009).

[73] P. B. Deotare, M. W. McCutcheon, I. W. Frank, M. Khan, and M. Loncar, Appl. Phys. Lett **94**, 121106 (2009).

[74] Q. Quan, P. B. Deotare, and M. Loncar, Appl. Phys. Lett. **96**, 203102 (2010).

[75] E. Kuraamochi, H. Taniyama, T. Tanabe, K. Kawasaki, Y-G. Roh, and M. Notomi, Opt. Express **18**, 15859-15869 (2010).

[76] Q. Quan, I. B. Burgess, S. K. Y. Tang, D. L. Floyd and M. Loncar, Opt. Express **19**, 22191-22197 (2010).

[77] K. Srinivasan, and O. Painter, Opt. Express **10**, 670-684 (2002).

[78] D. Englund, I. Fushman, and J. Vuckovic, Opt. Express **13**, 5961-5975 (2005).

[79] M. Palamaru, and P. Lalanne, Appl. Phys. Lett. **78**, 1466-1468 (2001).

[80] P. Lalanne, S. Mias, and J. P. Hugonin, Opt. Express **12**, 458-467 (2004).

[81] K. Sakoda, *Optical Properties of Photonic Crystals*, 2nd Edition, Springer (2005).

[82] J. D. Joannopoulos, S. G. Johnson, J. N. Winn, R. D. Meade, *Photonic Crystals: Molding the flow of light*, 2nd Edtition, Cambridge University Press (2007).

[83] S. G. Johnson et. al., Phys. Rev. E **65**, 066611 (2002).

[84] J. Vuckovic, M. Loncar, H. Mabuchi, and A. Scherer, Phys. Rev. E **65**, 016608 (2001).

[85] B. H. Ahn, J. H. Kang, M. K. Kim, J. H. Song, B. Min, K. S. Kim, and Y. H. Lee, Opt. Express **18**, 5654-5660 (2010).

[86] D. W. Vernooy, A. Furusawa, N. P. Georgiades, V. S. Ilchenko, and H. J. Kimble, Phys. Rev. A **57**, R2293-R2296 (1998).

[87] D. K. Armani, T. J. Kippenberg, S. M. Spillane, and K. J. Vahala, Nature **421**, 925-928 (2003).

[88] M. Soltani, S. Yegnanarayanan, and A. Adibi, Opt. Express **15**, 4694-4704 (2007).

[89] S. J. McNab, N. Moll and Y. A. Vlasov, Opt. Express **11**, 2927(2003)

[90] M. Soljacic, M. Ibanescu, S. G. Johnson, Y. Fink and J. D. Joannopoulos, Phys. Rev. E **66**, 055601(R) (2002)

[91] L. Haret, T. Tanabe, E. Kuramochi and M. Notomi, Opt. Express **17**, 21108(2009)

[92] A. R. M. Zain, N. P. Johnson, M. Sorel and R. M. De La Rue, Opt. Express, **16**, 12084 (2008)

[93] C. B. Kim, B. Su C. Meas. Sci Technol. **15**, 1683-1686 (2004).

[94] T. Lu et al, Proc. Natl. Acad. Sci. USA **108**, 5976 (2011).

[95] S. Arnold, M. Khoshsim, I. Teraoka, S. Holler, F. Vollmer, Opt. Lett. **28**, 272-274 (2003).

[96] R. C. Weast, M. J. Astle(Eds.), CRC handbook of chemistry and physics, 61st ed. CRC Press, Boca Raton, FL, 1980

[97] K. Zirk, H. Poetzschke, Med. Eng.& Phys. **29**, 449-458 (2006)

[98] M. Iqbal et. al., IEEE J. Sel. Top. Quant. Electron. **16**, 654-661 (2010).

[99] M. Loncar, A. Scherer, Y. Qiu, Appl. Phys. Lett. **82**, 4648-4650 (2003).

[100] S. Kita, K. Nozaki, T. Baba, Opt. Express. **16**, 8174-8180 (2008)

[101] S. Fan, Appl. Phys. Lett. **80**, 908-910 (2002).

[102] C. Y. Chao, L. J. Guo, Appl. Phys. Lett. **83**, 1527-1529 (2003).

[103] V. R. Almeida, M. Lipson, Opt. Lett. **29** 2387-2389 (2004).

[104] T. Uesugi, B. S. Song, T. Asano, S. Noda, Opt. Express **14**, 377-386 (2006).

[105] L. Haret, T. Tanabe, E. Kuramochi, M. Notomi, Opt. Express **17**, 21108-21117 (2009).

[106] H. G. Winful, J. H. Marburger, E. Garmire, Appl. Phys. Lett. **35**, 379-381 (1979).

[107] I. M. White, X. Fan, Opt. Express. **16**, 1020-1028 (2008).

[108] A. M. Armani, R. P. Kulkarni, S. E. Fraser, R. C. Flagan, K. J. Vahala, Science **317**, 783-787 (2007).

[109] R. W. P. Drever et. al., Appl. Phys. B. **31**, 97-105 (1983).

[110] T. M. Squires, R. J. Messinger, S. R. Manalis, Nat. Biotech. **26**, 417-426 (2008)

[111] H. Ma, A. K. Y. Jen, L. R. Dalton, Adv. Mater. **14**, 1339-1365 (2002)

[112] M. C. Choi, Y. Kim, C-S. Ha, Progress in polymer science, 581-630 (2008)

[113] S-I. Na, S-S. Kim, J. Jo, D. Y. Kim, Adv. Mater. **20**, 4061-4067 (2008)

[114] H-Y. Chen et. al., Nat. Photon. **3**, 649-653 (2009)

[115] D. Ghezzi, M. R. Antognazza, M. D. Maschio, E. Lanzarini, F. Benfenati, G. Lanzani, Nat. Comm. **2**, 166 (2011)

[116] Broz, P. (Editor) Polymer-Based Nanostructures, 1st Edition. Royal Society of Chemistry (RSC) publishing (2010)

[117] X. D. Fan, I. M. White, S. I. Shopova, H. Y. Zhu, J. D. Suter, Y. Sun, Anal. Chim. Acta **620**, 8-26 (2008)

[118] A. L. Martin, D. K. Armani, L. Yang, K. J. Vahala, Opt. Lett. **29**, 533-535 (2004)

[119] L. Martiradonna et. al., Nano Lett. **8**, 260-264 (2008)

[120] C. Chao, L. J. Guo, J. Vac. Sci. Technol. B **20** 2862-2866 (2002)

[121] G. Gong, J. Vuckovic, Appl. Phys. Lett. **96**, 031107 (2010)

[122] D. Chu, M. Touzelbaev, K.E. Goodson, S. Babin, R.F. Pease, JVSTB **19**, 2874 (2001)

[123] O. Beyer, I. Nee, F. Havermeyer, K. Buse, Appl. Opt. **42**, 30-37 (2003).

[124] W. R. Folks, J. Ginn, D. Shelton, J. Tharp, G. Boreman, Phys. Stat. Sol. (c) **5**, 1113-1116 (2008).

[125] J. N. Anker, W. P. Hall, O. Lyandres, N. C. Shah, J. Zhao, R. P. Van Duyne, Nature Mat. **7**, 442-463 (2008)

[126] A. V. Ka-bashin et. al., Nature Mat. **8**, 867-871 (2009)

[127] D. Taillaert et. al., Jap. Journal. Appl. Phys. **45**, 6071 (2006)